Università degli Studi della Basilicata

DOTTORATO DI RICERCA IN
"Metodi e tecnologie per il monitoraggio ambientale"
Ciclo XXVIII

TITOLO DELLA TESI

"Synergy between Doppler radar and Raman lidar for aerosol investigation"

SETTORE SCIENTIFICO-DISCIPLINARE
"Fis/06"

COORDINATORE DEL DOTTORATO
Prof.ssa Aurelia Sole

DOTTORANDA
Dr.ssa Pilar Gumà Claramunt

TUTOR
Dr.ssa Gelsomina Pappalardo

Dr. Aldo Amodeo

Dr. Fabio Madonna

A.A. 2014/2015

Synergy between
Doppler radar and Raman lidar
for aerosol investigation

Pilar Gumà Claramunt

Potenza, December 2015

Contents

Introduction

The topic of this thesis is the investigation of giant atmospheric particles using ground-based remote sensing techniques. In this direction, the synergy of two ground-based remote sensing instruments –the Doppler radar and the Raman lidar– have been used to retrieve vertically resolved estimates of the aerosol properties. The main results of this work are the development of an automatic classification algorithm for giant aerosols based on the use of cloud radar observations, and the exploitation of the synergy between lidar and radar in order to enlarge the size range in which aerosols can be characterized.

Aerosols affect the meteorological and climate system in many ways. They interact with solar radiation through absorption and scattering. Aerosols counteract part of the induced warming caused by greenhouse gases, mostly by increasing the amount of sunlight reflected back to space (Rosenfeld, 2014). Their effects on the radiation budget through interaction with clouds have large associated uncertainties (IPCC, 2013). Aerosols act as Cloud Condensation Nuclei (CCN) and Ice Nuclei (IN), upon which cloud droplets and ice crystals form, affecting in this way the clouds and precipitation formation. The optical properties of clouds, for instance, are influenced by the aerosol size and chemical properties (Roelofs and Jongen, 2004). Aerosols exert a significant influence on ecosystems, by carrying nutrients to oligrotrophic systems. Mineral dust, in particular, acts as a fertilizer in the Amazon rainforest (Lovett, 2010) and has been found to enhance oceanic primary productivity (Gallisai et al., 2012).

Moreover, aerosols also have a large impact on human health by causing or enhancing respiratory, cardiovascular, infectious, and allergic diseases (Pöschl, 2005). They can also affect air transport, as happened during the spring of 2010, when the Eyjafjallajökull volcano eruption in Iceland caused an enormous disruption to air traffic across western and northern Europe (Pappalardo et al., 2013).

Aerosol sizes range from few nanometers to tenths of micrometers, can be of natural or anthropogenic origin and have different compositions. Besides, their properties and composition are subject to modifications from their emission until their removal from the atmosphere. The aerosols effects depend on their intrinsic nature. The aerosol size distribution is of primary importance to determine the aerosol effect on clouds and rain, and in particular the availability of Giant Cloud Condensation Nuclei (GCCN) has a major impact on cloud development and rain formation (Dagan et al., 2015) . Giant and ultragiant aerosols (>5 μm diameter) can act as GCCN, determining the concentration of the initial cloud droplets, the clouds albedo and lifetime, and the precipitation formation. In addition, depending on their composition, they can also act as IN. Mineral dust, for instance, is an efficient IN (DeMott et al., 2003), being the coarser particles the first to nucleate (or to be activated) due to their larger surface area (Möhler et al., 2006). Several studies have focused on the effects of giant aerosols in precipitation formation, often presenting opposite results. Early studies (Houghton, 1938; Johnson, 1982) showed that GCCN have a major effect on the collision-coalescence process by causing early formation of large drops. Feingold et al. (1999) and Eagan et al. (1974) found that the presence of giant CCN has an effect on precipitation formation, expediting especially warm rain processes. Even though, several studies have indicated the suppression of warm rain (Albrecht, 1989; L'Ecuyer et al., 2009; Hudson and Yum, 2001), and others show rain rate enhancement (Koren et al., 2010, 2014). Furthermore, a minor or no effect of GCCN on the initiation of rain in warm convective clouds has been reported by Khain et al. (2000), who found a comparatively weak effect of GCCN on the acceleration of raindrops formation. Finally, Dagan et al. (2015) stated that the warm rain production as the final evolution of all clouds processes is highly affected by aerosol loading and properties. In summary, the contradictory results reported by all these studies expose the necessity to further study the meteorological and climatological effects of giant aerosols.

The main ground-based remote sensing instruments used nowadays to measure aerosol properties are sun photometer and lidar. Sun photometer provides columnar information, while lidar has the capability to measure the aerosol vertical distribution. The design of the instruments and the operating wavelengths defines the particle sizes that can be observed. The higher end in the range of sizes measured does not exceed ten and few microns for sun photometer and lidar respectively. This means that they do not account for giant and ultragiant aerosols. Therefore, the distribution in the atmosphere and the impact on climate of these particles is not well known and the aerosol transport models largely underestimate them (Ginoux et al., 2011). Recent studies have demonstrated that cloud radars are able to detect ultragiant volcanic aerosols (Marzano et al., 2006a,b), and they can be measured at a large distance from the source (Madonna et al., 2010, 2013). However, measurements concerning giant aerosols were limited to a few case studies and to special events.

Considering the importance and the lack of measurements of giant aerosols, the aim of this study is to enhance the size range in which aerosol microphysical properties can be retrieved taking advantage of the combined use of lidar and radar: namely lidar has a better sensitivity to small size aerosols, while, on the other hand, radar can detect coarser particles. Consequently, the combined information offers the possibility to retrieve aerosol microphysical properties from the ultrafine to ultragiant size range and under all weather conditions, contributing to a better understanding of the effects of giant particles on meteorology and climate and providing useful information for the management of natural and health hazards.

The main novelties of this study are: (a) the use of cloud radar to study aerosols in a systematic way and for a long time interval for the first time, for which a whole new methodology has been developed; (b) for the first time, a novel inversion procedure to retrieve aerosol microphysical properties with a cloud radar has been created; and (c) the synergistic use of lidar and radar observations has allowed to enhance the size range in which aerosol microphysical properties can be retrieved.

This thesis is structured in the following way: the principal characteristics of atmospheric aerosols are described in *Chapter 1*, an overview of the scattering principles is given in *Chapter 2*, and the instruments used for the study are described in *Chapter 3*. The development of the aerosol observation methodology by the cloud radar is presented in *Chapter 4* together with the results of its application. Following, in *Chapter 5*, is the analysis and examination of the lidar simultaneous measurements. In *Chapter 6* the synergy between cloud radar and lidar is explored, the aerosol optical properties are retrieved for their observations, and enlarged aerosol size distributions are obtained by combining the information. The effects of giant aerosols on the local meteorology are studied in *Chapter 7*, and the discussion and conclusions are given in *Chapter 8*.

1

Atmospheric aerosols

Aerosols are airborne suspensions of minuscule particles, which span a range in diameters from nanometers to tens and sometimes hundreds of micrometers (Seinfeld and Pandis, 2006). They exhibit high variability regarding their composition, size, concentration and shape; it is related to the inhomogeneity of the emitting sources and the chemical and physical processes that occur between the emission and removal processes. The different aerosol characteristics give them different properties, and therefore they interact in different ways with the environment.

Atmospheric aerosols have important effects on both the environment and human life. First, they affect the meteorological and climate system both in direct and indirect ways. Directly, they affect the radiation budget by interacting with the solar and thermal radiation. Indirectly, they modify the properties of clouds by acting as Cloud Condensation Nuclei (CCN), upon which cloud droplets and ice crystals form. Second, aerosols play an important role in air quality and human health, since they can cause or enhance respiratory, cardiovascular, infectious and allergic diseases (Pöschl, 2005). Third, aerosols can affect transportation, as happened during the spring of 2010, when the Eyjafjallajökull volcano eruption in Iceland caused an enormous disruption to air traffic across Western and Northern Europe (Pappalardo et al., 2013). Finally, aerosols have an impact on the biosphere by carrying nutrients to oligotrophic ecosystems such as oceans. Considering all these effects, it is clear how important the study of the atmospheric aerosols becomes. Unfortunately, the complex processes that characterize the aerosols from emission to removal give them a great variability, which makes them an atmospheric component that is especially difficult to observe and monitor.

Figure 1.1 shows the global mean positive and negative radiative forcings since 1750 (IPCC, 2013). Aerosols affect the radiation budget directly and indirectly and are grouped accordingly. The direct effect has mainly negative effect on radiative forcing with a high level of confidence, even if the uncertainty interval is large. The indirect effect ("Cloud adjustments due to aerosol" in the *Fig. 1.1*) was quantified as a negative forcing, with a low level of confidence and a big uncertainty interval. When the radiative forcing by aerosols is compared to the other emissions quantifications in terms of uncertainty and level of confidence, it becomes imperative to monitor and expand our knowledge on atmospheric aerosols.

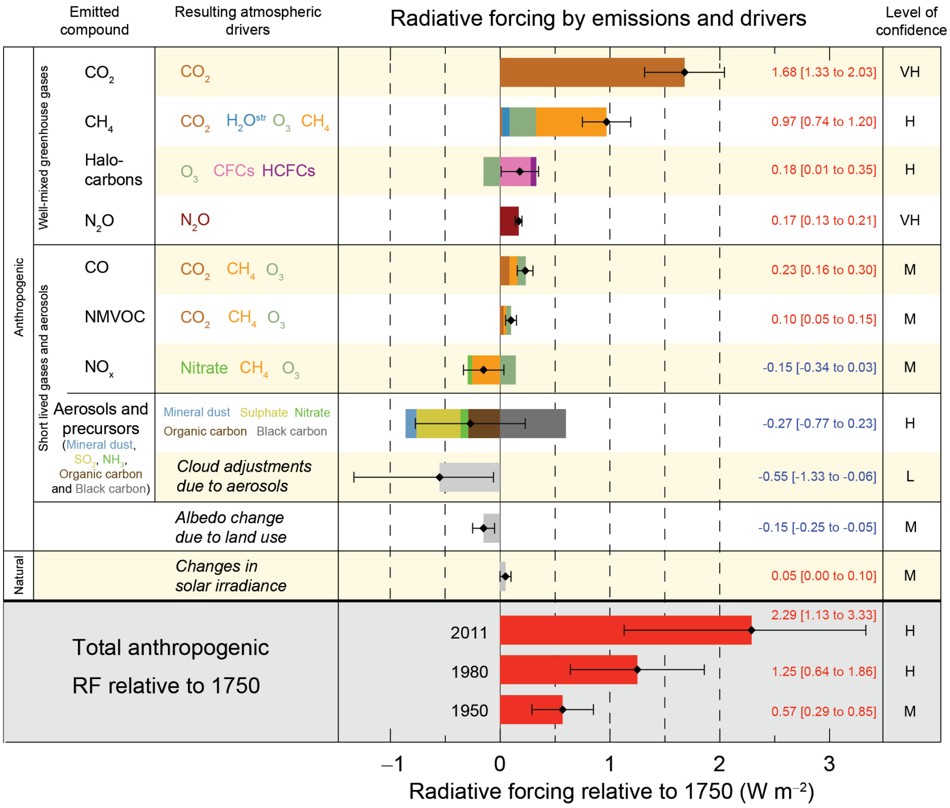

Figure 1.1: *Radiative forcing estimates in 2011 relative to 1750 and aggregated uncertainties for the main drivers of climate change. The best estimates of the net radiative forcing are shown as black diamonds with corresponding uncertainty intervals; the numerical values are provided on the right of the figure, together with the confidence level in the net forcing (VH – very high, H – high, M – medium, L – low, VL – very low). Figure SPM.5 adapted from IPCC (2013).*

The aerosol direct and indirect effects are depicted in *Fig. 1.2*. The direct effect is the mechanism by which particles scatter and absorb the short- and long-wave radiation. The indirect effect is the mechanism by which aerosol particles modify the properties of clouds. The aerosol indirect effect differences between an unperturbed (clean) cloud and a cloud with a higher aerosol load (polluted cloud) are shown in *Fig. 1.2*. In a clean cloud, where there are fewer and bigger droplets, the absorption is low and the transmission high. This results in a reduced cloud albedo. On the other hand, given the same amount of liquid water, in a polluted cloud there are more and smaller droplets, the absorption is higher and the transmission lower. This leads into an enhanced cloud albedo, as described by Twomey (1974). Regarding the precipitation formation, the collision-coalescence process takes place faster in clean clouds, so they produce more precipitation and have a shorter lifetime. In polluted clouds, this process is less efficient, delaying the raindrop formation and hence producing less precipitation and increasing the clouds lifetime (Albrecht, 1989).

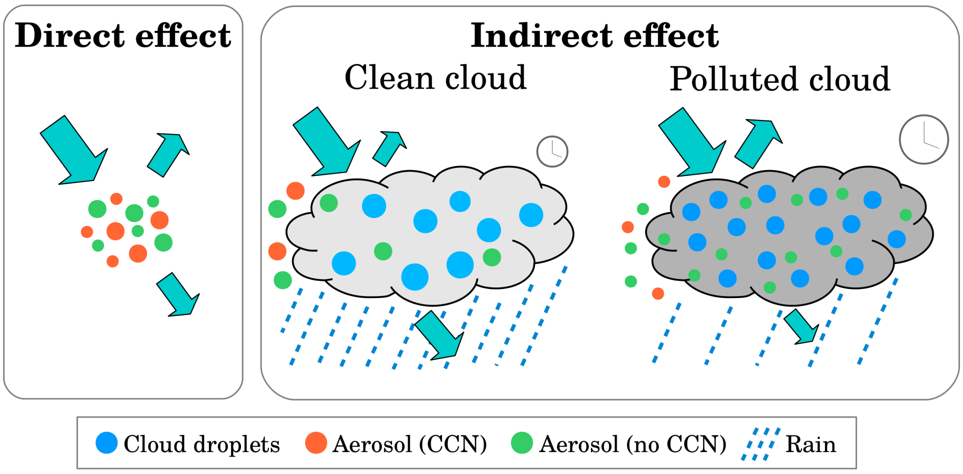

Figure 1.2: *Schematic diagram of the aerosol direct and indirect effects.*

The aerosol indirect effect can be linked to the giant and ultragiant particles. They are particularly big aerosols, with diameters over 5 μm, and can act as Giant Cloud Condensation Nuclei (GCCN) and Ice Nuclei (IN). The clouds formed upon GCCN are characterized by a low concentration of big cloud droplets, a reduced albedo, a high collision-coalescence efficiency and hence a fast precipitation formation. It is the case of warm rain processes, in which the precipitation results from the coalescence of droplets above freezing level. This process has been the focus of several studies. Feingold et al. (1999) and Eagan et al. (1974) found that GCCN expedite specially warm rain processes, while Dagan et al. (2015) showed that the GCCN effect is important only when the aerosol concentration is higher than the optimal for the maximum rain generation. When acting as IN, giant aerosols increase the temperature at which ice is formed in the atmosphere from around -42$^{\circ}C$ to about -10$^{\circ}C$. Mineral dust, for example, is an efficient IN (DeMott et al., 2003).

Aerosols can be classified according to their origin (natural vs. anthropogenic), formation mechanism (primary vs. secondary), source or size. In the following sections, the last two are described in more detail.

1.1 Aerosol types

The originating source of aerosols has a strong influence on their properties. Therefore, aerosol types are usually classified into different categories such as volcanic, marine, biomass burning, fossil-fuel combustion and industrial aerosols (Seinfeld and Pandis, 2006). The characteristics of the different aerosol types according to their sources are given below.

Arid and semi-arid regions are a major source of atmospheric aerosols. The particles originated in these regions are mineral particles, alias dust particles, created mainly by physical weathering and, in a lower rate, by chemical weathering of rocks and minerals. Generally, the term desert dust refers to particles smaller than 62.5 μm: particles between 4.0 and 62.5 μm are referred to as slit and particles smaller than 4 μm as clay (Goudie and Middleton, 2006). The main sources of dust are the large arid areas of the world: the African continent (in particular the Saharan desert), the Arabian Peninsula and the Asian continent (Prospero et al., 2002; Marticorena, 2007). Dust particles that are originated in these arid areas can be transported over long distances by strong winds and convective processes (D'Almeida et al., 1991).

Volcanic eruptions are an important source of atmospheric aerosols. They inject great amounts of material into the atmosphere: tephra (particles over 2 *mm*), volcanic ash (smaller than 2 *mm*), and gases. Most of the aerosols settle only a few tens of kilometers away from the volcano but, as with desert dust, particles smaller than 10 μm can travel thousands of kilometers and affect wider areas (Ayris and Delmelle, 2012; Wilson et al., 2012). Great quantities of gases are emitted together with the volcanic ash during an eruption. Some of them can lead to formation of secondary aerosol, as for example the sulphur dioxide transforms into sulphate particles.

The sea surface is also an important aerosol source. Marine aerosols include sea-salt and secondary particles. Sea-salt aerosols form when winds and waves force air bubbles to burst at the sea surface, while secondary marine particles are created through gas-to-particle conversion in the Marine Boundary Layer (MBL). Sea-salt particles have, mainly, diameters larger than μm, while the secondary particles dominate the sub-micron range (O'Dowd and Leeuw, 2007).

Forest and agricultural fires can produce large quantities of aerosols, such as ash, plant fibers, soil dust, organic matter and soot. The burning biomass influences strongly the physical and chemical aerosol characteristics, reflecting the different emission conditions.

Vegetated areas are also an aerosol source, even if their contribution to the total atmospheric aerosol population is low. These areas release pollen, spores and plant debris in the atmosphere. These aerosols are usually large and they often serve as sites on which cloud drops and ice crystals form (Jacobson, 2002).

The major anthropogenic aerosol sources are fossil-fuel combustion and industrial sources. Particles can originate from the combustion of coal, oil, gasoline, diesel and biomass. Only a small fraction of the originated aerosols by these burning processes are primary, as is the case of residual ash particles; the rest are produced by gas-to-particle transformation of precursor cases. Thus, fine mode particles dominate the aerosol type characterized by this source.

The strength of the different aerosol sources have great variations, and can be described by the emitted mass flux. Typical estimates of the annual emissions of different sources are summarized in *Table 1.1*, showing that the major aerosol sources are the arid and semi-arid regions together with the oceans. These mass fluxes, though, are not simply related to the sources impact on environment and climate. As an example, PM2.5 particles (the fraction of particulates in air with size $< 2.5\ \mu m$) are of great concern nowadays, as they can penetrate deep into the lungs and so pose significant health risks.

Table 1.1: *Global source emission estimations for major aerosols sources. Estimates adapted from Hobbs (1993), Hinds (1999) and Seinfeld and Pandis (2006).*

Origin	Source	Emission [Tg / *year*]
Natural	Dust	1000 - 3000
	Sea salt	1000 - 3000
	Volcanic	15 - 90
	Biogenic	50
	Gas-to-particle	200 - 1300
Anthropogenic	Industrial and fossil fuel burning	300
	Biomass burning	100 - 450

1.2 Aerosol sizes

Aerosol particles have diameters that span several orders of magnitude. Thereby, it is useful to distinguish atmospheric aerosol particles in different modes according to their diameters. They are commonly divided into four modes: the nucleation mode, the Aitken mode, the accumulation mode, and the coarse mode, as shown in *Fig. 1.3*. Anthropogenic aerosols occur mainly in submicron range ($< 1\ \mu m$ radius), and natural aerosols in the supermicron range ($> 1\ \mu m$ radius): soot and sulphuric acid are Aitken particles, while biomass burning smoke usually lies within the accumulation mode. Mineral dust, sea salt, pollen and volcanic particles are coarse mode particles.

Usually, each of the aerosol modes is represented by an individual log-normal size distribution (see *Fig. 1.3*), characterising the variation of concentration (i.e. number, surface area or volume) with size. Aerosol distributions are normally plotted on a logarithmic x-axis in order to display the several orders of magnitude over which the aerosol sizes vary in an adequate manner. The log-normal distribution for the number concentration, n_N, is given as (Seinfeld and Pandis, 2006):

$$n_N(D) = \frac{N}{\sqrt{2\pi}\; D\; ln\; \sigma_g} exp\left[\frac{-\left(ln\; D - ln\; \overline{D}_g\right)^2}{2\; ln^2\; \sigma_g}\right] \tag{1.1}$$

where N is the total aerosol number concentration, D the particle diameter, and $\overline{D}_g$ and σ_g the mean and standard deviation of the distribution respectively.

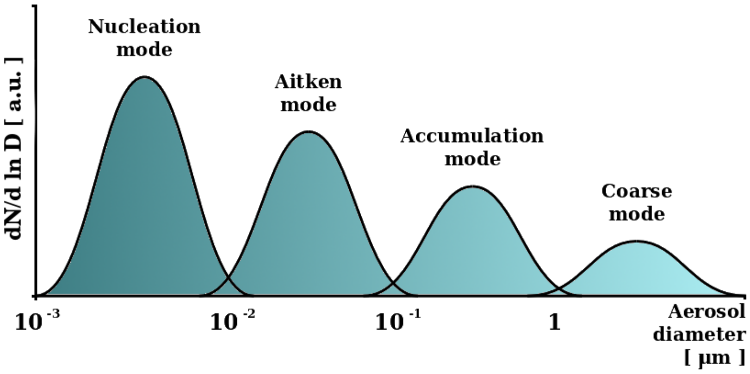

Figure 1.3: *Aerosol log-normal number distribution for the nucleation, Aitken, accumulation and coarse modes.*

Aerosol ensembles can also be described by their mean and integral properties (Ansmann and Müller, 2005), such as the effective radius r_{eff}, which is the surface-area-weighted mean radius:

$$r_{eff} = \frac{\int n(r)\; r^3\; dr}{\int n(r)\; r^2\; dr} \tag{1.2}$$

the total surface-area concentration a_t:

$$a_t = 4\pi \int n(r)\; r^2\; dr \tag{1.3}$$

and the total volume concentration v_t:

$$v_t = \frac{4\pi}{3} \int n(r)\; r^3\; dr \tag{1.4}$$

where n is the number of particles and r the particle geometric radius.

In the case of an aerosol log-normal distribution, the effective radius can be also expressed as (Grainger, 2015):

$$r_{eff} = \frac{exp\left(3r_g + {}^9/_2\sigma_g^2\right)}{exp\left(2r_g + {}^4/_2\sigma_g^2\right)} = exp\left(r_g + \frac{5}{2}\sigma_g^2\right) = r_g\ exp\left(\frac{5}{2}\sigma_g^2\right) \tag{1.5}$$

where r_g is the mean radius of the distribution and σ_g the standard deviation.

1.3 Aerosol transport

Once aerosols are injected into the atmosphere, they remain in it until they are removed by dry and wet deposition processes. In the meantime, the properties of these particles can change, either by chemical conversions or by collision and coagulation with other aerosol particles.

Aerosols can be removed from the atmosphere by various processes that can be roughly separated into two categories: dry deposition and wet scavenging (Seinfeld and Pandis, 2006). Dry deposition describes all the aerosol removal processes that do not involve water. The principal dry deposition process is gravitational settling, whose efficiency is determined mainly by the aerosol mass. This process is described by the aerosols terminal velocity. Wet scavenging describes all the processes that involve the removal of aerosols by hydrometeors, and can be divided into in-cloud and below-cloud. In-cloud scavenging includes nucleation and interstitial scavenging, the former being much more efficient than the latter. This is the main removal mechanism of sub-micron particles that are not removed efficiently by other processes. Below-cloud scavenging refers to the removal of aerosols when falling hydrometeors impact with them.

The efficiency of dry deposition by gravitational settling depends, mainly, on the particle size. The settling velocity v, also called terminal or Stoke's velocity, for an aerosol particle falling in the atmosphere is defined as:

$$v = \frac{2}{9}\left(\frac{\rho_{aer} - \rho_{air}}{\mu_{air}\ g\ r_{aer}^2}\right) \tag{1.6}$$

where ρ_{aer} and ρ_{air} are the aerosol and air density respectively, μ_{air} is the air viscosity, g is the acceleration of gravity and r_{aer} is the aerosol radius. *Figure 1.4* shows which is the settling velocity for aerosol particles of different aerosol radii, considering standard atmospheric pressure and temperature (1013.25 *hPa* and 293.15 *K* respectively) and an aerosol density of 2.6 $g\ cm^{-3}$, which is used for recent studies of Saharan dust (i.e. Ansmann et al., 2012; Binietoglou et al., 2015). It is clear that large particles are removed from the atmosphere much faster than the smaller ones.

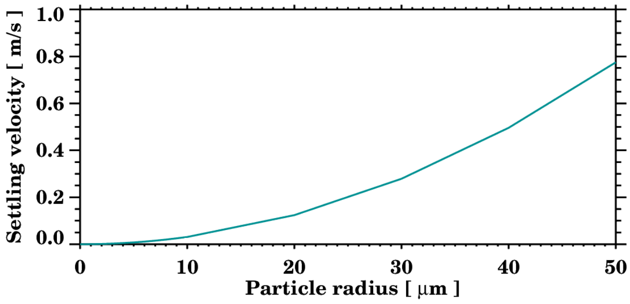

Figure 1.4: *Aerosol settling velocity calculated using equation 1.6 assuming a standard atmosphere (1013.25 hPa and 293.15 K) and a particle density of 2.6* $g\ cm^{-3}$.

In order to get an initial idea of the aerosols residence time in the atmosphere depending on their size, the time necessary for particles of different sizes to fall 1 *km* in the atmosphere is reported in *Fig. 1.5*. The time different particles need to fall 1 *km* by gravitational settling depends strongly on their size: a particle of 100 *nm* radius would need 10 *years*, one of 1 μm 37 *days*, one of 10 μm 9 *hours* and a 100 μm particle only 5 *minutes*.

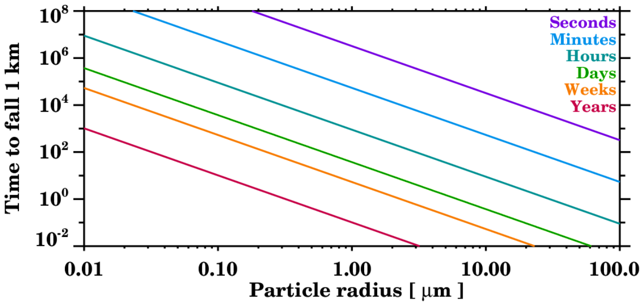

Figure 1.5: *Time for particles to fall 1 km in the atmosphere by sedimentation. The units of the vertical axis correspond to the units of each category: seconds, minutes, hours, days, weeks or years.*

The atmospheric residence time for tropospheric aerosols is typically about a week. For a mean atmospheric transport velocity of 5 $m\ s^{-1}$, this residence time corresponds to a transport distance of 3000 *km* (Jacobson, 2002). Therefore, the aerosol particles that remain in the atmosphere for a considerable period of time can travel a long way from their sources. Saharan dust, for example, is regularly transported over the Atlantic Ocean and the Mediterranean sea to America and Europe (Prospero, 1997).

In general, the mass median diameter of mineral dust over the oceans is typically 2 – 3 μm, while the larger-sized particles (tens of micrometers in diameter) are deposited relatively rapidly, generally within hundreds to a thousand kilometers of the source (Prospero, 1999). Guerzoni and Chester (1996) found a bimodal particle size distribution of the Saharan dust outbreaks in Sardinia, the two modes being between 2 and 4 μm and 15 and 30 μm. Maring et al. (2003) found indistinguishable normalized Saharan dust size distributions of particles smaller than 7.3 μm over the Canary Islands and Puerto Rico, indicating these particles were not preferentially removed during atmospheric transport. Schütz et al. (1981) also observed the presence of dust particles in the marine troposphere larger than is consistent with Stokes gravitational settling alone controlling removal. This indicates that atmospheric processes counteract the effects of gravitational settling.

The spatial distribution of aerosol particles in the atmosphere is far from uniform due to the non-uniform distribution of sources, processes and the different atmospheric residence times. *Figure 1.6* shows the distribution of aerosols across the globe during 11 *years* of measurements, which illustrates their heterogeneous distribution.

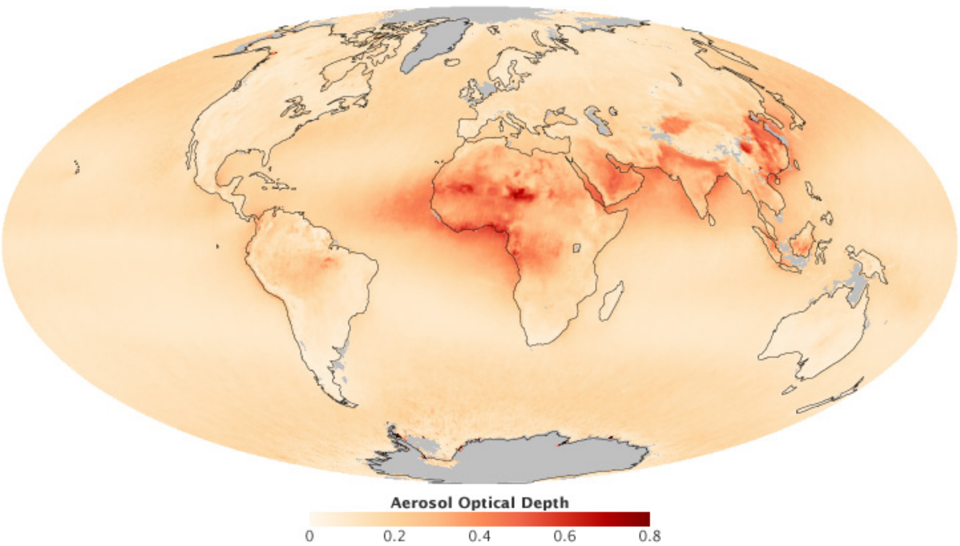

Figure 1.6: *Average distribution of aerosols from June 2000 through May 2010, measured by the Multi-angle Imaging Spectroradiometer (MISR). Red indicates high concentrations of aerosols, beige indicates low concentrations. Map by Robert Simmon. Source: "* `http://earthobservatory.nasa.gov/Features/Aerosols/page5.php`*".*

2

Scattering principles

The way in which the atmospheric constituents interact with the electromagnetic waves is widely used in remote sensing techniques to observe them.

Scattering is a general physical process where some forms of radiation, such as light and sound, or moving particles, are forced to deviate from a straight trajectory by one or more localized non-uniformities in the medium through which they travel. When an electromagnetic wave impinges on a particle, part of its energy will be intercepted. This energy can be either scattered or absorbed, the latter implying an energy type conversion. The combined effect of scattering and absorption is called extinction.

The types of non-uniformities which can cause scattering, sometimes known as scatterers or scattering centers, are too numerous to list, but a small sample includes particles, bubbles, droplets, density fluctuations in fluids, surface roughness and cells in organisms. The effects of such features on the path of almost any type of propagating wave or moving particle can be described in the framework of scattering theory.

Electromagnetic waves are one of the best known and most commonly encountered forms of radiation that undergo scattering. Several different aspects of electromagnetic scattering are distinct enough to have conventional names. Major forms of elastic light scattering (involving negligible energy transfer) are Rayleigh scattering and Mie scattering. Inelastic scattering includes Brillouin scattering, Raman scattering, inelastic Xray scattering and Compton scattering. Raman scattering consists in the inelastic scattering of a photon, in which the absorption of energy causes a wavelength change related to the change of energy of a molecule due to a transition to another energy level.

Light scattering is one of the two major physical processes that contribute to the visible appearance of most objects, the other being absorption. When looking at how a particle will scatter, the relation between the incident wavelength and the particle size is crucial. Models of light scattering can be divided into three domains based on a dimensionless size parameter, x, which is defined as:

$$x = \frac{2\,\pi\,r}{\lambda} \tag{2.1}$$

where r is the radius of a particle and λ is the wavelength of incident radiation. Based on the value of x, these domains are:

- Geometric optics scattering ($x \gg 1$): scatterers are much larger than the incident wavelength. The laws of geometric optics are sufficient to describe the interaction of light with the particle.
- Mie scattering ($0.1 \leq x \leq 100$): scatterers are about the same size as the incident wavelength. The shape of the scattering center becomes much more significant and the theory only applies to spheres and, with some modification, spheroids and ellipsoids. Closed-form solutions for scattering by certain other simple shapes exist, but no general closed-form solution is known for arbitrary shapes.
- Rayleigh scattering ($x \ll 0.1$): scatterers are much smaller than the incident wavelength. The exact shape of the scattering center is usually not very significant and can often be treated as a sphere of equivalent volume. The degree of scattering varies as a function of the ratio of the particle diameter to the wavelength of the radiation, along with many other factors including polarization, angle, and coherence.

These scattering domains can be observed in *Fig. 2.1* for different incident wavelengths and particle sizes. Moreover the figure categorizes the instruments and observed targets according to the scattering domains.

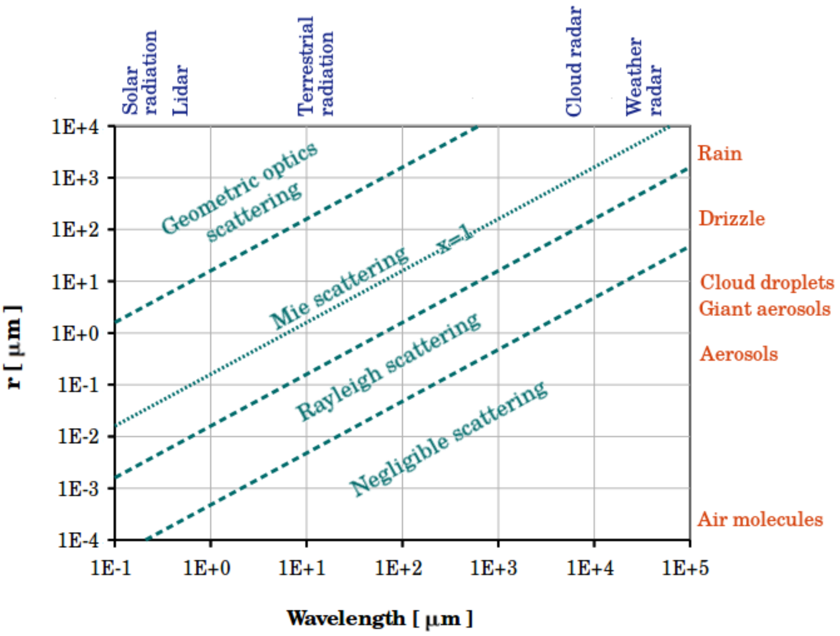

Figure 2.1: *Electromagnetic waves scattering domains depending on the incident wavelength and the particle radius. Adapted from the Geography Department of the University of California.*

Both Mie and Rayleigh scattering are considered elastic scattering processes, in which the energy (and thus wavelength and frequency) of the light is not substantially changed. However, electromagnetic radiation scattered by moving scattering centers does undergo a Doppler shift, which can be detected and used to measure the velocity of the scatterers in forms of techniques such as lidar and radar. This shift involves a slight change in energy.

2.1 Scattering parameters

The scattering of an electromagnetic wave by a particle depends on the following parameters:

- Phase function ($p(\theta)$): is a normalized measure of how the intensity of the scattered light varies with scattering angle θ measured respect to the radiation propagation direction. The phase function can be expressed as (Henyey and Greenstein, 1941):

$$p(\theta) = \frac{1}{4\,\pi} \frac{1-g^2}{[1+g^2-2\,g\,cos(\theta)]^{3/2}} \tag{2.2}$$

ranging this function from backscattering ($\theta = 180°$) through isotropic scattering to forward scattering ($\theta = 0°$) by the variation of the asymmetry parameter g. It can be written as function of $\mu = cos(\theta)$:

$$p(\mu) = \frac{1}{2} \frac{1-g^2}{[1+g^2-2\,g\,\mu]^{3/2}} \tag{2.3}$$

Figure 2.2 presents the phase function for spherical particles with different size parameters. When the size parameter is small and falls in the Rayleigh regime ($x < 0.1$), the forward and backward scattered radiation is the same, and both lobes are equal (see purple and blue lines). For size parameters falling in the Mie regime ($0.1 \le x \le 100$), by increasing the size parameter the forward lobe becomes more important and the backward lobe magnitude diminishes. This effect can be seen, for example, by comparing the green ($x = 1$) and orange lines ($x = 5$).

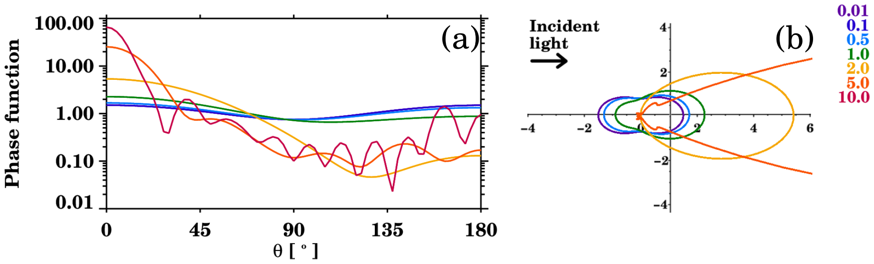

Figure 2.2: *Phase function for spherical particles with different size parameters, indicated by different colours. (a) Phase function depending on the scattering angle. The scattering angle θ is 0° for forward scattering and 180° for backwards scattering. (b) Polar plot of the phase function. Calculations were performed using the code presented in Mishchenko and Travis (1998) using a refractive index of 1.45 - 0.005i.*

- Asymmetry parameter (g): indicates the degree of scattering in the forward direction. Its range varies from -1 (i.e. all radiation is backward scattered, like a mirror) to 1 (pure forward scattering). For $g = 0$, the radiation is scattered equally in all the directions.

- Cross-section (C): describes how much of an incident beam's intensity is removed in terms of the area of the beam on a plane perpendicular to the beam. The scattering cross-section, C_{sca}, describes how much is scattered, the extinction cross-section, C_{ext}, how much is removed, and the absorption cross-section, C_{abs}, how much is absorbed. The extinction, scattering and absorption cross-sections are defined as:

  $$C_{ext} = \pi\, r^2\, Q_{ext} \qquad C_{sca} = \pi\, r^2\, Q_{sca} \qquad C_{abs} = \pi\, r^2\, Q_{abs} \tag{2.4}$$

  where r is the radius of the particle and Q the efficiency.

- Efficiency (Q): it is closely linked to the cross-section, and indicates what proportion of the incident beam on a particle is diverted into a certain process. For this reason, efficiencies can be defined as:

  $$Q_{ext} = \frac{C_{ext}}{G} \qquad Q_{sca} = \frac{C_{sca}}{G} \qquad Q_{abs} = \frac{C_{abs}}{G} \tag{2.5}$$

  where G is the cross sectional area of a particle, projected onto a plane perpendicular to the direction of incident light. In the case of a sphere of radius r_0, $G = \pi\, r_0^2$.

- Single Scattering Albedo (ω): is the ratio between the scattering and the total extinction efficiencies:

  $$\omega = \frac{Q_{sca}}{Q_{ext}} \tag{2.6}$$

  where $Q_{ext} = Q_{sca} + Q_{abs}$. It is a unitless parameter and varies from 0 (extinction is totally due to absorption) to 1 (extinction is totally due to scattering).

Based on the properties of a single scatterer previously described, quantities relative to an ensemble of scatterers can be defined, such as the volume extinction coefficient, α, of the medium:

$$\alpha = \sum_{i}^{n} N_i\, C_{ext}^{i} \tag{2.7}$$

where n corresponds to the different types of scatterers and N_i to the number of scatterer particles of type i. It is expressed by unit of path length, i.e. m^{-1}.

A beam of light with intensity I_0 that passes through a layer of this medium will be attenuated, and the new intensity is given by:

$$I = I_0 \; e^{-\int_0^H \alpha(r) \; dr} \tag{2.8}$$

where H is the thickness of the layer. The quantity in the exponential, $\int_0^H \alpha(r) \; dr$, is called optical depth, and describes how much extinction occurs when light travels through a medium. The optical depth varies with the wavelength, λ, as:

$$\tau \sim \lambda^{å} \tag{2.9}$$

where å is called the Ångström exponent and describes the extinction dependence on the wavelength.

In the same way as for the extinction coefficient, the backscatter coefficient, β, which characterizes the amount of light that is scattered towards the direction opposite to the direction of light propagation ($\theta = \pi$), can be defined as:

$$\beta = \sum_i^n N_i \frac{dC_{sca}}{d\Omega}(\pi) \tag{2.10}$$

where Ω is the solid angle and β is expressed by unit of path length and solid angle (i.e. $m^{-1}sr^{-1}$).

The ratio of the extinction and the backscatter coefficients depends on the microphysical properties of the scatterer and is called lidar ratio, S:

$$S_\lambda = \frac{\alpha(\lambda)}{\beta(\lambda)} \tag{2.11}$$

In *Chapter 3*, the properties and the importance of these parameters will be discussed.

2.2 Polarization

At every scattering process, either the degree or the nature of the electromagnetic wave polarization can change. A convenient way to describe the polarization state of light is through the Stokes vector. The Stokes vector can be defined through a set of ideal measurements (Bass et al., 2009). The light intensity measurements performed at various positions of an ideal polarizer in respect to the incident electromagnetic wave can be noted as:

- P_H: horizontal linear polarizer
- P_V: vertical linear polarizer
- P_{45}: 45° linear polarizer
- P_{135}: 135° linear polarizer
- P_R: right circular polarizer
- P_L: left circular polarizer

Following these definitions, the Stokes vector can be defined as:

$$S = \begin{bmatrix} S_0 \\ S_1 \\ S_2 \\ S_3 \end{bmatrix} = \begin{bmatrix} P_H + P_V \\ P_H - P_V \\ P_{45} - P_{135} \\ P_R - P_L \end{bmatrix} \tag{2.12}$$

The Stokes parameters, S_n, are a complete description of the state of light (Van de Hulst, 1981): S_0 represents the total intensity beam, S_1 the horizontally or vertically polarized light, S_2 the 45° or 135° polarized light, and S_3 the circularly polarized light. Therefore, we can define the degree of polarization DoP as:

$$DoP = \frac{\sqrt{S_1^2 + S_2^2 + S_3^2}}{S_0} \tag{2.13}$$

It is 1 for fully polarized light and 0 for unpolarized or natural light.

A scattering process transforms the incident light state from S_i to S_s:

$$S_s = F \cdot S_i \tag{2.14}$$

where F is the Müller matrix:

$$F = \begin{bmatrix} F_{11} & F_{12} & F_{13} & F_{14} \\ F_{21} & F_{22} & F_{23} & F_{24} \\ F_{31} & F_{32} & F_{33} & F_{34} \\ F_{41} & F_{42} & F_{43} & F_{44} \end{bmatrix} \tag{2.15}$$

The elements of this matrix depend on the direction of radiation propagation and the wavelength, and describe completely the properties of a scattering element.

For a single particle, only 7 of the 16 matrix elements are independent. For an ensemble of scatterers, the total Müller matrix is calculated as the sum of the individual matrices and it has 16 independent elements. If the ensemble has certain symmetry relations, the form of the matrix can be simplified (Van de Hulst, 1981). For example, an ensemble of scatterers that contain their mirror image in equal number and in random orientations can be described by a matrix with only 6 independent elements:

$$F = \begin{bmatrix} F_{11} & F_{12} & 0 & 0 \\ F_{12} & F_{22} & 0 & 0 \\ 0 & 0 & F_{33} & F_{34} \\ 0 & 0 & -F_{34} & F_{44} \end{bmatrix} \tag{2.16}$$

2.3 Scattering calculations

The interaction of electromagnetic radiation with a particle cannot be solved analytically, and therefore accurate calculations for real particles are difficult. Moreover, these interactions are conditioned by many different parameters, such as the wavelength of the radiation, size, shape, composition and roughness of the particle and its complex refractive index. Nevertheless, good results can be obtained by approximating the particles using simplified shapes such as homogeneous spheres and spheroids.

The Mie theory describes the scattering using the spherical approximation, which is valid for many categories of real particles, such as urban and sea-salt particles. Many of the particles, though, cannot be accounted for as spheres, and for those the Mie theory does not give satisfactory results. It is the case of mineral dust and volcanic ash.

Several approaches have been proposed to model the optical properties of such particles. The most widely used approach is to approximate the aerosol population by a mixture of randomly-oriented spheroids (Mishchenko et al., 1997; Dubovik et al., 2006). While the true shape of the atmospheric aerosols is probably not spheroidal, the light scattered by an ensemble of particles with random orientations and shapes, makes the individual scattering characteristics of each particle less pronounced.

In the specific case of non-spherical particles with rotational symmetry scattering field calculation, the T-matrix approach is specially suited (Mishchenko and Travis, 1998). The T-matrix method is based on the expansion of the incident and scattered fields in vector spherical wave functions, which are used to compute the electromagnetic scattering by single, homogeneous non-spherical particles (Mishchenko, 1993). The T-matrix approach has been shown to be an efficient method for scattering calculations involving rotationally-symmetric non-spherical particles, such as spheroids, cylinders, two-sphere clusters and Chebyshev particles (Mishchenko, 2000).

3

Aerosol observations

The research presented in this thesis has been carried out at the Consiglio Nazionale delle Ricerche - Istituto di Metodologie per l'Analisi Ambientale (CNR-IMAA) Atmospheric Observatory (CIAO). It is located in Tito Scalo, Potenza, Southern Italy, on the Apennine mountains (40.60°N, 15.72°E), less than 150 *km* from the West, South and East coasts (see *Figure 3.1*). The site is in a plain at 760 *m* of altitude and it is surrounded by low mountains (< 1100 *m a.s.l.*). Accordingly, it operates in a typical mountain weather strongly influenced by Mediterranean atmospheric circulation, resulting in generally dry, hot summers and cold winters (Madonna et al., 2011). The site is of particular interest for studying aerosol properties because it is affected by a quite large number of Saharan dust intrusions (Mona et al., 2014), and it is located 300 *km* far from the Etna volcano (Pappalardo et al., 2004).

In this chapter, a description of the instruments used in the study presented is given. For the aerosol observations, the main instruments used are two multi-wavelength Raman lidars and a Ka-band Doppler radar. To this end, complementary observations are employed. For instance, existing remote sensing and in-situ instruments on site are implemented.

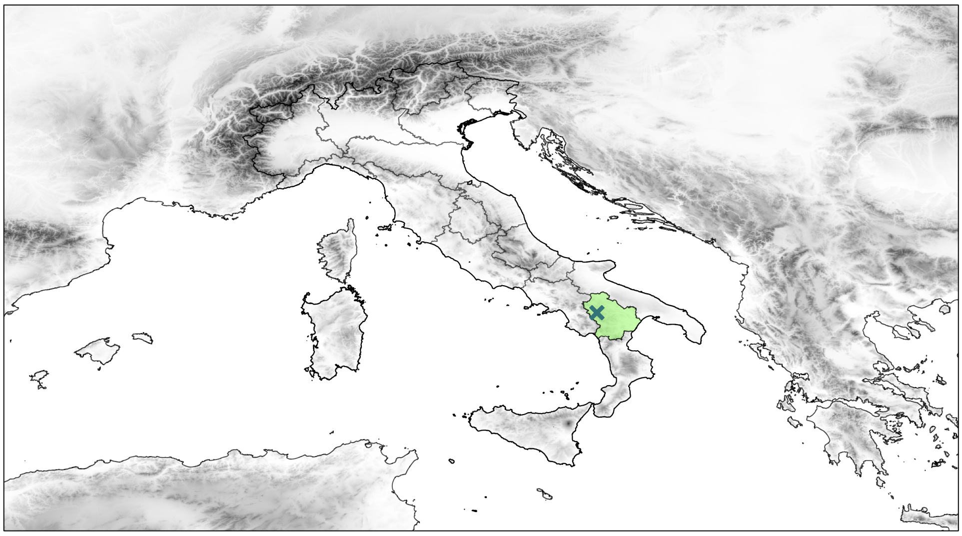

Figure 3.1: *Location of the CNR-IMAA Atmospheric Observatory (CIAO), indicated by a dark green cross. The light green area corresponds to the Basilicata region, in which the observatory is located.*

3.1 Lidar

Lidar stands for LIght Detection And Ranging, and is an active remote sensing instrument. A laser beam is emitted into the atmosphere and the light backscattered by its constituents is measured. There are several system designs, being each one optimized to probe a specific atmospheric region (Weitkamp, 2006).

In this study, we focus on the tropospheric observations done by the two multi-wavelength Raman lidars operative at CIAO: the Potenza EArlinet Raman Lidar (PEARL) and the MUltiwavelength System for Aerosol (MUSA) (Madonna et al., 2011). Both systems are designed to provide measurements for the retrieval of optical and microphysical properties of the atmospheric particles. Musa (*Fig. 3.2a*) is a compact and transportable system, while PEARL (*Fig. 3.2b*) is permanently at the observatory. Both systems are based on a Nd:YAG laser (20 Hz and 50 Hz repetition rate for MUSA and PEARL respectively), emitting at three laser wavelengths (355, 532 and 1064 *nm*) and have three optical channels devoted to the detection of the radiation elastically backscattered and 2 optical channels to detect the Raman radiation backscattered from the atmospheric N_2 molecules at 387 and 607 *nm*. Pearl is equipped with an additional receiver for the H_2O molecular Raman backscatter at 407 *nm*, for the measurement of the water vapour mixing ratio profile. In this way, both MUSA and PEARL are able to measure unconstrained aerosol extinction and backscatter coefficients. The elastic channel at 532 *nm* is split into parallel and perpendicular polarization components, which allows to retrieve the particles depolarization. The temporal resolution used in the measurements is of 1 minute for both systems, whilst the vertical raw space resolution is 3.75 *m* for MUSA and 7.5 *m* (at 1064 *nm*) and 15 *m* (at the other wavelengths) for PEARL.

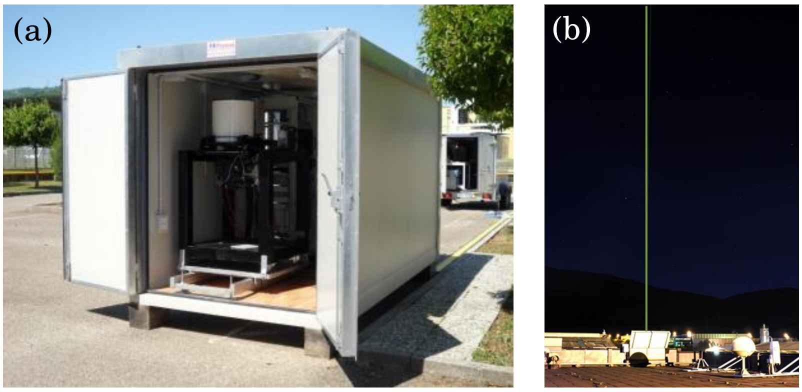

Figure 3.2: *Raman lidars at CIAO: MUSA (a) and PEARL (b).*

From the lidar measurements, the following optical properties can be obtained:

- **Extensive properties**: they depend on the aerosol load.
  - Backscatter coefficient (β): fraction of the light per solid angle scattered at an angle of 180° with respect to the incident radiation direction. It is expressed in $m^{-1}\ sr^{-1}$.
  - Extinction coefficient (α): measure of how much light energy is lost per path length unit. It is usually expressed in m^{-1}, and is obtained by measuring the Raman backscattered energy.
- **Intensive properties**: they depend on the particle type, also referred as bulk properties.
  - Lidar ratio (S): extinction to backscatter ratio (i.e. Müller et al., 2007). It is expressed in *sr*.

- Ångström exponent, backscatter or extinction related ($Å_\beta$ or $Å_\alpha$): describes the spectral dependence of the backscatter or extinction coefficients retrieved at the different wavelengths, giving an indication of the particle size (Kaufman, 1993). It is *unitless*.
- Linear particle depolarization ratio (δ_p): the ratio of the perpendicular to the parallel component of the particle backscatter coefficient at a certain wavelength. It gives information on the shape and size of the particles and is usually expressed as a *percentage*.

As already noted, the intensive properties depend on the particle type, and can therefore be used to distinguish between different aerosol types. In *Figure 3.3*, the Ångström exponent, lidar ratio and particle linear depolarization ratio for different aerosol types is shown.

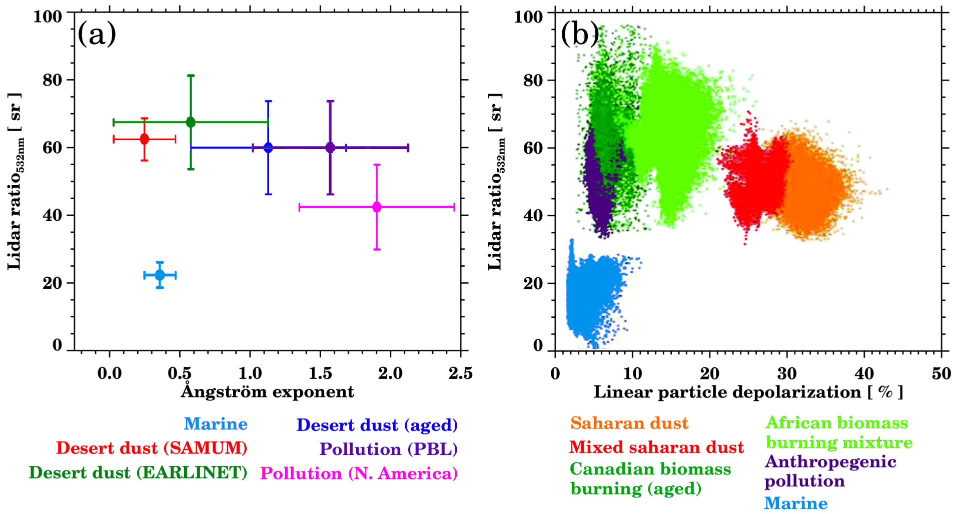

Figure 3.3: *(a) Ångström exponent (backscatter related) versus lidar ratio at 532 nm for different aerosol types according to Müller et al. (2007). Error bars show the standard deviation of the mean values. (b) Particle linear depolarization ratio versus lidar ratio at 532 nm for different aerosol types from Groß et al. (2013): each point represents a measurement point.*

3.1.1 Lidar equation

In the following, the basic lidar operation principles are described together with the main methods to process its data.

The power $P(R,\lambda)$ measured by the lidar system from the range R and at the wavelength λ can be described by the lidar equation (Wandinger, 2005):

$$P(R,\lambda) = \underbrace{P_0 \frac{c\,\tau}{2} A \eta}_{\substack{\text{System}\\\text{factor}}} \underbrace{\frac{O(R)}{R^2}}_{\substack{\text{Geometric}\\\text{factor}}} \underbrace{\beta(R,\lambda)}_{\text{Backscatter}} \underbrace{exp\left[-2\int_0^R \alpha(r,\lambda)\,dr\right]}_{\text{Transmission}} \tag{3.1}$$

where:

- the *system factor* summarizes the performance of the lidar system and is completely determined by the lidar setup; P_0 is the average power of a single laser pulse, c is the speed of light, τ is the temporal pulse length, A is the telescope area, and η is the system efficiency;
- the *geometric factor* describes the range-dependent measurement geometry and is completely determined by the lidar setup; $O(R)$ is the laser-beam receiver-field-of view overlap function, and R^2 describes the quadratic decrease of the signal with distance;
- the *backscatter* term stands for the ability of the atmosphere to scatter light back into the direction from which it comes and it is defined as:

  $$\beta(R,\lambda) = \sum_j N_j(R)\,\frac{d\sigma_{j,sca}}{d\Omega}(\pi,\lambda) \tag{3.2}$$

  where $N_j(R)$ is the concentration of scattering particles of kind j in the volume at distance R illuminated by the laser pulse and $d\sigma_{j,sca}(\pi,\lambda)/d\Omega$ is the particle's differential scattering cross section for the backward direction at wavelength λ. In the atmosphere, the laser light is scattered by air molecules and particulate matter, and then the backscatter can be written as the sum of two components:

  $$\beta(R,\lambda) = \beta_{mol}(R,\lambda) + \beta_{aer}(R,\lambda) \tag{3.3}$$

  where the indices *mol* and *aer* correspond to air molecules and aerosols (particulate matter) respectively;
- the *transmission* term describes how much light gets lost on the way from the lidar to distance R and back, and it can take values from 0 to 1; $\alpha(r,\lambda)$ is the extinction coefficient (the sum of all transmission

losses). It is defined in a similar way as the backscatter coefficient as the product of number concentration and extinction cross section $\sigma_{j,ext}$ for each type of scatterer j:

$$\alpha(R,\lambda) = \sum_j N_j(R)\ \sigma_{j,ext}(\lambda) \tag{3.4}$$

Extinction can occur because of scattering and/or absorption of light by molecules and particles. The extinction coefficient therefore can be written as the sum of four components:

$$\begin{aligned}\alpha(R,\lambda) &= \alpha_{mol}(R,\lambda) + \alpha_{aer}(R,\lambda) = \\ &= \alpha_{mol,sca}(R,\lambda) + \alpha_{mol,abs}(R,\lambda) + \alpha_{aer,sca}(R,\lambda) + \alpha_{aer,abs}(R,\lambda)\end{aligned} \tag{3.5}$$

where the indices *sca* and *abs* stand for scattering and absorption respectively.

In the lidar equation, the system and geometric factors are determined by the lidar setup. The molecular scattering properties, β_{mol} and α_{mol}, can be determined from the best available meteorological data of temperature and pressure or approximated from appropriate Standard Atmosphere so that only the aerosol scattering and absorption properties, β_{aer} and α_{aer}, remain to be determined. In order to solve the equation for the two unknowns it is necessary to assume an a priori knowledge of their relation. The lidar ratio, the extinction-to-backscatter ratio, is defined then for molecules and particles (Ansmann and Müller, 2005). For molecules is given by:

$$S_{mol} = \frac{\alpha_{mol}}{\beta_{mol}} = \frac{8\pi}{3} \tag{3.6}$$

while for particles it is:

$$S_{aer} = \frac{\alpha_{aer}(R,\lambda)}{\beta_{aer}(R,\lambda)} \tag{3.7}$$

The molecular lidar ratio S_{mol} depends on the meteorological conditions, not varying with height. The particle lidar ratio S_{aer}, instead, depends on the size distribution, shape, and chemical composition of the particles, and therefore it is generally a range dependent parameter.

Elastic lidars measure the elastic backscattered signal, and then two physical quantities must be determined from one measured quantity. In this case, the lidar equation (see Eq. 3.1) is solved by using iterative (e.g., Platt, 1973) or analytical methods (e.g., Klett, 1981, 1985). The Stable analytical inversion procedures (Klett, 1985) are widely used and provide robust results in case of optical thick features, whereas suffer when optical thinner features are present, and, what is more, are sensitive to the selection of the lidar ratio. Hence, Di Girolamo et al. (1999) developed an iterative method to obtain the aerosol backscatter coefficient. However, the procedure is based on the selection of a constant lidar ratio.

The aerosol backscatter coefficient, considering the Eq. 3.2, is given by:

$$\beta_{aer}(R,\lambda_0) = R_{aer}(R,\lambda_0)\ N_{mol}(R)\ \sigma_{mol}(\lambda_0) \tag{3.8}$$

where $R_{aer}(R,\lambda_0)$ is the aerosol scattering ratio and is defined as the ratio of aerosol and molecular scattering to molecular scattering, $N_{mol}(R)$ is the molecular number density, and $\sigma_{mol}(\lambda_0)$ is the molecular cross section.

For this procedure, the aerosol scattering ratio can be obtained from the power measured from the system:

$$R_{aer}(R) = \frac{P(R,\lambda)}{P_{mol}(R,\lambda)-1} \tag{3.9}$$

where $P_{mol}(R,\lambda)$ is the molecular contribution to the measured signal $P(R,\lambda)$ and can be written as:

$$P_{mol}(R) = K\ \frac{N_{mol}(R)}{R^2}\ exp[-2(\tau_{mol}(R)+\tau_{aer}(R))] \tag{3.10}$$

where K is a calibration factor and τ the optical depth for molecules and aerosols. The calibration region (reference height) is set in an aerosol free region of the range, where the calibration factor can be retrieved normalizing Eq. 3.1 with $P_{mol}(R,\lambda)$ within that region. The molecular optical depth and number density are typically determined either from radiosondes or models. The iteration starts guessing a $P_{mol}(R)$ value without taking into account the aerosol term in Eq. 3.10. This helps to calculate $R_{aer}(R)$ and $\beta_{aer}(R,\lambda_0)$ from Eqs. 3.9 and 3.8, respectively. Then, we infer the aerosol lidar ratio and we estimate the aerosol optical depth through:

$$\tau_{aer}(R) = \int_0^{R_0} \alpha_{aer}(R')\ dR' \tag{3.11}$$

Following, this estimate is introduced in Eq. 3.10, and a new P_{mol} profile is obtained. The iteration continues until the solution is stabilized. The study of Di Girolamo et al. (1999) showed that after 2-3 iterations, stable $\beta_{aer}(R,\lambda_0)$ values are obtained.

The most critical input parameter in the iterative method is the particle lidar ratio S_{aer}: in case of a wrongly assignment the uncertainty can reach up to 150% (Amodeo, 2010). As mentioned, this quantity depends on the microphysical, chemical, and morphological properties of the particles and is affected by the relative humidity, and therefore it can vary strongly with height. Accordingly, the lidar ratio can be only considered as a first guess, and the true lidar ratio profile remains unknown.

This problem can be overcome using the Raman lidar technique, which provides with an accurate particle extinction coefficient profile (Ansmann et al., 1990). The Raman lidar measures lidar return signals elastically backscattered by air molecules and particles and inelastically Raman backscattered by nitrogen and/or oxygen molecules.

Elastic lidars operate continuously, whereas Raman lidars suffer from the the strong daylight sky background conditions. The strength of Raman signals is a factor of 20 (rotational Raman lines) to 500 (vibration-rotational Raman lines) lower than the one of Rayleigh signals.

The determination of the particle extinction coefficient from molecular backscatter signals is rather straightforward. Lidar ratio assumptions or other critical assumptions are not needed (Ansmann et al., 1992). The advantage of the Raman lidar over the conventional elastic-backscatter lidar is already obvious from the respective lidar equation for the molecular backscatter signal:

$$P(R,\lambda_{Ra}) = \frac{E_0 \eta_{\lambda_{Ra}}}{R^2}\, O(R,\lambda)\, \beta_{Ra}(R,\lambda_0) \times exp\left\{ -\int_0^R \left[\alpha(r,\lambda_0) + \alpha(r,\lambda_{Ra})\right] dr \right\} \tag{3.12}$$

The coefficient β_{Ra} denotes Raman backscattering. The only particle-scattering effect on the signal strength is attenuation, and therefore particle backscattering does not appear in the equation. $\alpha(R,\lambda_0)$ describes the extinction on the way up to the backscatter region, $\alpha(R,\lambda_{Ra})$ the extinction on the way back to the lidar. In the case of a vibration-rotational Raman signal the shift of the wavelength from λ_0 to λ_{Ra} must be considered. If, for example, a Nd:YAG laser wavelength of 532 *nm* is transmitted, the first Stokes vibration-rotation Q branch of nitrogen is centered at $\lambda_{Ra} = 607\ nm$.

The molecular backscatter coefficient is calculated from the molecular number density N_{Ra}, which is the nitrogen or oxygen molecule number density for the Raman case and the air-molecule number density for the Rayleigh case, and the molecular (differential) cross section $d\sigma_{Ra}/d\Omega(\pi, \lambda_0)$ for the scattering process at the laser wavelength λ_0 and the scattering angle π:

$$\beta_{Ra}(R, \lambda_0) = N_{Ra}(R)\ \frac{d\sigma_{Ra}}{d\Omega}(\pi, \lambda_0) \tag{3.13}$$

where $\beta_{Ra}(\lambda_0)$ is equal to β_{mol} in equation 3.3.

Combining equations 3.12 and 3.13 and rearranging the terms, the total extinction coefficient is obtained:

$$\alpha(R, \lambda_0) + \alpha(R, \lambda_{Ra}) = \frac{d}{dR}\ ln \frac{N_{Ra}(R)}{R^2\ P(R, \lambda_{Ra})} + \frac{d}{dR} ln\ O(R, \lambda_{Ra}) \tag{3.14}$$

In the following we concentrate on the optimal measurement range, where $O(R, \lambda_{Ra}) \equiv 1$ and thus the term is omitted. Then, using equation 3.5 we get:

$$\alpha_{aer}(R, \lambda_0) + \alpha_{aer}(R, \lambda_{Ra}) = \frac{d}{dR}\ ln \frac{N_{Ra}(R)}{R^2\ P(R, \lambda_{Ra})} - \alpha_{mol}(R, \lambda_0) - \alpha_{mol}(R, \lambda_{Ra}) \tag{3.15}$$

To obtain the particle extinction coefficient at the transmitted wavelength we have to introduce the Ångström exponent Å(R), which describes the wavelength dependence of the particle extinction coefficient:

$$\frac{\alpha_{aer}(\lambda_0)}{\alpha_{aer}(\lambda_{Ra})} = \left(\frac{\lambda_{Ra}}{\lambda_0}\right)^{\text{Å}(R)} \tag{3.16}$$

Finally we obtain:

$$\alpha_{aer}(R, \lambda_0) = \frac{\frac{d}{dR}\ ln \frac{N_{Ra}(R)}{R^2\ P(R, \lambda_{Ra})} - \alpha_{mol}(R, \lambda_0) - \alpha_{mol}(R, \lambda_{Ra})}{1 + \left(\frac{\lambda_0}{\lambda_{Ra}}\right)^{\text{Å}(R)}} \tag{3.17}$$

In contrast to the iterative method, no critical assumption is needed; an overestimation of the Å value by 0.5 leads to relative errors of the order of 5% (Ansmann and Müller, 2005).

However, the Raman lidars used in this work are limited by the lighting condition. Considering that the Raman backscattered light is several orders of magnitude smaller than the elastic, it is not possible to measure it accurately during day-time, when the atmospheric background noise is very high. Therefore, the aerosol extinction profiles can only be retrieved during night-time and the iterative method must be applied during day-time in order to retrieve the aerosol backscatter profiles.

3.1.2 Linear particle depolarization ratio

The linear particle depolarization ratio (δ_p) is the ratio of the perpendicular to the parallel component of the particle backscatter coefficient at a certain wavelength:

$$\delta_{aer}(R,\lambda) = \frac{\beta_{\perp}(R,\lambda)}{\beta_{\parallel}(R,\lambda)} \tag{3.18}$$

This variable has been used widely during the last years to gain important information on the shape of measured aerosols (Freudenthaler et al., 2009).

As measured, the depolarization is referred to the sampled volume, but once the aerosol backscatter coefficient is known, the linear particle depolarization ratio (δ_p) can be calculated.

We consider only the case that the backscatter light is measured at two perpendicular polarization axis, parallel and perpendicular to the polarization plane (the one that is defined by the direction of propagation and the electric field vector) of the laser beam. The collected light passes through a Polarizing Beamsplitter Cube (PBC) and is then directed to the detectors. For such a system, the measured power is given by:

$$P_{\perp} = \frac{\eta_{\perp}}{R^2} \left(\beta_{aer}^{\perp} + \beta_{mol}^{\perp}\right) T^2 \tag{3.19}$$

$$P_{\parallel} = \frac{\eta_{\parallel}}{R^2} \left(\beta^{\parallel}_{aer} + \beta^{\parallel}_{mol}\right) T^2 \tag{3.20}$$

where η is the efficiency of the receiving system up to the PBC, T is the atmospheric transmission term, and $\beta^{\perp}$ and $\beta^{\parallel}$ are the cross and parallel polarized components of the backscatter coefficient and their sum is the total backscattering coefficient:

$$\beta = \beta^{\perp} + \beta^{\parallel} \tag{3.21}$$

The linear volume depolarization ratio is defined as:

$$\delta_v = \frac{\beta^{\perp}_{aer} + \beta^{\perp}_{mol}}{\beta^{\parallel}_{aer} + \beta^{\parallel}_{mol}} \tag{3.22}$$

The signals P_R and P_T that are recorded by the detectors are given by:

$$P_R(\phi) = \left(P_{\perp}(\phi)\, R_{\perp} + P_{\parallel}(\phi)\, R_{\parallel}\right) V_R \tag{3.23}$$

$$P_T(\phi) = \left(P_{\perp}(\phi)\, R_{\perp} + P_{\parallel}(\phi)\, R_{\parallel}\right) V_T \tag{3.24}$$

where $P_{\perp}$ and $P_{\parallel}$ are the power that arrives perpendicular and parallel to the incident plane of the PBC, ϕ is the angle between the plane of polarization of the laser and the incident plane of the PBC, R and T are the reflection and transmission efficiency, and V_T and V_R are the efficiencies of the two measuring channels including the amplification by the detector. Then, the relative amplification factor V^* is defined as:

$$V^* = \frac{V_R}{V_T} \tag{3.25}$$

and the ratio of the measured signals is:

$$\delta^* = \frac{P_R(\phi)}{P_T(\phi)} \tag{3.26}$$

For a perfect PBC and at $\phi = 0$, these quantities are related as:

$$\delta_v = V^*\ \delta^* \tag{3.27}$$

A robust method for calculating the relative amplification factor V^* is the so-called ±45 calibration (Freudenthaler et al., 2009), in which two depolarization measurements are performed at +45° and -45° in respect to the normal measuring position. Then, the relative amplification factor can be calculated as:

$$V^* = \frac{T_{\parallel} + T_{\parallel}}{R_{\parallel} + R_{\perp}} \sqrt{\delta^*(+45^\circ)\ \delta^*(-45^\circ)} \tag{3.28}$$

The advantage of this method is that the results are independent of the atmospheric condition and relatively insensitive to inaccurate determination of the ±45 angles in respect to the polarization plane of the laser. When V^* is known, the linear volume depolarization ratio can be calculated using equation 3.27.

Then, if the aerosol backscatter profile is known, the linear particle depolarization ratio δ_p can be calculated as:

$$\delta_p = \frac{\left(1+\delta_{mol}\right)\ \delta_v\ R - \left(1+\delta_v\right)\ \delta_{mol}}{\left(1+\delta_{mol}\right)\ R - \left(1+\delta_v\right)} \tag{3.29}$$

where R is the backscatter ratio:

$$R = \frac{\beta_{mol} + \beta_{aer}}{\beta_{mol}} \tag{3.30}$$

3.2 Cloud radar

A millimetre-wavelength cloud radar MIRA36 produced by METEK is operating at CIAO since March 2009, and can be seen in *Fig. 3.4*. It is a mono static magnetron-based pulsed Ka-Band Doppler radar operating at 8.6 *mm* wavelength (35 *GHz*); it has a sensitivity of -55 *dBZ* at 1 *km* and -40.3 *dBZ* at 5 *km* (Madonna et al., 2011). According to its current configuration, the time and range resolution are 10 *seconds* and 30 *meters* respectively. Pulses of electromagnetic energy linearly polarized are transmitted, and co- and cross polarized signals are received simultaneously. The backscattered signal can be considered as a complex signal, sampled with the Pulse Repetition Frequency (PRF). By the complex notation, the signal can be written as (Bauer-Pfundstein, 2009):

$$y(kT) = I(kT) + iQ(kT), \quad k = 0, 1, ..., N_{FFT} - 1 \tag{3.31}$$

where $y(kT)$ is called "I-Q-signal", T is the pulse repetition period and N_{FFT} is the length of the Fast Fourier Transform (FFT) used to obtain the Doppler spectra from the I-Q-signal. The I and Q signal is derived taking the real and imaginary part of the received complex voltage.

Figure 3.4: *MIRA36 Ka-band Doppler radar operating at CIAO.*

The amplitude of the backscattered pulses describes the reflectivity of meteorological targets, and the phase change of the I-Q-signal from pulse to pulse contains the information about the motion of the targets.

From equation 3.31, the following variables can be calculated:

- Signal-to-Noise Ratio (SNR): the 0^{th} moment divided by the receiver noise level:

  $$SNR = 10\ log\left(\frac{\sum_{n=0}^{N_{FFT}-1} S_n}{P_{Rec.noise}}\right) \tag{3.32}$$

  where S_n is the power spectrum of the received signal and $P_{Rec.noise}$ is the receiver noise. The SNR is usually expressed in decibels (dB), where $A\ [dB] = 10\ log_{10}(A)$.

- Doppler velocity (VEL or v): the 1^{st} moment, it is the mean value of the Doppler spectra and therefore indicates the mean velocity of the targets present in the sampled radar volume:

$$v = -\frac{\lambda}{2}\frac{1}{P_0}\sum_{n=0}^{N_{FFT}-1} f_n S_n \tag{3.33}$$

where λ is the wavelength, P_0 is the power of the scattered signal, and f_n are the frequencies assigned to the frequency bins of the discrete spectra obtained by the FFT's. The Doppler velocity is usually expressed in $m\ s^{-1}$.

- Peak Width (RMS or W): the 2^{nd} moment, it corresponds to the variance of the Doppler spectra, and thus it gives an indication of the range of the detected velocities in the sampled volume:

  $$W^2 = \left(\frac{\lambda}{2}\right)^2 \frac{1}{P_0}\sum_{n=0}^{N_{FFT}-1} f_n^2 S_n - V^2 \tag{3.34}$$

  It is usually expressed in $m\ s^{-1}$.

The radar reflectivity (η) is the 6^{th} moment, and depends on the number and size of the particles. However, in meteorology the most commonly used parameter is the radar equivalent reflectivity factor Z_e. In the following, the radar equation is presented together with the definition of the radar equivalent reflectivity factor.

The radar equation for a point target is:

$$P_R = \frac{P_T\ G_0^2\ |f_n(\theta)|^4\ \lambda^2}{(4\pi)^3\ L}\frac{\sigma}{R^4} \tag{3.35}$$

where P_R is the received power, P_T is the transmitted power, G_0 is the antenna gain, $|f_n(\theta)|^4$ is the normalized antenna pattern, λ is the radar wavelength, L is the power loss introduced by the components between the antenna and the Low Noise Amplifier (LNA), R is the distance to the target, and σ is the radar backscattering cross section of the target.

The radar equation for the mean power for volume filling distributed targets is:

$$\overline{P}_R = \frac{1}{V}\int_V P_R\, dV = \frac{P_T\ G_0^2\ \lambda^2}{(4\pi)^3\ L}\frac{1}{V}\int_V |f_n(\theta)|^4\ \frac{1}{R^4}\ \sum_i \sigma dV \tag{3.36}$$

where V is the radar resolution volume. The radar reflectivity η is used instead of the backscattering cross section:

$$\eta = \frac{1}{V}\sum_i \sigma_i \tag{3.37}$$

Then, assuming that the radar reflectivity is uniform within the radar resolution volume and substituting $dV = R^2\ dR\ d\Omega$, we get:

$$\overline{P}_R = \frac{P_T\ G_0^2\ \lambda^2}{(4\pi)^3\ L}\ \eta \int_R^{R+c\tau/2} \frac{dR}{R^2} \int_\Omega |f_n(\theta)|^4 d\Omega = \frac{P_T\ G_0^2\ \lambda^2}{(4\pi)^3\ L}\ \eta \frac{c\tau}{2R^2}\frac{\pi\theta_0^2}{8\ ln\ 2} \tag{3.38}$$

Introducing the equivalent radar resolution volume at the distance R, $V = \frac{c\ \tau}{2}\frac{\pi\ \theta_0^2}{8\ ln\ 2}\ R^2$, the radar equation for a distributed target is:

$$\overline{P}_R = \frac{P_T\ G_0^2\ \lambda^2\ c\ \tau\ \theta_0^2}{1024\ \pi^2\ ln\ 2\ L}\frac{\eta}{R^2} \tag{3.39}$$

The equivalence between the radar reflectivity η and the radar equivalent reflectivity factor Z_e is:

$$Z_e = \frac{\lambda^2}{\pi\ |K|^2}\ \eta \tag{3.40}$$

where $|K|^2$ is the dielectric constant of the observed target (i.e. $|K_{water}|^2 = 0.93$).

Assuming that the Rayleigh approximation is valid and all the targets are spherical, $Z_e = Z$:

$$Z = \int_0^\infty N(D)\ D^6\ dD \tag{3.41}$$

where N corresponds to the number of particles and D to their diameter. It is usually expressed in dBZ, decibel relative to Z, being Z measured in $mm^6\ m^{-3}$.

Finally, using Z_e the radar equation can be written as:

$$\overline{P}_R = \frac{P_T\ G_0^2\ \lambda^2\ c\ \tau\ \theta_0^2}{1024\ \pi^2\ ln\ 2\ L}\frac{\pi^5\ |K|^2}{\lambda^4}\frac{Z_e}{R^2} \tag{3.42}$$

For simplicity, in this study the radar equivalent reflectivity factor Z_e will be denominated reflectivity Z.

Regarding the radar polarization measurements, the Linear Depolarization Ratio (LDR) is calculated as the ratio between the power received in the cross-polarized channel and in the co-polarized channel:

$$LDR = \frac{P_{\perp}}{P_{\parallel}} \tag{3.43}$$

It gives an indication of the asphericity of the targets and it is usually expressed in dB.

3.3 Ancillary measurements

The use of additional meteorological information, such as temperature, wind profiles and precipitation data, has been very important in this study. These were obtained from ancillary instrumentation or numerical models, which are described in the following.

3.3.1 Ground-based remote sensing

Measurements from three ground-based remote sensing instruments, a MicroWave Radiometer (MWR), a ceilometer, and a sun photometer, are used. A brief description of these instruments is given in the following; more information about the instruments can be found in Madonna et al. (2011).

3.3.1.1 Microwave radiometer

The microwave radiometer (model MP3014, produced by Radiometrics) measures the sky Brightness Temperature (BT) at 12 frequencies, 5 in the Ka band around 22 GHz and 7 in the V band around 60 GHz. The inversion of the BT, based on a neural network algorithm (Ware and Solheim, 2000), provides temperature and humidity profiles up to 10 km as well as an estimation of the Ice Water Content (IWC), Liquid Water Content (LWC), Liquid Water Path (LWP) and Integrated Precipitable Water Vapour (IPWV).

3.3.1.2 Ceilometer

The CT25K VAISALA ceilometer measures continuously the cloud-base height and the signal backscattered by atmospheric particles at 905 *nm* up to 7.5 *km*. The ceilometer is basically a Rayleigh lidar system that employs a pulsed In-Ga-As diode laser emitting at 905 *nm* wavelength using a high repetition rate (1.6 μJ of energy per pulse at 6.67 *kHz*) and detects the elastic backscattered radiation. The CT25K ceilometer is able to detect three cloud layers simultaneously to identify precipitation or other obstructions to vision. Besides cloud layers, it also provides the profile of uncalibrated backscattering coefficient. It has a vertical resolution of 30 *m* and a temporal resolution of 15 *s*.

3.3.1.3 Sun photometer

The CIMEL CE-318 sun photometer is a multi-channel automatic sun-and-sky scanning radiometer that measures the direct solar irradiance and sky radiance at the Earth's surface.

The instrument delivers a multitude of aerosol columnar properties. The main product is the Aerosol Optical Depth (AOD) at 340, 380, 440, 500, 675, 870, 1020, and 1640 *nm*, that can be used to compute columnar water vapour and to estimate the aerosol refractive index and size distribution. The CIMEL CE-318 sun photometer at CIAO is operational within AErosol RObotic NETwork (AERONET), the reference network of sun photometer ground-based aerosol measurements.

The photometers of the network follow a fixed measurement schedule. Direct sun measurements are performed every 15 *min*. Each measurement takes around 10 *s*. A triplet of such measurements is performed each time with 30 *s* distance; these three measurement can be used to screen clouds that have much greater temporal variability than aerosol. The 15 *min* intervals are also used for cloud screening in longer time frames. There are two different types of sky measurements performed: almucantar and principle plane measurements. The almucantar measurements are performed at the elevation angle of the sun for specific azimuth angles relative to the sun. Only four wavelengths are used in this case (440, 670, 870,1020 *nm*) and the measurements are performed in sequence for each of them. A set of almucantar measurements is performed every hour between 9:00 and 15:00 local solar time and take around 4 *min* each. The principle plane measurements use the same channel as the almucantar ones but measure along the principle planes of the sun. Each such measurement takes around 3 *min*. The sky radiance measurements are used in the AERONET processing algorithms to perform a microphysical inversion that gives detailed information about the Particle Size Distribution (PSD) and the complex index of refraction. In the current version of the inversion algorithm, the particles are assumed to be a mixture of spheres and spheroids and a cloud mask is applied to remove cloud contamination.

The cloud mode capability in AERONET increases the cloud optical depth observations (one of the most poorly observed climate variables) in both number and accuracy. When clouds block the sun, the sun photometer is set to cloud mode operations, in which the AERONET radiometers take 10 zenith radiance measurements in up to 6 narrow spectral bands with a sampling resolution of 9 *s*. This set of measurements is taken every 15 *min*.

The zenith radiances at wavelengths of 440 and 870 *nm* together with the surface albedo are used to retrieve the Cloud Optical Depth (COD). At these two wavelengths, the COD is almost identical, but vegetated surfaces reflect differently (the surface is typically 5 - 8 times brighter at 870 *nm* than at 440 *nm*). The surface albedo is taken from Moderate Resolution Imaging Spectroradiometer (MODIS) when available, and from a climatological database derived from 5 *years* of MODIS observations otherwise. The COD is averaged over 1.5 *min*, and it is derived from the cluster of 10 instantaneous retrievals from individual zenith radiance measurements (Chiu et al., 2010).

3.3.2 Space-borne remote sensing

3.3.2.1 SEVIRI

For the cross-check of some particular aerosol observations at the site, images acquired by the Spinning Enhanced Visible and Infrared Imager (SEVIRI) are used. The SEVIRI sensor is the optical imaging radiometer on

Table 3.1: *General characteristics and applications of the* SEVIRI *channels.*

Channel No	Spectral band [μm]	Characteristics [μm] λ_{cen}	λ_{min}	λ_{max}	Main observational application
1	VIS0.6	0.635	0.56	0.71	Surface, clouds, wind fields
2	VIS0.8	0.81	0.74	0.88	Surface, clouds, wind fields
3	NIR1.6	1.64	1.50	1.78	Surface, cloud phase
4	IR3.9	3.90	3.48	4.36	Surface, clouds, wind fields
5	WV6.2	6.25	5.35	7.15	Water vapour, high level clouds, atmospheric instability
6	WV7.3	7.35	6.85	7.85	Water vapour, atmospheric instability
7	IR8.7	8.70	8.30	9.1	Surface, clouds, atmospheric instability
8	IR9.7	9.66	9.38	9.94	Ozone
9	IR10.8	10.80	9.80	11.80	Surface, clouds, wind fields, atmospheric instability
10	IR12.0	12.00	11.00	13.00	Surface, clouds, atmospheric instability
11	IR13.4	13.40	12.40	14.40	Cirrus cloud height, atmospheric instability
12	HRV	Broadband (about 0.4 - 1.1)			Surface, clouds

board METEOSAT Second Generation (MSG) satellites, which are the second generation of geostationary, meteorological satellites developed by the European Space Agency (ESA) in close co-operation with the European Organisation for the Exploitation of Meteorological Satellites (EUMETSAT). As reported in *Table 3.1*, the sensor has 12 different spectral channels: 3 in the visible, 1 in the near infrared and 8 in the infrared region of the spectrum. Altogether, they provide unique capabilities in cloud imaging and tracking, fog detection, measurement of the earth surface and cloud top temperatures, tracking ozone patterns, as well as many other improved performances. Its temporal resolution is of 15 *min*, while its spatial resolution is of 3 *km* for all the channels except for the High Resolution Visible (HRV) channel, which is 1 *km*.

3.3.2.2 MODIS

Some products based on the information acquired by MODIS can be very useful to identify aerosol types and sources in order to assist the aerosol ground-based observations.

MODIS is a sensor on board two NASA (National Aeronautics and Space Administration) polar orbiting satellites: Terra and Aqua. It has 36 channels in the visible, near-infrared and infrared bands that are used to observe the land and oceans as well as the atmospheric constituents (i.e. clouds, aerosols, ozone and water vapour). The cross track is 2330 *km*, while the spatial resolution depends on the channel, ranging from 250 to 1000 *m*. Terra and Aqua orbit around the Earth at 705 *km*, imaging the Earth's entire surface in less than two days.

Among the several products elaborated from the MODIS imagery, the MODIS active fire product is of our interest. It detects fires in 1 *km* pixels that are burning at the time of overpass under relatively cloud-free conditions using a contextual algorithm, where thresholds are first applied to the observed middle–infrared and thermal infrared brightness temperature and then false detections are rejected by examining the brightness temperature relative to neighbouring pixels (Giglio et al., 2003).

3.3.3 In-situ measurements

Three types of in-situ instruments are used: an automatic weather station, radiosoundings and a rain gauges network.

The MILOS520 Automatic Weather Station manufactured by VAISALA routinely monitors pressure, temperature, humidity and wind at the surface level (Madonna et al., 2011).

Weekly radiosoundings (models AS13, MW21 and PP15, manufactured by VAISALA) provide in-situ profile observations of temperature, pressure, humidity and winds (Madonna et al., 2011).

The rain gauges network run by the Basilicata Region Civil Protection measures the accumulated precipitation in the region where the study has been carried out with an accuracy of 0.2 *mm*. *Figure 3.5* shows all the rain gauges that have been considered. There are several hydrological basins in the Basilicata region, and for this reason the pluviometers have been divided in three groups according to the regions used by Civil Protection to emit hydrogeological risk regional warnings (*www.protezionecivilebasilicata.it*):

- *Group A* comprises the hydrological basins in the north and north-west of the region, corresponding to the rivers Ofanto and Sele.
- *Group B* contains the eastern area of the region, in the Basento, Bradano and Cavone rivers domain.
- *Group C* embraces the southern part of the region, including the Agri, Noce and Sinni hydrological basins.

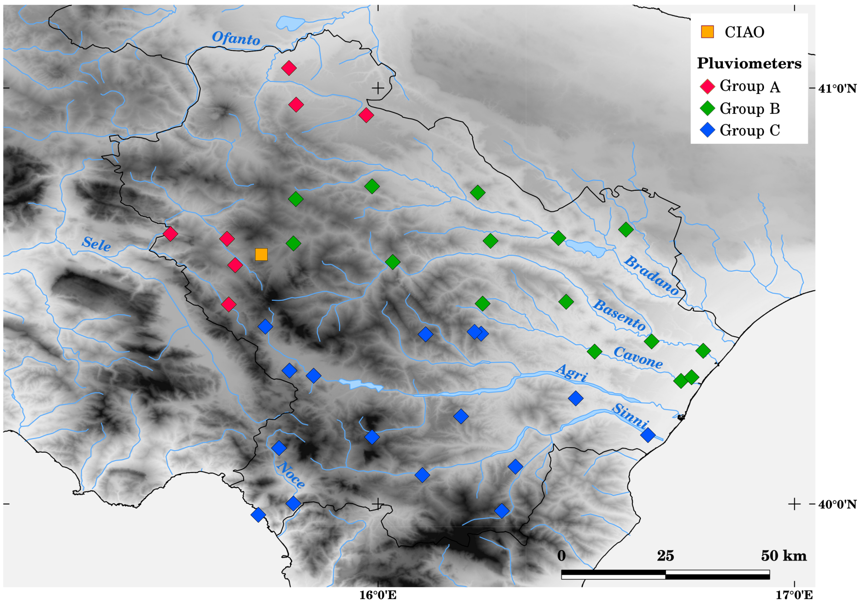

Figure 3.5: *Rain gauges network of the Basilicata region, run by the Civil Protection in the Basilicata region. The rain gauges are divided into the three groups, indicated with A, B and C.*

3.3.4 Models

Two different types of models are used in this study: the European Center for Medium-range Weather Forecasts (ECMWF) model is used to obtain the wind profile and pressure vertical velocity forecast, while the FLEXible PARTicle dispersion model (FLEXPART) is used to identify the possible sources of the aerosol layers observed at the site with the cloud radar and the lidar.

The ECMWF Integrated Forecast System Model has an horizontal resolution of 39 *km* and 60 vertical levels. The output used has a forecast range between 12 and 35 *hours* and a temporal resolution of 1 *h*. Some of its data outputs, such as the forecasted wind speed and direction are used in this study.

FLEXPART is a Langrangian particle dispersion model that computes trajectories of a large number of so-called particles (not necessarily representing real particles, but infinitesimally small air parcels) to describe the transport and diffusion of tracers in the atmosphere (Stohl et al., 2005). FLEXPART simulations are based on meteorological fields and simulate the long-range and mesoscale transport, diffusion, dry and wet deposition, and radioactive decay of tracers released from point, line, area or volume sources. It can be used backward in time to identify the possible regions that could contribute to the measured aerosol load (Seibert and Frank, 2004).

In this work, the FLEXPART model was driven by data of the National Center for Environmental Prediction (NCEP) Climate Forecast System (CFS) (Saha et al., 2010) with time resolution of 3 *hours* and horizontal resolution of 1 *degree*. The simulations were performed considering a 7-day-long period and the output was stored at a grid with horizontal resolution of 0.2° × 0.2° at 12 vertical levels with 1 *km* distance. The FLEXPART outputs used for this study are two: the total column sensitivity and the ground-level sensitivity. The total column sensitivity indicates how much time the air parcels that reached the site spend in the atmospheric column of a certain location. The ground-level sensitivity represents the time the air parcels stayed in the lowest 1 *km* of the atmospheric column of a certain location.

4

Cloud radar aerosol observations

In this chapter, the development of a novel technique to identify and characterize giant aerosols with the cloud radar is described. The results of its application to approximately 6 *years* of measurements are shown. Then, an approach for near real-time aerosols automatic identification is presented. Finally, the correlation of giant aerosol with other atmospheric variables like Aerosol Optical Depth (AOD) and Cloud Optical Depth (COD) is studied and discussed, as well as the effect of the giant particles on the development of warm rain processes.

4.1 Observation methodology

The microwave radiation emitted by the radar probes the atmospheric vertical structure, and receives echoes caused by different kinds of scatterers (hereinafter targets). The target discrimination is essential for interpreting the cloud radar observations, and in many cases this operation can be accomplished only using the different Doppler velocities. In the cloud radar MIRA36 algorithms, following the noise (clutter) removal, the targets are classified into clouds, rain and plankton; the latter is a radar term used to describe non-hydrometeorological targets (i.e. insects).

Ka and W-band cloud radars (35 and 94 *GHz* respectively) detect almost exclusively insect targets on warm cloudless days (Clothiaux et al., 2000; Khandwalla et al., 2002). Indeed, radar has been applied to the study of insects for more than 40 *years*. Since wind-borne insect migration occurs on a colossal scale, far exceeding (at least in numerical terms) the migratory flux of birds (Chapman et al., 2011) and giant and ultragiant volcanic aerosols can be detected by Ka-band radars (Marzano et al., 2006a,b; Madonna et al., 2010, 2013), we can assume that the non-hydrometeorological (plankton) echoes consist of insect and aerosol returns only. Therefore, a strategy has been developed, based on insects characteristics and behaviour to detect and subtract them from the radar signals, keeping the aerosol returns only.

The first of the insects characteristics that has to be taken into account is their spatial evolution throughout the day. The depth of the insect layer follows the diurnal variation of the Atmospheric Boundary Layer (ABL) with a minimum during night-time, sharply increases in the morning, and reaches a maximum in the afternoon. According to this daily evolution, represented in *Figure 4.1*, crepuscular, diurnal and nocturnal insects can be identified with almost no overlap between them. Crepuscular species take off during the morning twilight period, with small numbers and a generally short-lived flight, although occasionally continue for some time and daytime layers are reported (Chapman et al., 2011). Day-flying migrants take off from mid-morning onward, as atmospheric convection develops, and generally descend in the late afternoon; occasionally, small numbers of day-flying species continue their migration into the night (Chapman et al., 2011). Nocturnal species typically have a mass take off at dusk and fly throughout the night following the stratification of the nocturnal ABL (Chapman et al., 2004; Reynolds et al., 2005, 2008; Wood et al., 2006, 2009b). Therefore, they tend to concentrate into layers of shallow depth but broad horizontal extent (Drake, 1984; Drake and Farrow, 1988; Gatehouse, 1997; Reynolds et al., 2009).

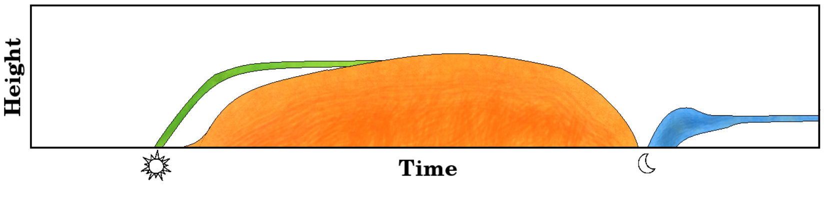

Figure 4.1: *Insect daily schematic evolution, in three distinguished groups: crepuscular (green), diurnal (orange) and nocturnal (blue). The height reached by the insects depends on the geographical location and meteorological conditions.*

Typically, insects size range is of the order of *millimeters*, whereas aerosols size range after atmospheric transport can reach up to tenths of *microns*. Considering that the radar reflectivity is proportional to the sixth power of the diameter of the scatterers, aerosols are only detectable in range gates free of insects. Therefore, only the lofted layers relative to the insect flight identified areas are searched for and further processed. *Figure 4.2* depicts the approach that has been developed for this purpose. First, according to the cloud radar original classification (Bauer-Pfundstein and Görsdorf, 2007), the plankton (non-hydrometeorological) layers are looked for. Due to the speckled nature of the cloud radar images, it was established that the lofted layers should have 600 pixels at least, which corresponds to a 300 *m* thick layer that lasts for 10 *min*. Second, the misclassification of the outer cloud and rain pixels into the plankton category that is frequently done by the original cloud radar classification algorithm needs to be overcome. With this purpose, the cloud and rain areas are expanded 2 *min* in time and 120 *m* in range to create a cloud mask. This mask includes the clouds and rain regions, including their outer originally misclassified pixels. Third, the cloud base height detected by the ceilometer is also included into the mask in order to avoid inserting misclassified clouds into the process. Finally, after applying the cloud mask, the remaining layers are classified into lofted or not lofted depending on their minimum height.

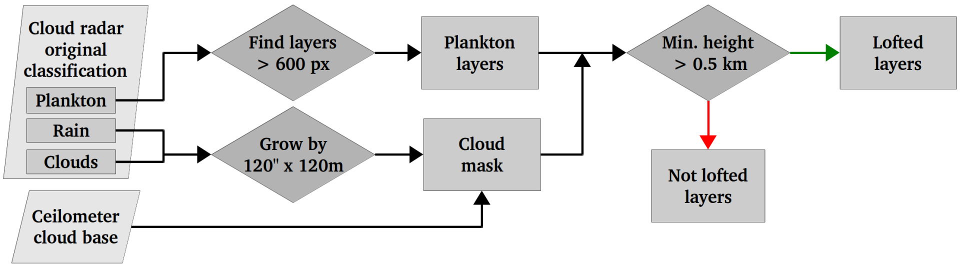

Figure 4.2: *Methodology adopted for the identification of non-hydrometeorological targets lofted layers. The green arrow indicates the condition is fulfilled, the red one that it is not.*

After the identification of the plankton lofted layers, a series of tests based on the insect behaviour in the atmosphere are carried out to distinguish between the aerosol and insect layers. The different criteria are based on entomology studies and consider atmospheric variables such as the temperature and the wind. The key features of insects layers are explained next. Two aspects of the insects relation with temperature were considered: (a) the ceiling (maximum height) of the insect layer can be approximated by the $10°C$ isotherm in most cases, even though there is a tendency of insects to tolerate lower temperatures after prolonged periods with temperatures lower than average (Luke et al., 2007); and (b) the insect layers during night-time are frequently located near the inversion top height (Reynolds et al., 2005). Regarding the insects behaviour with respect to the wind, it was found that they do not fly at a wind speed on the Beaufort wind force scale[1] higher than 5 (Møller, 2013), which corresponds to a mean wind speed of 10 $m\ s^{-1}$; and that the aerosol layers tend to follow the isotachs of horizontal wind speed, while insects have a more random behaviour. Finally, concerning the relation of the insects with the convection, the ABL and the height, it is known that (a) insects tend to be concentrated in plumes of rising air (Reid et al., 1979); that (b) there are usually many more insects within the Convective Boundary Layer (CBL) than above it (Wood et al., 2009a); and that (c) migrating insects typically fly at high altitudes, sometimes as high as 2 or 3 *km* above the ground (Gatehouse, 1997).

Figure 4.3 illustrates the developed methodology based on entomology criteria. In order to perform the following screening steps, ancillary measurements are required. Radiosoundings temperature and wind profiles are used, if available, within a temporal difference of 2 *h*. In any other case, profiles provided by MWR and ECMWF model are used for temperature and wind respectively.

In the first step, the layers that have more than 60% upward Doppler velocities are classified as insects. If not, then it is a possible aerosol layer and goes through the second screening step. In this step, which is only applied during night, the layer location relative to the temperature inversion height is used as the screening metric. If more than 10% of the layer is located within 500 *m* higher or lower of the temperature inversion height, it is classified as an insect layer. If not, it goes ahead in the classification procedure. In the third screening step, four tests are applied:

1. is the temperature of more than 90% of the points below $0°C$?
2. are more than 90% of the layer pixels located above 3 *km*?

---

[1] The Beaufort wind force scale is an empirical measure that relates wind speed to observed conditions at sea or on land.

3. is the corresponding horizontal wind speed of at least 90% of the layer pixels over 10 $m\ s^{-1}$?

4. is the difference of angle between the layer and the isotachs orientation lower than 30°?

The layer that meets at least one of these conditions is classified as aerosol. If not, it falls into the insect category.

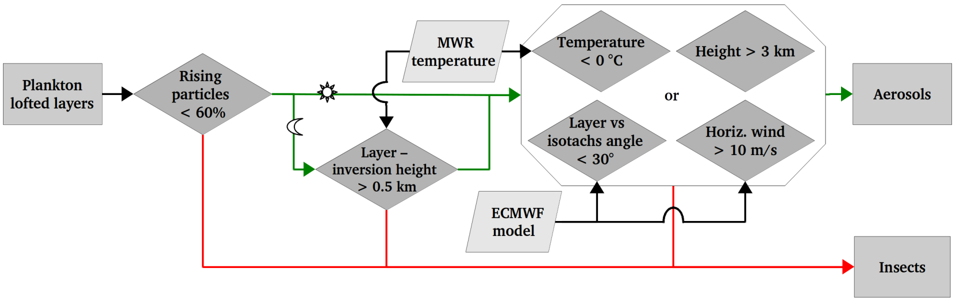

Figure 4.3: *Methodology used for the creation of the aerosol-insect database, applying tests based on entomology studies. Green arrows indicate the condition is fulfilled, and red arrows that it is not.*

Some other criteria found in the entomology literature, such as a limitation of the insects to fly when the daily mean surface temperature is below 10°C (Khandwalla et al., 2002), have been also tested but finally not applied, since they did not provide an additional value.

Finally, since radar measurements alone cannot provide unique information on whether giant aerosols are embedded in the insect layers due to their highly differing sizes, it is necessary to check independent measurements to further scrutinise the results obtained from the cloud radar. For this reason, the insect layers following the methodology of *Fig. 4.3* are submitted to an additional screening criterion. The size distribution retrievals from the AERONET sun photometer during the insect layer are averaged. Then, if the effective radius of the coarse mode is bigger than 2.5 μm, in accordance to the giant aerosols definition, it is considered that the layer consists of insects with embedded giant aerosols (*Fig. 4.4*).

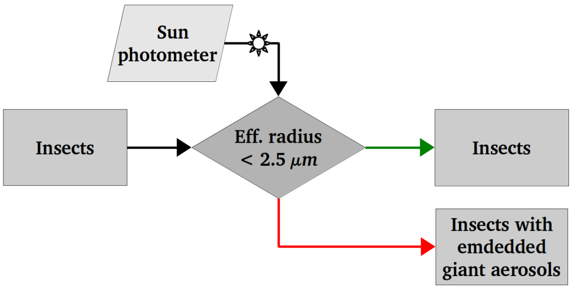

Figure 4.4: *Additional screening criteria applied to the insect cases in order to discard the presence of embedded giant aerosols within the insect layers. Green arrows indicate the condition is fulfilled, and red arrows that it is not.*

This criterion can only be applied during day-time, when the sun photometer is operating. During night-time, the atmospheric conditions are generally more stable and, in addition, the cases occurring in this period are checked for the temperature inversion.

4.2 Dataset

The described method was applied to all the cloud radar observations within the period of March 2009 - June 2015, resulting in the identification of 328 aerosol layers, 684 insect layers and 18 insect layers with embedded giant aerosols. *Table 4.1* shows the day/night distribution of the identified layers.

Table 4.1: *Aerosols, insects and insects with embedded giant aerosol lofted layers dataset (March 2009 - June 2015). Between parentheses is the percentage of layers of the total. Note that some layers have a long duration and are both day and night-time.*

Layers	Aerosol	Insect	Insect with embedded giant aerosol
Night-time	155 (26.9%)	421 (73.1%)	0 (0%)
Day-time	175 (37.8%)	270 (58.3%)	18 (3.9%)
Total	328 (31.8%)	684 (66.4%)	18 (1.7%)

The number of aerosol layers during day and night is very similar, while the number of insect layers during night is much higher than during day. This might be due to one of the steps in the screening procedure, in which the temperature inversion height is compared to the height of the aerosol/insect layer. Sun photometer data is used in order to detect embedded giant aerosol layers within the insect layers, as explained in *Section 4.1*. Information from this instrument was available for 139 of the 288 total insect cases (for the 48.3%), and it was found that the 12.9% of the insect layers to which this criterion could be applied contained giant aerosols. Henceforth, only the aerosol and insect layers without embedded giant aerosols will be considered in order to compare the two targets.

The frequency distribution of the radar moments and the LDR for aerosols and insects are shown in *Fig. 4.5*. The reflectivity distribution (*Fig. 4.5a*) is very similar for both targets. Even though, some small differences are observed: low reflectivity values are observed more frequently for insects, while aerosols reach higher reflectivity values. In the Doppler velocity distribution (*Fig. 4.5b*), it must be taken into account that one of the screening criteria, the one that considers the insects preference for updrafts, affects this variable. It can be noted that aerosols tend to have downwards velocities, as an effect of gravitational settling. A few aerosol layers fall at high vertical velocities (over 2 $m\ s^{-1}$), while some have slightly upwards velocities, meaning they are being carried by air fluxes. For insects, the most common vertical velocities are around 0 $m\ s^{-1}$. The peak width distribution (*Fig. 4.5c*), which gives an idea of the turbulence, shows a similar distribution for aerosols and insects. The most remarkable difference in this plot is that insects occur with lower peak width (a 15% more in the first bin). The LDR distribution (*Fig. 4.5d*) is bimodal for the aerosols and unimodal for the insects, being the low values more common for the first ones. This indicates that the difference between the SNR between the co- and the cross-channel is, in general, higher for aerosols. This effect might be due to the effective irregularities of the two targets.

In *Figure 4.6* the monthly and daily distributions of the layers are shown. Regarding the occurrence of the aerosol layers throughout the year (*Fig. 4.6a*), the maximum number of layers observed occurs during summer (July and August), and a relative maximum is observed in April. These features, together with an observation of a minimum during winter are in accordance to climatological studies of the site (Mona et al., 2006, 2014). Most likely, the peak during spring is caused by pollen and dust and the one during summer by dust. The distribution of the layers during the day (*Fig. 4.6b*) does not present significant differences between the aerosols and insects frequency along the day.

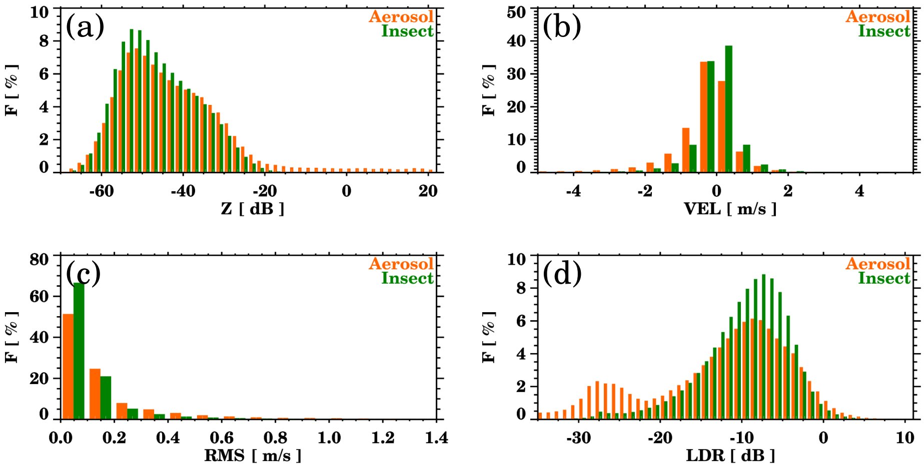

Figure 4.5: *Frequency distribution of (a) reflectivity, (b) Doppler velocity, (c) peak width, and (d)* LDR *for all the aerosols and insect cases.*

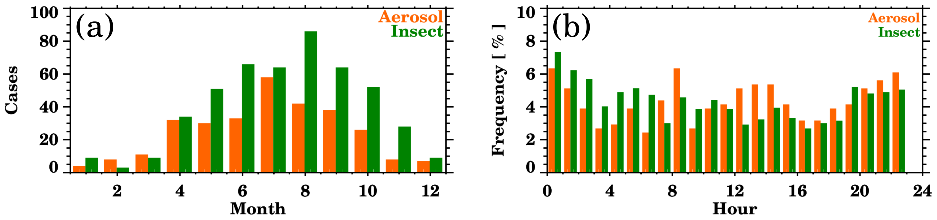

Figure 4.6: *(a) Number of aerosol and insect cases per month; (b) daily frequency distribution of layers.*

Concerning the vertical distribution of the layers (*Fig. 4.7a*), aerosol layers are usually located at higher altitudes compared to the insect layers; and any information can be extracted from the layer thickness (*Fig. 4.7b*). *Fig. 4.7c* shows the distribution of the percentage of rising particles of the layers: most of the times, the aerosol layers have a vertical velocity close to zero (40 to 60% of rising particles), and in some cases most of the particles are falling. This characteristic helps to distinguish these layers from the insect ones, as insects tend to follow the upward motion of the air parcels. The horizontal wind speed at the layer heights is represented in *Fig. 4.7d*: most insects fly when the wind speed is between 2 and 5 $m\ s^{-1}$, while aerosol layers are observed in a wider range of velocities.

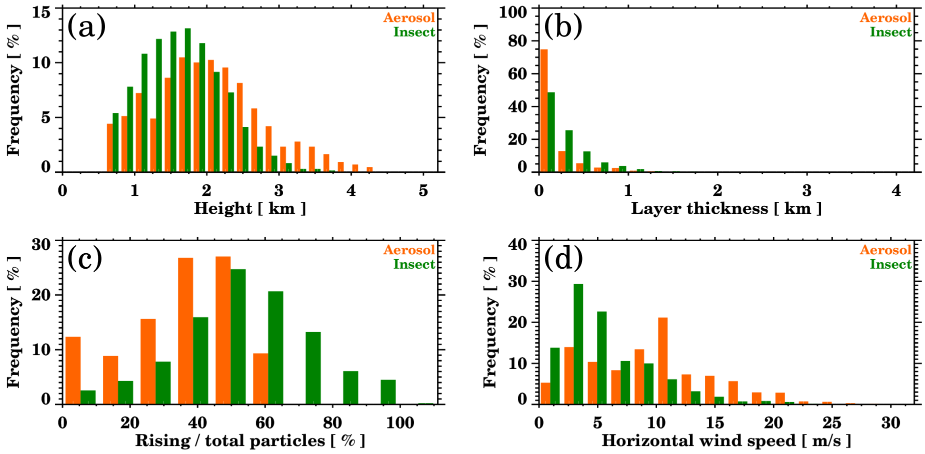

Figure 4.7: *(a) Height distribution of the insect and aerosol layers. (b) Frequency distribution of their thickness. (c) Frequency distribution of the proportion of particles with upwards velocity. (d) Horizontal wind speed forecasted at the layer heights.*

4.2.1 “Orange clouds”: a particular case

Some of the giant aerosol layers observed by the cloud radar have specially high LDR values, ranging from about −5 to 0 *dB*. These layers appear as orange in the false colour images representing the time-height evolution of the radar observations (see an example in *Fig. 4.8*), and are thereby called orange clouds.

Table 4.2 reports the orange clouds observed in Potenza, highlighting a low occurrence compared to the total number of aerosol observations. Nonetheless, these highly depolarizing aerosol observations can have a big impact on air transportation (Madonna et al., 2013). It was the case of the 2010 April and May observations, when the observed orange clouds were related to volcanic aerosol particles coming from the Eyjafjallajökull volcano eruption in Iceland (Madonna et al., 2010, 2013), which caused an enormous disruption to air traffic across western and northern Europe (Pappalardo et al., 2013).

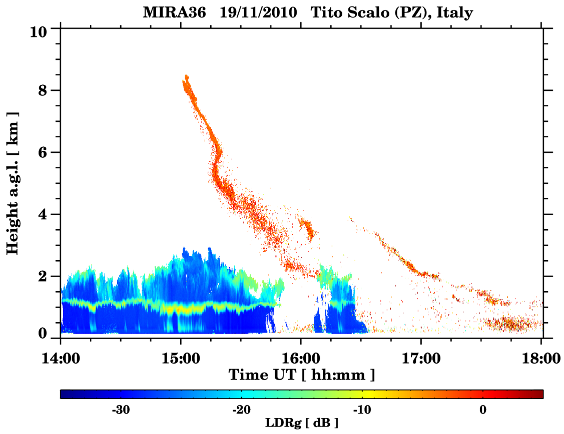

Figure 4.8: *LDR of an orange cloud observation, on 19 November 2010.*

Table 4.2: *Orange clouds observations, including the LDR and Doppler velocity (VEL) mean and standard deviation.*

Case	Date	Time UT [*hh* : *mm*]	Height [*km a.g.l.*]	LDR [*dB*]	VEL [$m\ s^{-1}$]
1	02/02/2010	19:25 - 20:30	0.5 - 2.1	-0.89 ±4.03	-0.47 ±1.42
2	19/04/2010	19:30 - 23:59	1.2 - 2.5	-0.50 ±3.43	-0.23 ±0.78
3	06/05/2010	12:25 - 13:00	4.6 - 5.9	-2.65 ±2.91	0.50 ±0.48
4	07/05/2010	00:00 - 00:30	1.6 - 3.5	-0.71 ±3.66	-0.51 ±0.40
5	10/05/2010	13:20 - 14:55	2.5 - 7.9	-1.70 ±3.18	-0.50 ±0.39
6	13/05/2010	11:20 - 13:00	2.4 - 7.0	-2.21 ±5.50	-0.69 ±1.37
7	04/06/2010	11:30 - 12:45	1.4 - 3.7	-4.00 ±2.38	-2.66 ±1.73
8	19/11/2010	15:00 - 18:10	0.7 - 8.6	-0.58 ±4.41	-0.71 ±0.84
9	10/12/2010	13:00 - 14:10	1.4 - 4.2	-1.33 ±3.31	2.54 ±1.01
10	27/12/2010	14:15 - 14:35	3.2 - 4.4	-1.75 ±6.34	-0.39 ±0.50
11	13/04/2011	14:30 - 18:00	1.1 - 4.3	1.15 ±5.77	0.65 ±1.55
12	10/01/2012	15:40 - 16:05	2.3 - 2.8	-2.74 ±3.20	0.96 ±0.29
13	08/05/2013	04:00 - 06:30	0.9 - 2.8	-2.72 ±3.20	0.15 ±0.35
14	16/10/2013	20:10 - 22:40	1.9 - 4.8	-2.61 ±3.35	-0.01 ±0.81
15	06/02/2014	17:25 - 19:55	0.9 - 3.0	-0.12 ±4.36	-0.32 ±0.41

These layers have generally high vertical velocities, in general larger than 0.5 $m\ s^{-1}$. This unusual feature makes them appear as unnatural layers in the time-height evolution plots. The high vertical velocities along with high LDR are the typical characteristics of chaff particles. They are such as strips of metal, foil or glass fiber with a metal content cut into various lengths and can be used for cloud seeding or military purposes. The cloud seeding, typically, is based on dispersing chemicals or small objects into clouds in order to stimulate or enhance the precipitation formation. The chaff particles are, specially, dry ice crystals or silver iodide particles. When injected into the cloud, they act as nuclei for raindrop formation. The silver iodide particles are used because they have a crystal structure similar to ice. In military operations, chaff particles serve as a radar countermeasure, since they have varying frequency responses and high reflectance.

When chaff particles are introduced into the atmosphere, they tend to generate elongated structures, usually a few kilometers wide per several kilometers long, that can be easily detected by weather radars.

Since we are interested into observing aerosols and not chaff particles, it is necessary to discard the presence of chaff in the observed orange clouds. The best approach to identify chaff is to look for elongated structures in weather radar images, but unfortunately the CIAO observatory is not covered by the national radar network of Italy. In view of this, and considering the horizontal extent of the structures generated by chaff, satellite images provided by SEVIRI have been used instead.

The best way to display the SEVIRI images for our goal is by Red-Green-Blue (RGB) composites: their generation is fast and they are quite efficient for inferring qualitative features of the observed atmospheric targets. Individual channels or channels combinations are attributed to individual colour beams (red, green and blue), and the classification is based on the addition of the RGB colour intensities.

To generate an RGB composite image, after selecting the suitable channels or the differences of channels, an enhancement of the individual colour channels is done in order to get a good contrast and colors in the resulting RGB composite (Roesli et al., 2004). First, a stretching of the intensity ranges (linear stretching of active dynamic range) is performed and then a Gamma correction is applied. This correction changes the overall brightness (and color saturation) of an image. The formula to perform a Gamma correction on a MSG BT image is:

$$BRIT = 255\left[\frac{BT - BT_{min}}{BT_{max} - BT_{min}}\right]^{1/\Gamma} \tag{4.1}$$

where $BRIT$ is the brightness intensity (ranging within 0–255), and

BT_{min} and BT_{max} are the minimum and maximum of the range in which the stretching of intensity range is performed. This range depends on the phenomenon of interest, the season and the time of the day.

The generated RGB composites for the purposes of this study were the “Dust composite" to detect dust intrusions, the “Night Microphysical" to be able to differentiate between different types of clouds and the “High Resolution Visible (HRV)" to see the finest features during day-time. The details of these composites are listed in *Table 4.3*. The channels used for the composites are the 04, 07, 09, 10 and 12. Channel 04 is a window channel close to a CO_2 absorption line in the near infrared, getting contributions from reflected solar and emitted thermal radiation. Channels 07, 09 and 10 are window channels, and thereby they get the maximum signal from the surface and the lower atmosphere. Channel 12 is a broadband visible channel, that has an improved spatial resolution and provides information during day-time only.

Table 4.3: *Generated SEVIRI RGB composites. For each colour beam and composites, the first and second line correspond to the names and channels and the third to the stretching of intensity range. The Gamma correction is 1 for all the cases except for the green colour beam for Dust, in which* $\Gamma = 2.5$. *In the blue colour beam for the HRV composite, the "i" notation stands for inverted.*

RGB composite name	Colour beam Red	 Green	 Blue	Interest
Dust	IR12.0-IR10.8 (ch10-ch09) $[-4, 2K]$	IR10.8-IR8.7 (ch09-ch07) $[0, 15K]$	IR10.8 (ch09) $[261, 289K]$	Dust, thin clouds, contrails
Night Microphysical	IR12.0-IR10.8 (ch10-ch09) [-4, 2 K]	IR10.8-IR3.9 (ch09-ch04) $[0, 10\ K]$	IR10.8 (ch09) $[243, 293K]$	Clouds, fog, contrails
HRV	HRV (ch12) $[0, 100\%]$	HRV (ch12) $[0, 100\%]$	IR10.8i (ch09i) $[323, 203K]$	High resolution visible

The difference between channels *ch10* and *ch09* is small for cirrus and high clouds, medium for water clouds, and almost negligible for dust. The difference between *ch09* and *ch07* is small for cirrus, medium for thick high-level clouds, high for water clouds and medium for dust. The difference between channels *ch09* and *ch04* is large and negative for cirrus (they are more transparent at *ch04* because of the radiation from below), positive for thick high-level clouds and small for low-level clouds. The BT used is from channel *ch09*, becoming brighter as temperatures decrease in the normal case, and vice-versa when inverting the channel (*ch09i*, where *i* stands for inverted). Accordingly, in the "Dust" composite dust appears in pink, low and mid-level clouds in greenish colours and high clouds in dark red colours. In the "Night Microphysical" composite, fog and low clouds appear in light green colors, cirrus in dark blue, and cumulonimbus in dark red. In the "HRV" composite, the observed features have a higher detail. The land appears in brownish colors, the sea in dark blue, the thick high-level clouds in white, the cirrus in light blue and the fog and low clouds in yellow.

The mentioned RGB SEVIRI composites have been generated for all the orange clouds observations and elongated structures searched for in order to discard the presence of chaff. An example is shown in *Figure 4.9*. *Fig. 4.9a* and *b* report the LDR and velocity time-range evolution of the orange cloud event. The orange cloud is clearly distinguished by the high LDR values (the mean LDR is -2.6 *dB*) in *Fig. 4.9a*: it was detected from 20:15 to 22:30 Universal Time (UT) between 1 and 5 *km a.g.l.* and, as a structure, it was loosing height with time. The mean vertical velocity is -0.01 $m\ s^{-1}$, but upwards and downwards velocities can be observed in different time and height regions (*Fig. 4.9b*). At the beginning, before 20:55 UT, the layer had a downwards velocity. Then, it turned upwards until the end of the event except for the upper parts of the layer (over 3 *km* approx.), in which the velocity kept positive values. This may indicate the presence of convection, which counteracted the settling velocity of the aerosol particles. This is confirmed by the fact that the highest upwards velocities are observed around 22:00 UT, when the layer resides between 1 and 2.5 *km a.g.l.* In *Figure 4.9a* and *b*, the purple lines represent the cloud contours, showing the presence of low clouds on top of the boundary layer. The pink dashed line corresponds to the time step shown in *Fig. 4.9c* and *d*. They show the Dust and Night microphysical RGB composites respectively. Both figures indicate the presence of low clouds over the observational site (marked with a black cross), in accordance with the cloud radar observations. Elongated structures are not present around the site, indicating that the radar signals were not affected by chaff particles.

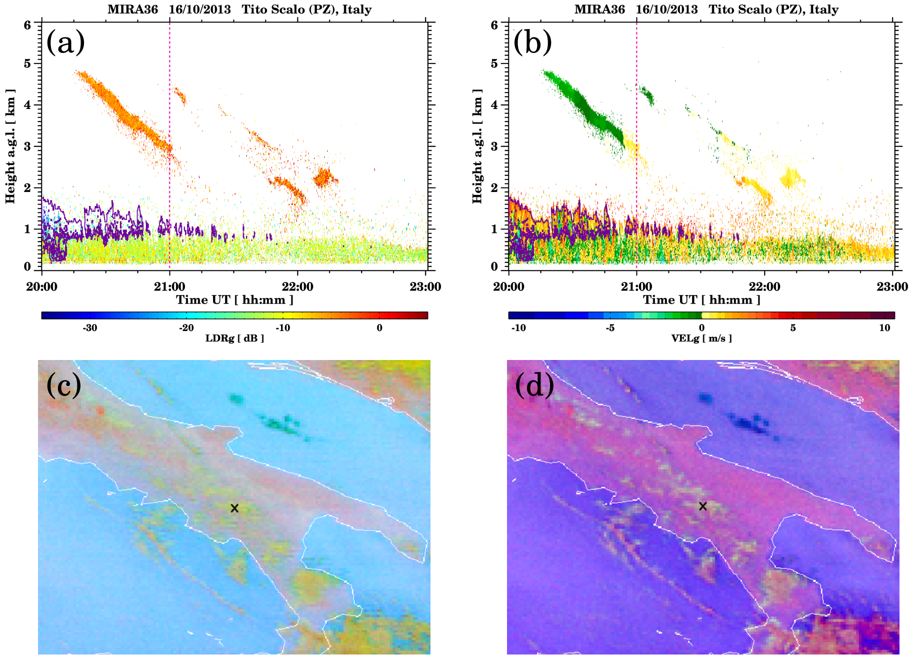

Figure 4.9: *Orange cloud observation on 16 October 2013. Time-height evolution of (a) LDR and (b) velocity between 20:00 and 23:00 UT. The purple lines correspond to the low clouds contours, while the pink dashed line corresponds to the time step of the c and d plots. (c) Dust and (d) Microphysical night RGB composites at 21:00 UT. The black cross indicates the site location.*

4.3 Automatic methodology using Doppler spectra

As described previously, continuous observations of aerosol properties are important for several purposes, including the enhancement of forecast ability of transport models. Accordingly, and given the fact that the cloud radar is operating continuously, an automatic method to detect giant aerosol layers in near real-time is of great interest.

The observational methodology described in *Section 4.1* could be used for this purpose, but the ancillary information that it requires is not always available in near real-time. Therefore, an automatic method based solely on cloud radar data is under investigation. The radar moments and LDR distributions of aerosols and insects (*Fig. 4.5*, *Sect. 4.2*) have proven to be quite similar and cannot be used to discriminate the two targets.

The new radar stand-alone method to detect giant aerosols in near real-time intends to fully exploit the information contained in the Doppler spectra. In principle, the Doppler spectra of aerosols and insects should be intrinsically different: insects move in a more or less random way, whereas aerosols are transported by the air fluxes (wind fields). Consequently, assuming similar atmospheric turbulence conditions, the variability of the Doppler spectra in a very high temporal resolution (in the order of $^1/_2$ *second*) should be higher when insects are present. This concept allows us to define new variables able to better exploit the different features of the two targets. The effectiveness can be tested with the aerosol and insect dataset presented in *Section 4.2*.

The new variables defined in this work were introduced in the radar as a parallel data processing in August 2013 and are calculated by averaging 5 spectra (instead of the typical 200) and then retrieving their variability within 10 *s*. Following, the new variables are defined in detail:

- Moments distribution: the variance of the moments over the time is calculated for the Signal-to-Noise Ratio (SNR), Doppler velocity (VEL) and Peak Width (RMS). Afterwards, the variance of SNR is normalized by its mean value to obtain relative values. The variances of VEL and RMS are normalized by the RMS mean value to maximize the differences between single and distributed targets.

- Random uncertainty (ε): the random uncertainty of the cloud radar measurements is not typically calculated. In principle, this variable is lower for aerosols, since they are more stable than a random target like insects. The random uncertainty of the data is the variability of the spectral lines over the time, as shown in equation (4.2), where fft are the FFT lines:

$$\varepsilon = \frac{\sqrt{\int_{t=0s}^{t=10s}\left(\int_{fft=0}^{fft=255}(var(P_{fft}(t)))^2\,dfft\right)dt}}{\int_{t=0s}^{t=10s}\left(\int_{fft=0}^{fft=255}P(fft,t)\,dfft\right)dt} \tag{4.2}$$

- Spectrum shape (S): the spectrum of an insect can contain several narrow peaks caused by the movement of its wings, a feature that is not observed in aerosols. The shape of a spectrum is calculated by adding all the absolute differences of power between one FFT line and the next and then normalized by its mean power. The spectra shape is the average over the time of all the single spectrum shapes:

$$S = \left\langle \frac{\int_{fft=0}^{fft=254}|P_{fft+1}(fft,t)-P_{fft}(fft,t)|dfft}{\int_{fft=0}^{fft=255}P_{fft}(fft,t)dfft} \right\rangle_{t=10s} \tag{4.3}$$

Figures 4.10 and *4.11* display the distribution of these variables for aerosols and insects. Neither the random uncertainty nor the spectrum shape distributions (*Fig. 4.10*) nor the moments variance (*Fig. 4.11*) show any significant difference for both targets.

Conversely, interrelations of these variables have shown remarkable differences between the two targets, as shown in *Fig. 4.12*. It can be seen that for aerosols (*Fig. 4.12a*), low values of peak width variance in the co-channel correspond to low values in the cross-channel for the same variable and for the random uncertainty in the co-channel. For insects

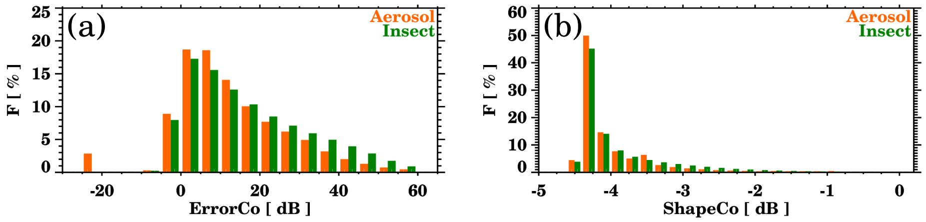

Figure 4.10: *Random uncertainty (a) and spectrum shape (b) distributions in the co-channel.*

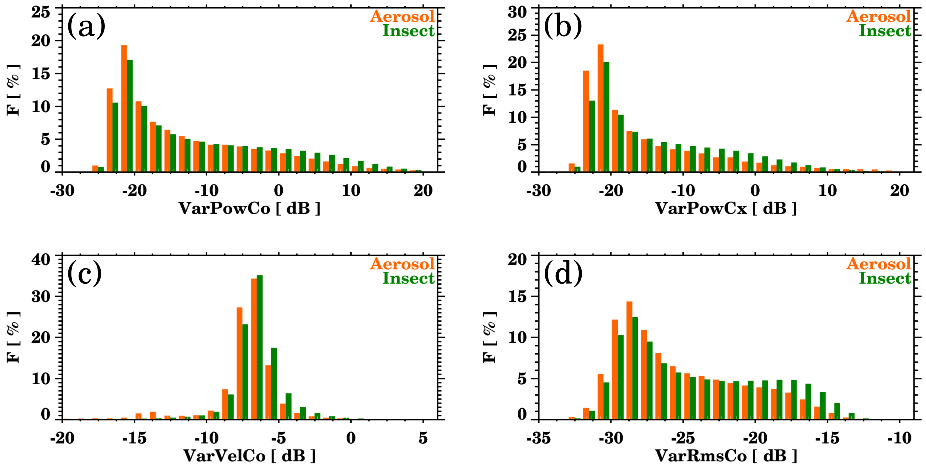

Figure 4.11: *Moments variance distributions of insects and aerosol lofted layers: SNR in the (a) co- and (b) cross-channel, and VEL (c) and RMS (d) in the co-channel.*

(*Fig. 4.12b*), the peak width variances in the two channels have much more spread and the random uncertainty values observed are in general higher. The same effect is observed in *Fig. 4.12c* and *d*, which contain the scatter plot of the variance of velocity versus the variance of peak width together with the random uncertainty, all for the co-channel. Hence, even if the histograms pointed otherwise, the new Doppler spectra based variables can potentially be used to discriminate insects from aerosols. Therefore, more research should be done in this direction in order to create an an automated detection algorithm of giant aerosol layers in near real-time.

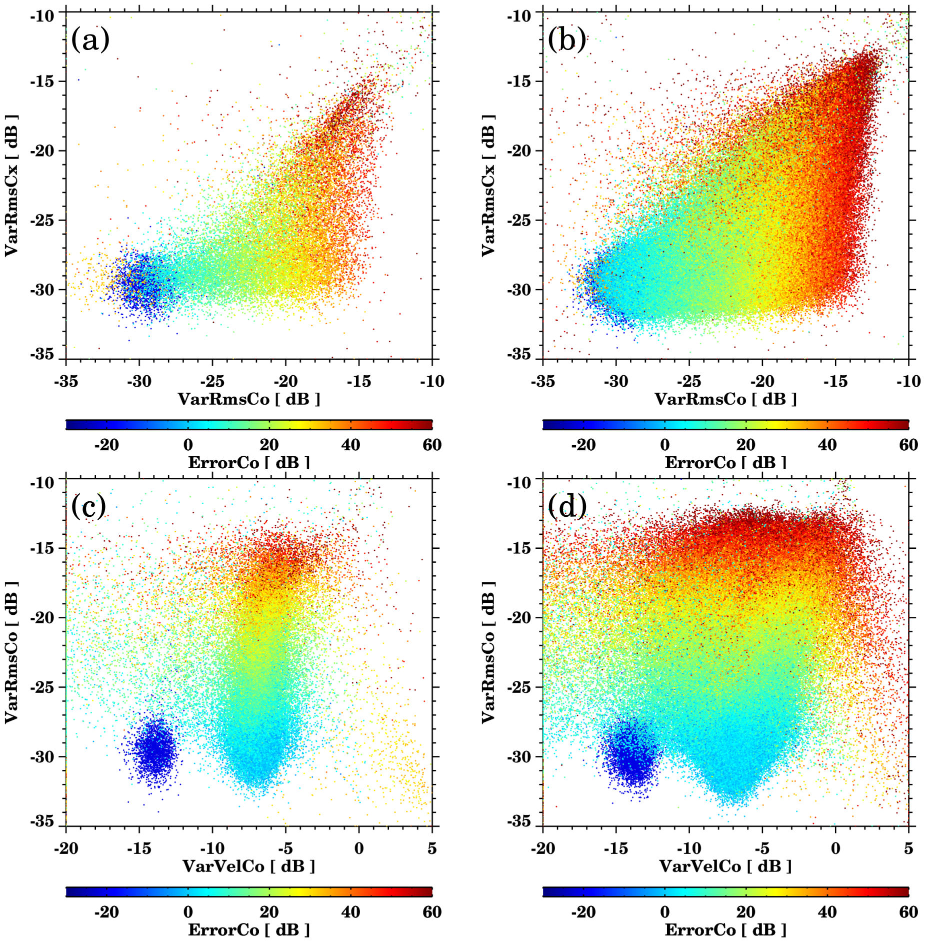

Figure 4.12: *Scatter plot of the variance of the* RMS *in the parallel (VarRmsCo) versus the perpendicular channel (VarRmsCx) together with the random uncertainty (ErrorCo) in the color scale for aerosols (a) and insects (b). Scatter plot of the variance of the* VEL *(VarVelCo) versus the variance of* RMS *(VarRmsCo) in the parallel channel together with the random uncertainty also in the parallel channel (ErrorCo) in the color scale for aerosols (c) and insects (d).*

5

Lidar aerosol observations

Multi-wavelength Raman lidar measurements simultaneous to the cloud radar observation of giant aerosols are analysed in this section.

The lidar systems operating at CIAO are part of the European Aerosol Research LIdar NETwork (EARLINET). Lidar observations within the EARLINET network are performed on a regular schedule: one day-time measurement per week around noon, when the boundary layer is usually well developed, and two night-time measurements per week, with low background light, in order to perform extinction measurements using the Raman technique. In the framework of EARLINET activities, satellite instruments and products are calibrated and/or validated with the networks' lidar systems. Since 2006, the network efforts have been focused on the space-borne Cloud-Aerosol Lidar with Orthogonal Polarization (CALIOP) lidar on-board the CALIPSO (Cloud-Aerosol Lidar and Infrared Pathfinder Satellite Observations) satellite. On average, each EARLINET station performs one to two CALIPSO correlative measurements during daytime and one to two during night for each 16-day CALIPSO repetition cycle. Additionally, simultaneous measurements with other EARLINET stations are predicted in order to study the aerosol temporal variability, or, in case of special events (i.e. measurement campaigns, dust intrusions and volcanic eruptions), to study specific aerosol types and to investigate the geographical representativity of the network observations (Pappalardo et al., 2010).

The lidar observations presented here correspond to aerosols only:

cloud cases are not considered and insects are not detected by the lidar because of its narrow Field Of View (FOV) and its operating wavelengths. Nonetheless, it is interesting to select the lidar aerosol cases according to the target observed by the cloud radar, as the aerosol properties might vary accordingly.

5.1 Lidar cases

For the time period of interest (March 2009 - June 2015), 40 cases of simultaneous measurements have been considered. The list of the cases is summarized in *Tables 5.1* and *5.2*. If these lidar measurements are classified according to the cloud radar observed target, 22 correspond to aerosols and 18 to insects. *Figure 5.1* reports their distribution according to the lighting conditions (day- and night-time), showing that the number of cases for aerosol is the same for day and night while for insects the number of cases during night is much higher.

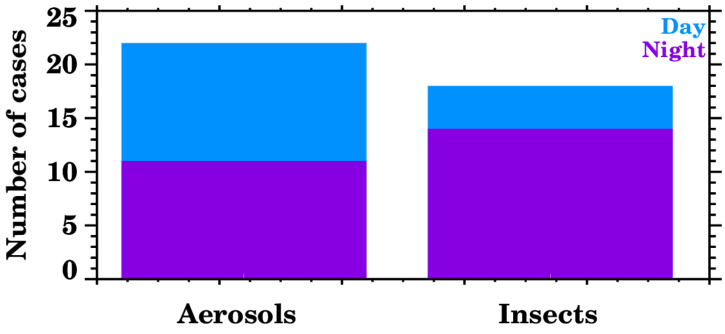

Figure 5.1: *Aerosol lidar measurements matching the aerosol cloud radar dataset, depending on the target observed by the latter.*

As it was described in *Chapter 3*, the Raman lidars at CIAO (MUSA and PEARL) perform measurements for the study of aerosol and clouds. Both lidar systems combine a set of elastic and inelastic channels, consisting of 3 elastic (355 nm, 532 nm and 1064 *nm*) and 2 inelastic Raman (387 nm and 607 *nm*) channels, the so-called 3+2 configuration. This offers the advantage of independent measurements of aerosol extinction and aerosol backscatter coefficient profiles. Moreover, the lidars are able to measure

Table 5.1: *Lidar measurements performed at the site simultaneously to cloud radar giant aerosol observations.*

Conditions	System	Case	Date	Time UT [$hh:mm$]
Day	MUSA	1	12/05/2013	10:52 - 12:20
		2	29/07/2013	13:59 - 14:59
		3	05/08/2013	13:00 - 13:56
		4	23/09/2013	13:05 - 13:35
		5	25/08/2014	14:12 - 15:12
		6	12/01/2015	12:39 - 13:09
		7	12/01/2015	14:30 - 15:00
	PEARL	8	13/07/2009	10:32 - 11:02
		9	10/05/2010	14:00 - 14:15
		10	13/05/2010	11:55 - 12:03
		11	20/05/2013	12:10 - 13:11
Night	MUSA	12	19/06/2013	19:27 - 19:57
		13	16/09/2013	18:15 - 18:43
		14	19/09/2013	19:09 - 20:09
		15	23/09/2013	17:40 - 18:56
		16	26/09/2013	18:00 - 18:59
		17	18/02/2014	17:52 - 18:23
		18	03/07/2014	21:09 - 21:39
		19	16/10/2014	19:00 - 19:30
	PEARL	20	13/07/2009	19:45 - 21:15
		21	19/04/2010	20:03 - 20:33
		22	17/06/2013	19:27 - 21:13

Table 5.2: *Lidar measurements performed at the site simultaneously to cloud radar insect observations.*

Conditions	System	Case	Date	Time UT [*hh* : *mm*]
Day	MUSA	23	08/08/2011	12:39 - 12:59
		24	29/08/2012	10:44 - 11:04
		25	29/08/2012	13:23 - 13:53
		26	25/10/2012	11:55 - 13:51
Night	MUSA	27	18/11/2009	00:00 - 00:30
		28	26/08/2010	18:52 - 19:37
		29	18/08/2011	19:15 - 19:35
		30	09/08/2012	20:47 - 21:18
		31	22/07/2013	19:21 - 21:40
		32	05/08/2013	18:54 - 19:28
		33	22/05/2014	19:29 - 21:10
		34	23/06/2014	20:00 - 21:00
		35	25/06/2014	00:10 - 00:50
		36	30/06/2014	20:08 - 20:38
		37	03/07/2014	19:33 - 20:33
		38	04/08/2014	21:50 - 22:20
		39	04/05/2015	20:40 - 21:20
		40	29/05/2015	21:51 - 22:51

the depolarization of the linearly emitted radiation. The retrieved linear particle depolarization ratio is a type-determining parameter, as it provides information on the shape of the particles.

In the following, three examples of lidar data analysis from *Table 5.1* are presented: 2, 12 and 18. They correspond to mixed dust, smoke and dust particle observations respectively.

Case 2: 29/07/2013

The first case presented here describes measurements of Saharan dust particles that prior to arriving over the site were subject to mixing with anthropogenic pollution. The measurements at CIAO were performed on 29 July 2013. The evolution of the observed aerosol load is depicted in *Figure 5.2* as time-height evolution of the lidar Range Corrected Signal (RCS). Aerosol is observed from the ground up to 4 *km a.g.l.* The main aerosol layer is located in the range between 1 and 2.5 *km*. Thin aerosol layers are also found up to 4 *km*. Below 1 *km* the evolution of the CBL is also evident as the CBL and free tropospheric aerosol are well separated throughout the measurement period.

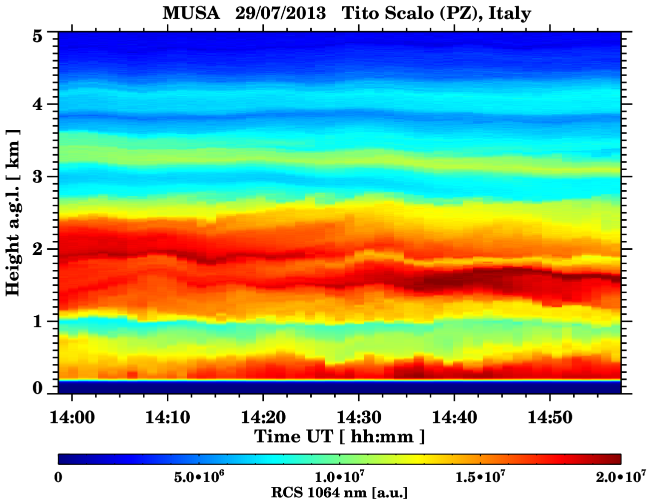

Figure 5.2: *Time-height evolution of the RCS at 1064 nm for 29 July 2013 between 13:59 and 14:59 UT, measured by MUSA.*

In this case, the measurements took place during day-time, when the Raman backscattered signal cannot be measured accurately owing to the solar background radiation. Consequently, the extinction profiles cannot be retrieved in an independent way. *Figure 5.3* displays the lidar extensive and intensive optical properties. The particle backscatter coefficient profiles (hereinafter backscatter, *Fig. 5.3a*) show the location of the various aerosol layers, as identified in the time-height evolution. The backscatter related Ångström exponents (*Fig. 5.3b*) are separated into two parts with different characteristics. The first presents stable values greater than 1 up to 1 *km*, indicating small particles originating from anthropogenic activities within the CBL. The second displays values well below 1 above 1 *km* suggesting the existence of bigger particles. *Figure 5.3c* shows a linear particle depolarization ratio (hereinafter particle depolarization) over 10% for the aerosols over 1 *km*: about 13% up to 1.9 *km* and approximately 11% from this height up to 4.5 *km*. The estimated depolarization along with the low Ångström values highlights the mixing of dust particles with low depolarizing particulates - i.e., smoke, anthropogenic pollution (Heese and Wiegner, 2008; Burton et al., 2012; Groß et al., 2015), and it can be considered that the observed aerosols in this case correspond to aged dust.

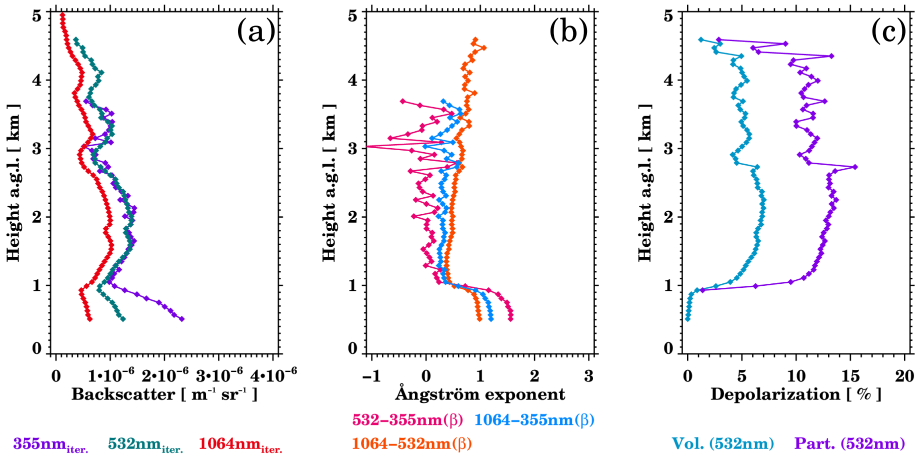

Figure 5.3: *MUSA lidar analysis for 29 July 2013 between 13:59 and 14:59 UT. Profiles of (a) particle backscatter coefficient, (b) Ångström exponent backscatter related and (c) volume and linear particle depolarization ratio. The vertical resolution is of 30 m.*

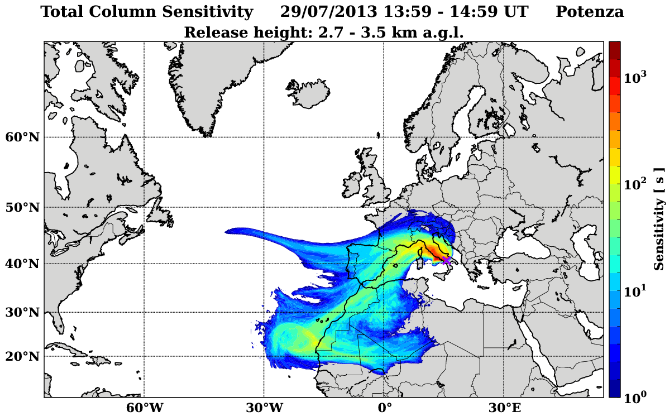

Figure 5.4: *Total column sensitivity for a 7-days FLEXPART back-trajectory analysis starting on 29 July 2013 (from 13:59 to 14:59 UT) between 2.7 and 3.5 km a.g.l.*

FLEXPART was used to identify the possible source region of the observed aerosols. The output of the simulation for this case is depicted in *Figure 5.4*, and it shows that, backwards, the air-parcels followed a northward motion over the Italian peninsula before looping towards the north-west of Africa. The travelled path reveals the potential sources of the observed aerosol features. The observed layers were originating from NW Sahara regions and crossed the heavily polluted area of Po valley prior to arrival over the site. Summing up, the aerosol observations coupled with model simulations show the mixing of dust particles with anthropogenic pollution.

Case 12: 19/06/2013

The second measurement example describes the observation of biomass burning aerosol, collected at CIAO on 19 June 2013. The height-time evolution of the RCS at 1064 *nm* is shown in *Figure 5.5*. A stratified aerosol load is measured from the ground up to 3 *km a.g.l.* Two main features can be identified: first, an aerosol layer is located near the ground and represents the well mixed residual layer, and second, a thicker optical layer extending from 2 to 2.5 *km*.

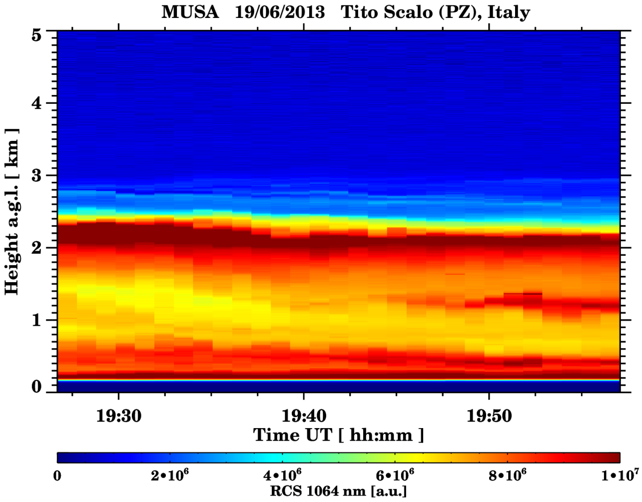

Figure 5.5: *Time-height evolution of the RCS at 1064 nm for 19 June 2013 between 19:27 and 19:57 UT, measured by MUSA.*

The lidar extensive and intensive optical properties are shown in *Figure 5.6*. The lidar ratio (*Fig.5.6c*) is around 60 *sr* at 355 *nm* and 80 *sr* at 532 *nm*. The backscatter and extinction related Ångström exponents (*Fig.5.6d*) are approximately 1, values that correspond to absorbing particles. The small values of depolarization (5-6%) correspond to almost spherical particles. The intensive optical properties designate that, most likely, the observed aerosol particles correspond to smoke or urban particles (e.g., Amiridis et al., 2010; Burton et al., 2013).

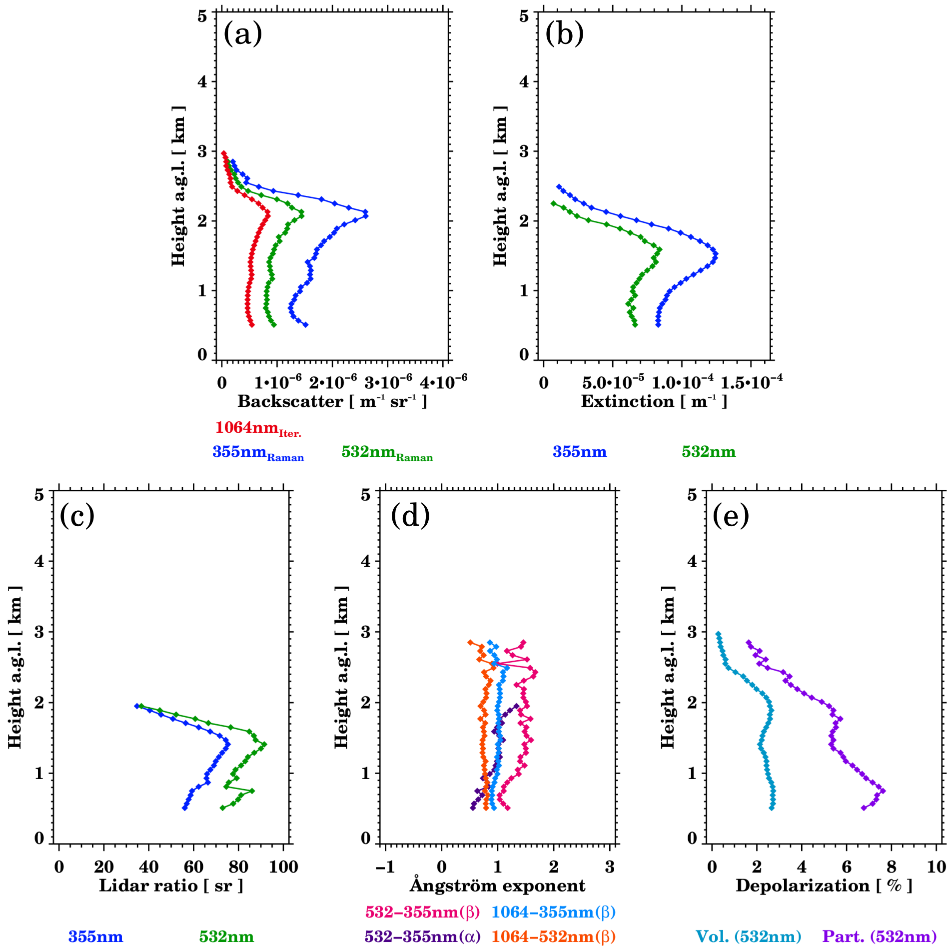

Figure 5.6: *Musa lidar analysis for 19 June 2013 between 19:27 and 19:57 UT. Profiles of (a) particle backscatter coefficient, (b) particle extinction coefficient, (c) lidar ratio, (d) Ångström exponent backscatter and extinction related and (e) volume and linear particle depolarization ratio. The vertical resolution is of 210 m.*

The possible origin and transport path of the measured aerosols were investigated using FLEXPART model and the active fire product from MODIS. Flexpart was used in the backward mode to identify the areas that could contribute to the measured aerosol load. The simulation was performed considering a 7-day-long period. Flexpart total column sensitivity plot (*Fig. 5.7*) indicates the travelled path of the aerosols prior to arriving at the measuring site. The air masses followed an eastward direction towards Greece and then moved north and, finally, extended westwardly. The MODIS active fire product (*Fig. 5.8*) identified several active fires, before the aerosol layers were observed, along the path of the air masses. Hence, the source of the observed layer can be ascribed to the presence of forest fires burning over the Balkans.

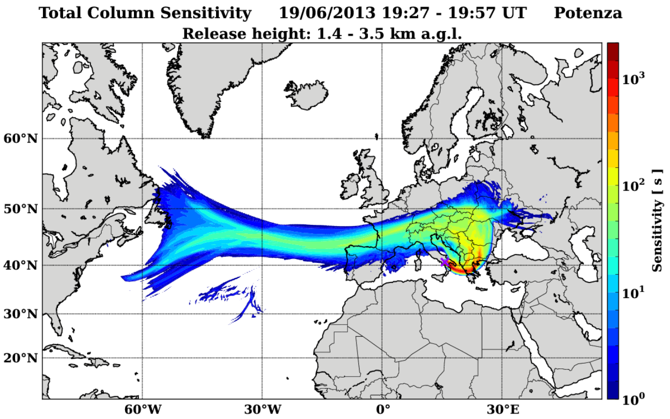

Figure 5.7: *Total column sensitivity for a 7-days FLEXPART back-trajectory starting on 19 June 2013 (from 19:27 to 19:57 UT) between 1.4 and 3.5 km a.g.l.*

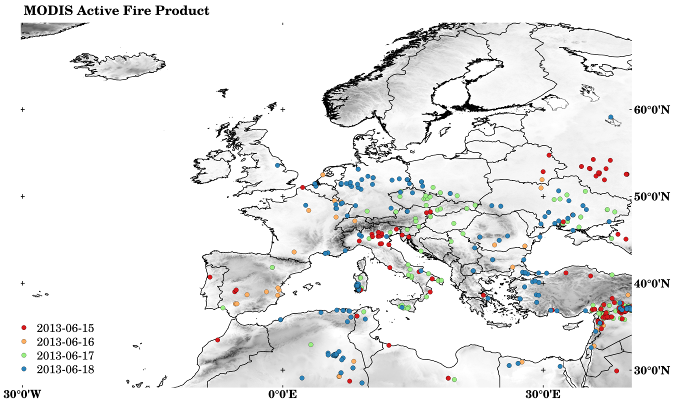

Figure 5.8: *Modis active fire product 1, 2, 3 and 4 days prior to 19 June 2013.*

Case 18: 03/07/2014

The last examined case describes a typical dust transport event, observed at CIAO on 3 July 2014. *Figure 5.9* depicts the height-time evolution of the aerosol as observed by the lidar. Aerosol layers are observed from the ground up to 6 *km a.g.l.* The layers can be separated in a well mixed ABL extending up to 1.1 *km* and a lofted layer between 2.8 and 5 *km a.g.l.*

The latter layer, as can be seen by the RCS, consists of dense and persistent aerosol load.

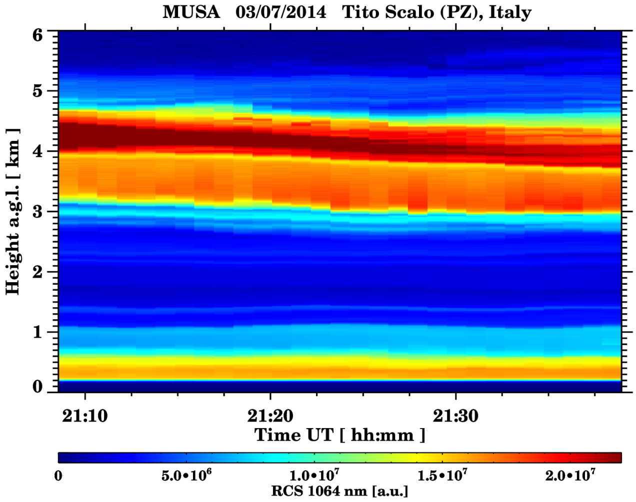

Figure 5.9: *Time-height evolution of the RCS at 1064 nm for 3 July 2014 between 21:09 and 21:39 UT, measured by MUSA.*

The optical coefficients and the intensive optical properties profiles derived by the multi-wavelength Raman lidar can be seen in *Figure 5.10*. The backscatter and extinction profiles (*Fig. 5.10a* and *b*) show the two separate layers: one from the surface to 1.2 *km a.g.l.* and another between 2.4 and 5 *km a.g.l.* The lidar ratio of the upper layer is about 50 *sr* and shows a small wavelength dependency. The extinction and backscatter related Ånsgtröm exponent (*Fig. 5.10d*) presents high values for the lower layer (around 1), indicating the presence of small particles. The values for the upper layer, instead, are around 0, revealing the presence of large particles. The depolarization ratio (*Fig. 5.10e*) for the lofted layer is over 30%. These findings show that, in this case, the upper layer corresponds to fresh dust particles.

To confirm the possible origin of the observed aerosol type, transport simulations were performed using the FLEXPART dispersion model. *Figure 5.11* shows the resulting total column sensitivity of the lofted layer region. The plot indicates that air-parcels originate from the Sahara region were transported to the observational site following a path through western Mediterranean.

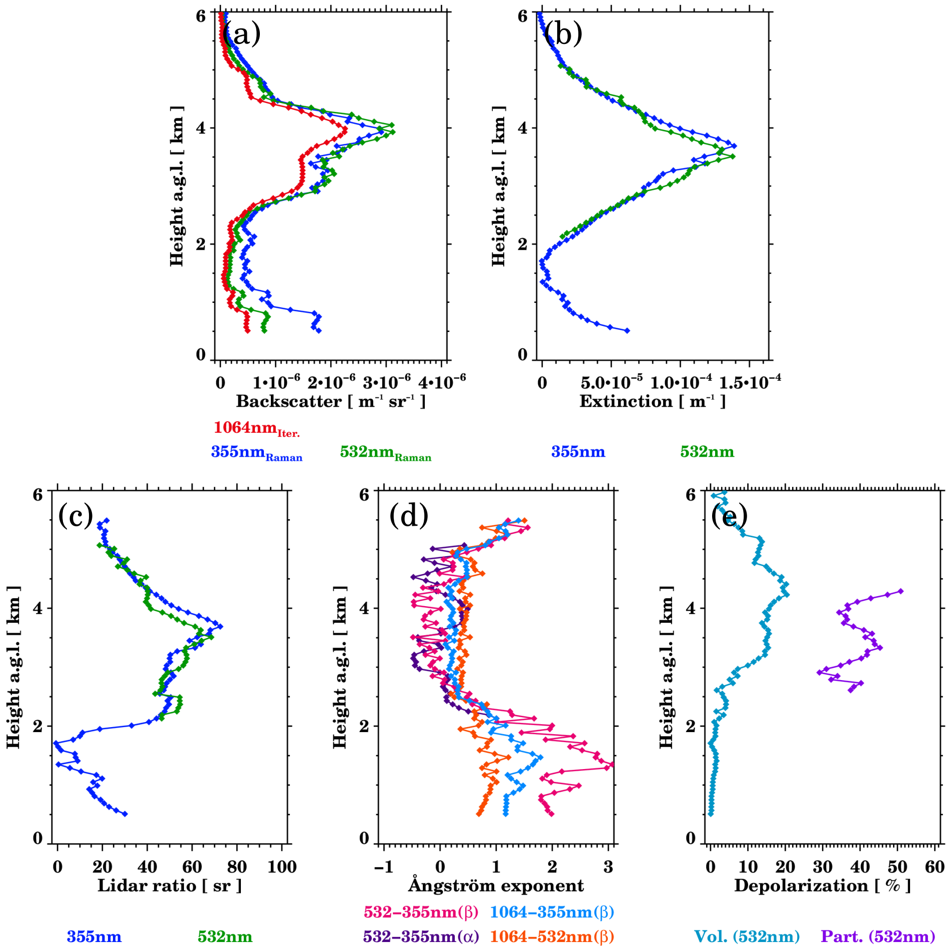

Figure 5.10: *Musa lidar analysis for 3 July 2014 between 21:09 and 21:39 UT. Profiles of (a) particle backscatter coefficient, (b) particle extinction coefficient, (c) lidar ratio, (d) Ångström exponent backscatter and extinction related and (e) volume and linear particle depolarization ratio. The vertical resolution is of 210 m.*

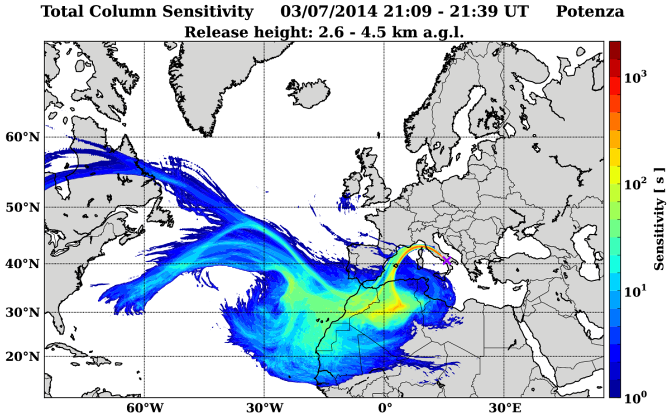

Figure 5.11: *Total column sensitivity for a 7-days* FLEXPART *back-trajectory analysis starting on 3 July 2014 (from 21:09 to 21:39* UT*) between 2.6 and 4.5 km a.g.l.*

5.2 Lidar statistics

For better understanding of the different behaviour of giant aerosol and insects in terms of aerosol optical properties (backscatter, extinction, lidar ratio, Ångström exponent and depolarization ratio), a statistical study on these variables has been carried out.

The analysis is performed for all the lidar cases, separating them according to the cloud radar target classification, as listed in *Tables 5.1* and *5.2*. *Table 5.3* reports the number of available layers for each optical property. The number of layers is not constant for all the properties. Extinction profiles, for example, are only available during night, and depolarization information is considered for MUSA measurements only. Other differences in the number of layers considered, for example for backscatter at different wavelengths, can be due to low Signal-to-Noise Ratio (SNR) values or to quality assurance of the estimated properties.

First, the mean and the standard deviation is calculated for each optical property retrieved from the lidar considering the mean of each layer. As already mentioned, all the optical properties presented in this chapter correspond to aerosols, but they have been classified according to the cloud radar detected target to identify possible differences. *Figure 5.12* presents the mean values of the lidar extensive optical properties. The

Table 5.3: *Number of available layers for each optical property considered for the lidar statistics analysis. They are classified according to the observed cloud radar target.*

Optical property	Wavelength [*nm*]	Target by cloud radar Aerosol	Target by cloud radar Insect
Backscatter	355	21	17
	532	19	17
	1064	21	18
Extinction	355	11	12
	532	5	13
Ångström exponent (α)	532–355	3	11
Ångström exponent (β)	1064–532	20	18
	532–355	19	18
	1064–355	20	18
Lidar ratio	355	10	12
	532	5	13
Volume depolarization	532	13	15
Particle depolarization	532	13	15

backscatter (*Fig. 5.12a*) yields similar values for both targets at all wavelengths, and the same behaviour is observed for the extinction (*Fig. 5.12b*). In the last case, though, not taking into account the large standard deviation, a different spectral behaviour can be observed. The mean extinction at 355 *nm* is lower than at 532 *nm* when insects are present, whereas for aerosols, the situation is reversed and the difference between the two extinctions is higher. The possible explanation for this fact is that bigger aerosols are observed by the lidar when the radar detects insects, resulting in the observed spectral independence.

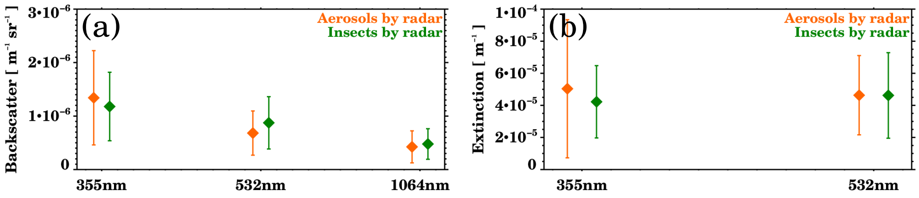

Figure 5.12: *Mean lidar extensive optical properties according to the target detected by the cloud radar: (a) backscatter and (b) extinction. The vertical bars correspond to the standard deviation.*

The intensive mean optical properties are shown in *Fig. 5.13*. The lidar ratio (*Fig. 5.13a*) shows the same effect already noted in extinction: the spectral dependency is lower when insects are present. The Ångström exponent (*Fig. 5.13b*) is very similar for both targets, indicating similar particle sizes independently of the cloud radar observed target. Hence, and along with the high standard deviation, this dependence will not be considered as relevant. The depolarization values (*Fig. 5.13c*) are also very similar for both targets, indicating the particle shape observed by the lidar is approximately the same independently of the cloud radar observed target.

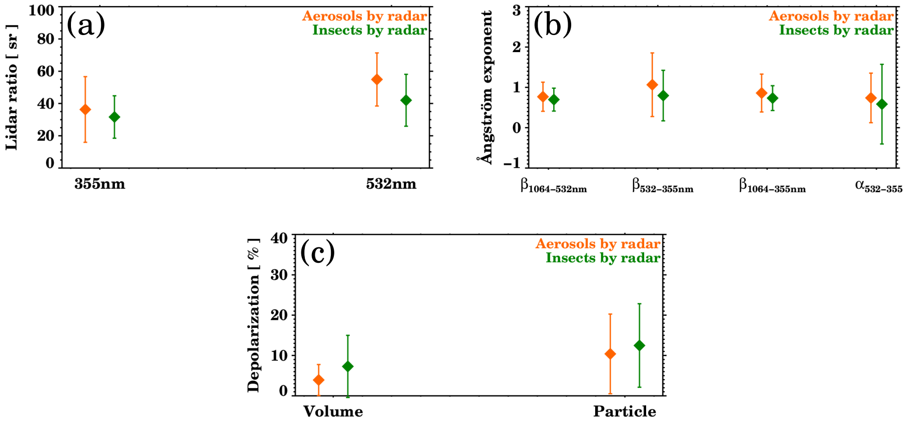

Figure 5.13: *Mean lidar intensive optical properties according to the target detected by the cloud radar: (a) lidar ratio, (b) Ångström exponent and (c) volume depolarization and linear particle depolarization. The vertical bars correspond to the standard deviation.*

In the following, some scatter plots for various sets of the layer parameters are presented. The plots intend to quantify and discriminate the observations into clusters. Some examples are presented in *Figures 5.14* and *5.15*.

The linear particle depolarization ratio versus the Ångstöm exponent backscatter related for two pairs of wavelengths (1064–355 *nm* and 1064–532 *nm*) is presented in *Figure 5.14*. Generally, high values of depolarization correspond to low Ångström exponents, while low depolarizations correspond to higher Ångström exponents. This indicates that the small particles observed are usually spherical and big particles are frequently irregular. No major differences are observed depending on the cloud radar detected target.

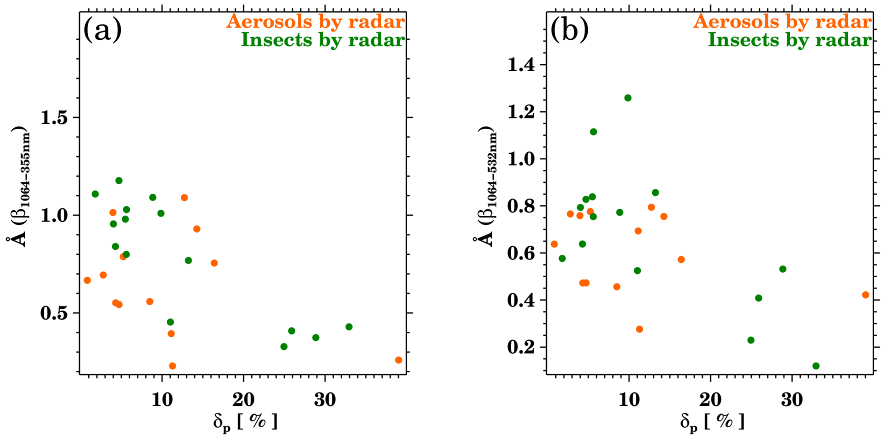

Figure 5.14: *Scatter plots of linear particle depolarization ratio versus Ångström exponent (backscatter related) for two pairs of wavelengths: 1064–355 nm (a) and 1064–532 nm (b). The layers are labelled according to the cloud radar observed target.*

Figure 5.15 presents the layer mean height versus the Ångström exponent extinction related. As in the previous figure, no major differences are observed depending on the radar detected target, and it seems that there is no dependency of the Ångstöm exponent with height.

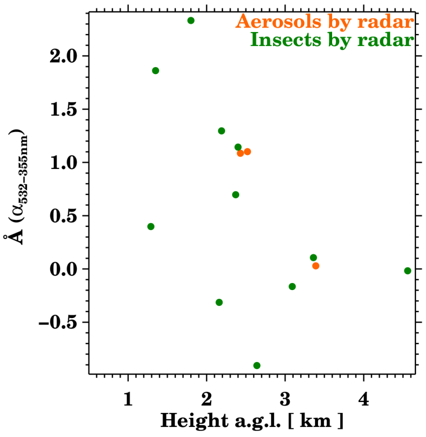

Figure 5.15: *Scatter plot of height of the layers versus its Ångström exponent (extinction related). The layers are labelled according to the cloud radar observed target.*

Finally, the potential sources for each of the aerosol layers is investigated. Flexpart was used in the backward mode to identify the areas that could contribute to the measured aerosol load. The simulation was performed for all the lidar cases considering a week-long period. In order to illustrate the complex situation coming from every simulation, we estimated the mean back-trajectory for the aerosol and insects categories separately. The scope of these plots is to highlight the sources of the observed aerosol layers.

The total column sensitivity for all the aerosol layers (*Fig. 5.16*) does not present major differences depending on the target that the cloud radar observed. Both for aerosols (*Fig. 5.16a*) and insects (*Fig. 5.16b*), the western flux of air masses can be clearly observed. As it is obvious, the sensitivity around the site is the highest. The highest values for the aerosol cases are located mainly over the western coast of Italy, the Tyrrhenian sea and the Genoa gulf, while for insects are located mainly above the eastern Italian coast and the Adriatic sea. In both cases the provenance of air masses from the north-west of Africa is clear, even if the origin regions vary slightly depending the target.

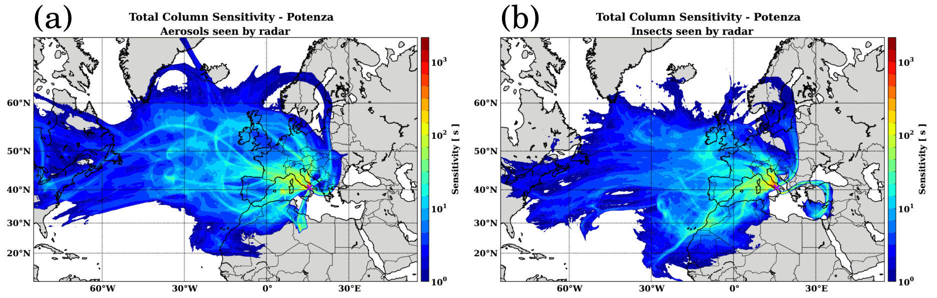

Figure 5.16: *7-days FLEXPART back-trajectory analysis total column sensitivity averaged for all the aerosols (a) and insects (b) layers. The purple cross indicates the site location.*

The FLEXPART footprint plot (*Fig. 5.17*) indicates the impact of the ground level uptake of particulate matter, and is also called ground-level sensitivity. This product offers the capability to evaluate the strength of ground sources in the area of interest, since it shows the ground-level regions that are likely to affect the aerosol loading over the observational site. For the cases classified as aerosols by the cloud radar (*Fig. 5.17a*), the ground level uptake of particles is produced, mainly, over the ground close to the site, the Adriatic sea at the north of the site and over western Mediterranean. There are also some uptakes over the Sahara desert and the Cantabric sea. For the cases classified as insects by the cloud radar (*Fig. 5.17b*), the major uptake of particles is produced in the surroundings of the site and over the Adriatic sea at the north of the site. In this case, the sensitivity at footprint is much higher than in *Fig. 5.17a*. The air masses arriving at the site in this case are also occasionally reaching the ground in central Europe, in western Mediterranean, and at the northern part of the Sahara desert.

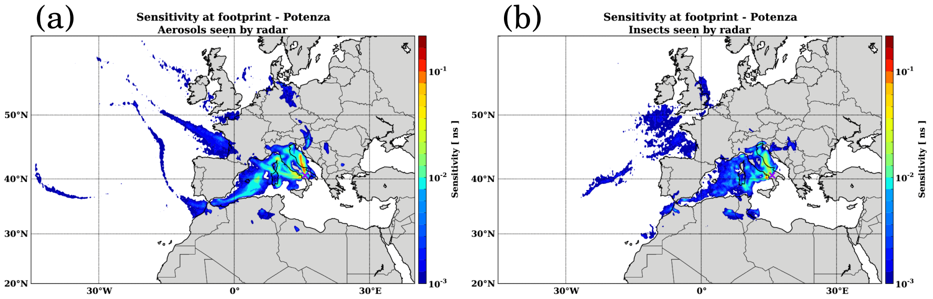

Figure 5.17: *7-days* FLEXPART *back-trajectory analysis sensitivity at footprint for all the aerosols (a) and insect (b) cases. The colour designated areas correspond to the impact of the ground level uptake of particulate matter. The purple cross indicates the site location.*

6

Cloud radar and lidar synergy

In this chapter, the lidar and radar measurements are compared in terms of backscattered radiation and depolarization and the retrieval of the aerosol microphysical properties using these measurements is described.

The lidar and cloud radar operating wavelengths differ several orders of magnitude. Accordingly, they are sensitive to different particle size ranges. In order to quantify their capability to detect different particle effective radii, the T-matrix method for randomly oriented, rotationally symmetric scatterers (Mishchenko et al., 1996) has been used to compute the extinction and scattering efficiency (Q_{ext} and Q_{sca} respectively) of aerosols at the various wavelengths. These calculations necessitate the a priori inference of the aerosol complex refractive index. For the three lidar wavelengths, the value was set to $1.59 - 0.009i$, indicative of dust particles. Kandler et al. (2007) estimated the complex refractive index for visible light by averaging dust mineralogical data observed in the Canary Islands. For the radar wavelength, the complex refractive index used is $2.45 - 0.43i$, corresponding to volcanic particles at 35.5 *GHz* (Adams et al., 1996).

Figure 6.1 displays the extinction and scattering efficiencies depending on the radius for the three lidar wavelengths (355, 532 and 1064 *nm*) and the radar wavelength (8.45 *mm*). Moreover, the efficiencies have been estimated for three different axis ratios (which is the ratio between the major and minor axis of an spheroid). The efficiencies could be computed

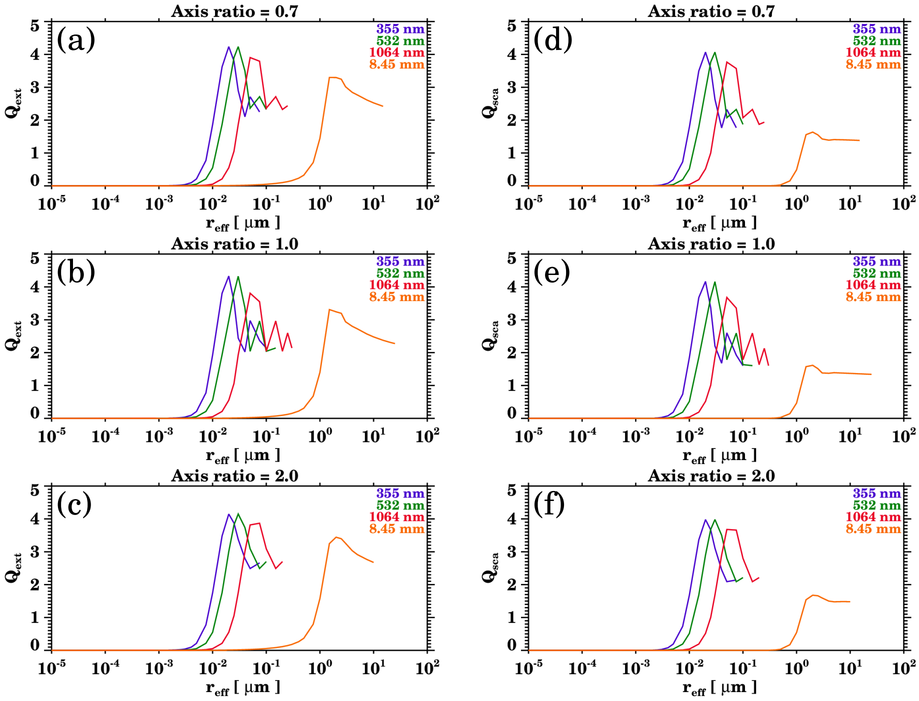

Figure 6.1: *Extinction and backscattering efficiencies at the three lidar wavelengths (355, 532 and 1064 nm) and at the radar wavelength (8.45 mm) for different axis ratios. Extinction efficiency for axis ratios of (a) 0.7, (b) 1.0 and (c) 2.0. Backscattering efficiency for axis ratios of (d) 0.7, (e) 1.0 and (f) 2.0.*

up to size parameters equal to 200, according to the T-matrix scattering model stability. As explained in *Chapter 2* (equation 2.5), the efficiencies indicate the proportion of the incident light diverted into a certain process. The extinction efficiency (*Fig. 6.1a*, *b* and *c*) comprises scattering and absorption processes. The differences between the extinction efficiencies at the different wavelengths are clear: while at the lidar wavelengths it starts to increase for aerosol particles slightly above 1 *nm*, for the radar it does so above 0.1 μm. Expectedly, the shorter the wavelength, more sensitive becomes to smaller particles. The shape of the curves is affected by the complex refractive index, the size parameter and the axis ratio of the particles. The oscillating character of the lidar curves is prominent for spherical particles (*Fig. 6.1b*), an effect less evident for prolate particles (*Fig. 6.1a*) and even less for oblates (*Fig. 6.1c*). The backscattering efficiency (*Fig. 6.1d*, *e* and *f*) at the lidar wavelengths is very similar to the extinction efficiency, whereas at the radar wavelength the scattering efficiency yields lower values than the extinction efficiency.

This can be attributed to the absorbing component of the refractive index - i.e, the imaginary part. For the lidar wavelengths, the imaginary part used is 0.009 whereas for the radar wavelength is 0.43.

6.1 Backscatter and depolarization comparison

Since lidar particle backscatter coefficient (backscatter hereinafter) and equivalent radar reflectivity (reflectivity henceforth) reflect almost the same physical parameter; a methodology to convert the radar reflectivity into backscatter has been applied to compare the measurements of the two instruments using the same magnitude.

The lidar wavelength is small compared to the scatterers, and therefore, applying the geometric optics approximation, the backscatter coefficient, β, can be estimated as:

$$\beta \propto ND^2 \tag{6.1}$$

where β is in $m^{-1}sr^{-1}$, N is the number concentration and D is the diameter of the particles.

Cloud radars operate in the Rayleigh regime, according to their wavelength and the atmospheric targets they sample. Thus, the scattering efficiency can be estimated as (Van de Hulst, 1957):

$$Q_{sca} = \frac{8}{3}\, x^4 \left| \frac{m^2-1}{m^2+2} \right|^2 \tag{6.2}$$

where x is the size parameter and relates the particle radius to the wavelength (equation 2.1, *Chapter 2*), and m is the refractive index, an optical parameter associated with the velocity change of electromagnetic waves in a medium with respect to vacuum. Normally, the refractive index of atmospheric particles and molecules is composed of a real part m_r and an imaginary part m_i corresponding, respectively, to the scattering and absorption properties of particles and molecules. Usually, $|K|^2$ is used to indicate the third factor of the equation 6.2.

In the regime of Rayleigh scattering, neglecting polarization effects of small scattering particles, the phase function can be obtained as:

$$R(\theta) = \frac{1}{4\,\pi}\,\frac{3}{8}\,(1+\mu^2) \tag{6.3}$$

For the backscattered radiation, $\theta = \pi$ and $\mu = cos(\theta) = -1$. Therefore, the phase function in the Rayleigh domain is:

$$R(\pi) = \frac{1}{4\,\pi}\,\frac{3}{8}\,(1+(-1)^2) = \frac{3}{2^4\,\pi} \tag{6.4}$$

Then, from equation 2.4 (*Chapter 2*), the backscatter over all the particle sizes is:

$$\beta = C^{\pi}_{sca} = \pi \int_0^{\infty} r^2\; n(r)\; Q_{sca}\; R(\pi)\; dr \tag{6.5}$$

By introducing equations 2.1 (*Chapter 2*), 6.2 and 6.4 into 6.5:

$$\beta = \pi \int_0^{\infty} r^2\; n(r)\; \frac{8}{3} \left(\frac{2\,\pi\,r}{\lambda}\right)^4 |K|^2\; \frac{3}{2^4\,\pi}\; dr \tag{6.6}$$

Equation 6.6 can be also written as:

$$\beta = \frac{2^3\,\pi^4\,|K|^2}{\lambda^4} \int_0^{\infty} r^6\; n(r)\; dr \tag{6.7}$$

From the radar equation, we know that the radar reflectivity Z is:

$$Z = \int_0^{\infty} D^6\; n(D)\; dD \tag{6.8}$$

Equation 6.8 can be also expressed as:

$$Z = \int_0^{\infty} (2\,r)^6\; \frac{1}{2}\; n(r)\; dr = 2^5 \int_0^{\infty} r^6\; n(r)\; dr \tag{6.9}$$

Merging equations 6.7 and 6.9, the backscatter coefficient is given as:

$$\beta = \frac{2^3\,\pi^4\,|K|^2}{\lambda^4}\,\frac{Z}{2^5} = \frac{\pi^4\,|K|^2}{4\,\lambda^4}\,Z \tag{6.10}$$

By applying equation 6.10 to the radar data, it is possible to directly compare the lidar and radar backscatter coefficients. The application of the methodology is presented in the following for the three cases already discussed.

Case 2: 29/07/2013

The time-height evolution for this mixed dust case is in *Figure 6.2*. Several layers are detected by the lidar (*Fig. 6.2a*) spanning from the ground up to 4.3 *km a.g.l.*, while only a tenuous lofted layer around 3 *km a.g.l.* is detected by the cloud radar.

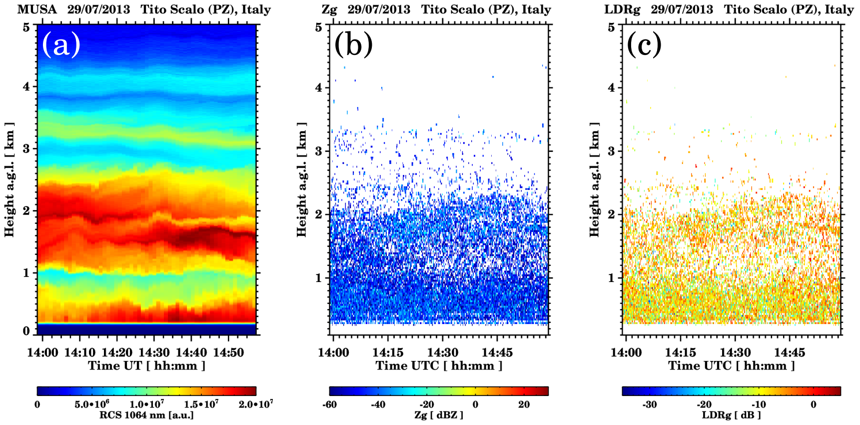

Figure 6.2: *Time-height evolution of (a) the lidar RCS at 1064 nm, (b) the cloud radar reflectivity, and (c) the LDR for 29 July 2013 between 13:59 and 14:59 UT.*

The lidar and radar backscatter comparison (*Fig. 6.3a*) illustrates the different layers. The enhanced signal up to 2 *km* is evident for both instruments and is expected considering the influence of the CBL. The lofted layer location seen by the radar coincides with the retrieved lidar stratification. The LDR (*Fig. 6.3b*) is clearly different for the two sensors: while it is almost constant for the lidar above 1 *km a.g.l.*, for the radar is much higher in the CBL than above.

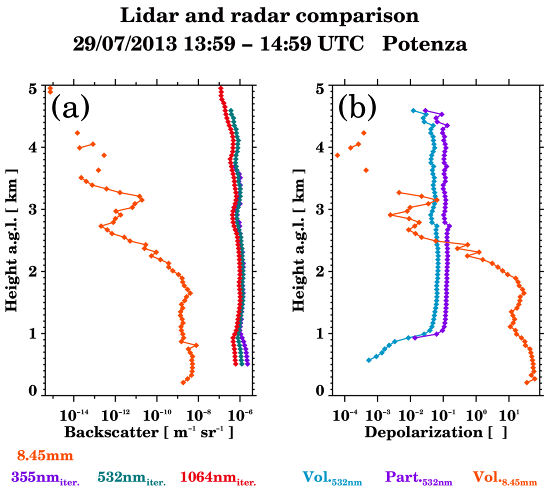

Figure 6.3: *Lidar and radar (a) bakscatter coefficient and (b) depolarization ratio comparison for 29 July 2013 between 13:59 and 14:59 UT.*

Case 12: 19/06/2013

The time-height evolution of lidar RCS, radar Reflectivity (Z) and radar LDR observed in *Fig. 6.4* illustrates the eminent biomass burning plume up to 3 *km* as seen by the lidar, while for radar a thin layer around 3 *km* was observed. The LDR sensitivity of the MIRA36 radars is of -35 *dB*. As this is the ratio between the signal received in the cross-channel versus the co-channel, the LDR is below the sensitivity threshold when the SNR values of the cross channel are low.

Figure 6.5 contains the backscatter and depolarization profiles obtained with the lidar and the radar. In the backscatter profiles (*Fig. 6.5a*), the order of magnitude of the difference between the backscattered signal of the two sensors is the first thing that can be noticed. The CBL height detected by the two instruments is also different, and it is lower for the radar observations. Regarding the upper layers, there is a mismatch in the layer location, as the maximum radar layer height was observed higher with respect to the lidar layer. In *Fig. 6.5b*, the lidar linear particle depolarization profile is almost homogeneous, while clear differences are observed for the radar between the CBL and the aerosol lofted layers, indicating of the existence of spherical particles.

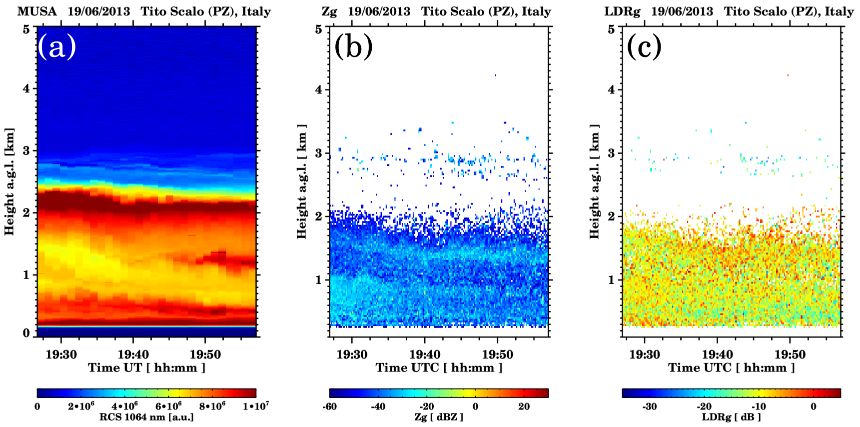

Figure 6.4: *Time-height evolution of (a) the lidar* RCS *at 1064 nm, (b) the cloud radar reflectivity, and (c) the* LDR *for 19 June 2013 between 19:27 and 19:57* UT.

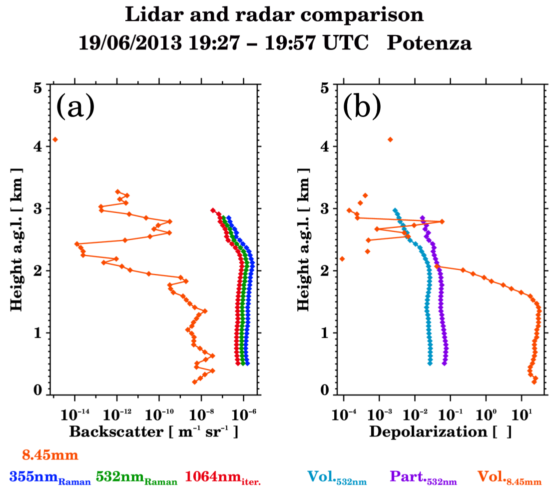

Figure 6.5: *Lidar and radar (a) backscatter coefficient and (b) depolarization ratio comparison for 19 June 2013 between 19:27 and 19:57* UT.

Case 18: 07/03/2014

The stable nocturnal ABL can be observed in the lidar RCS time-height evolution (*Fig. 6.6a*), reaching a height about 1 *km a.g.l.*. The dust layer detected by the lidar is located between 2.8 and 4.9 *km a.g.l.* The radar lofted layer is observed between 2 and 2.8 *km a.g.l.* in the reflectivity plot (*Fig. 6.6b*). Few pixels have LDR values (*Fig. 6.6c*) due to the instrument sensitivity.

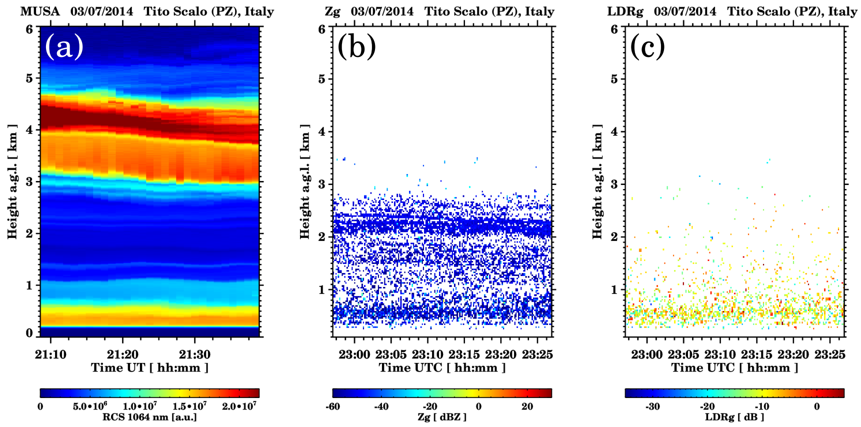

Figure 6.6: *Time-height evolution of (a) the lidar RCS at 1064 nm, (b) the cloud radar reflectivity, and (c) the LDR for 3 July 2014 between 21:09 and 21:39 (lidar) and between 22:57 and 23:27 UT (radar).*

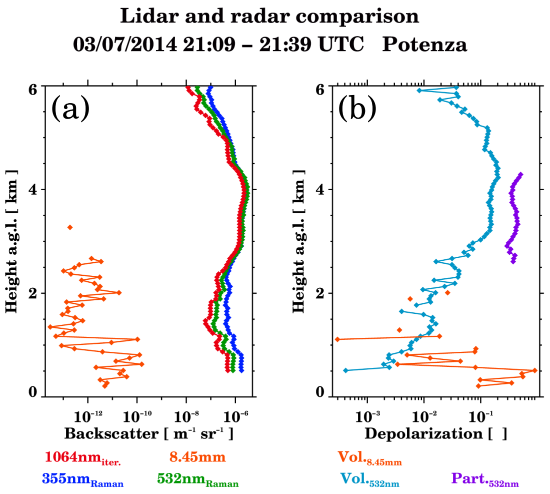

Figure 6.7: *Lidar and radar (a) bakscatter coefficient and (b) depolarization ratio comparison for 3 July 2014 between 21:09 and 21:39 (lidar) and between 22:57 and 23:27 UT (radar).*

The backscatter profiles (*Fig. 6.7a*) report the same discrepancies. As before, the lidar and radar backscatter differ in some orders of magnitude, but in this case the aerosol lofted layer detected by the cloud radar is located below the base of the layer as observed by the lidar. The lidar depolarization profile (*Fig. 6.7b*) reports a high linear particle depolarization for the dust layer (about 30%). The radar LDR profile is similar to the two previous cases for the ABL, while it contains few values related to the lofted layer due to low Signal-to-Noise Ratio (SNR) values in the cross-channel.

6.1.1 All cases comparison

The comparisons highlighted the differences between the lidar and radar profiles, not only in terms of magnitude of the physical parameters examined but also in terms of shape and altitude of the different lofted layers. In Case 2 the lidar and radar lofted layers were collocated, in Case 12 the radar layer was at the top of the lidar one, and in Case 18 at the bottom. However, the comparison has been carried out for the whole dataset in order to identify any existing pattern or correlation between the examined physical parameters. To this end, a series of scatter plots that compare the mean values for each of the layers have been used. The plots are color coded according to the radar target classification.

The height comparison (*Fig. 6.8a*) shows that for most cases the lidar and radar layers coincide in height, from 0.5 to 3.7 *km a.g.l.* The good agreement indicates that the layer contains particles of different sizes: the lidar measures the smaller particles and the radar the bigger ones. In few cases, the layer height observed by the radar was lower, reaching height differences up to 900 *m*. In the cases in which the cloud radar observed aerosols, it is probably an effect of differential settling velocities. In some of the cases, the height of the radar layer is higher (up to a difference of 1 *km*). Most of these cases correspond to cloud radar observations of aerosols.

The backscatter comparison (*Fig. 6.8b*) shows similar values at 1064 *nm* and 8.45 *mm* whether aerosols or insects are observed by the cloud radar, ranging from 10^{-8} to 10^{-5} $m^{-1}sr^{-1}$ and from 10^{-5} to 1 $m^{-1}sr^{-1}$ respectively. However, in two of the cases in which the cloud radar detected aerosols, they have a lower backscatter at 1064 *nm*.

The depolarization comparison (*Fig. 6.9a*) does not present a significant relation between linear particle depolarization and LDR, and no differences are observed depending on the cloud radar detected target.

As in the previous example, the extinction versus backscatter comparison (*Fig. 6.9b*) does not present a relation between the two parameters nor differences depending on the radar target.

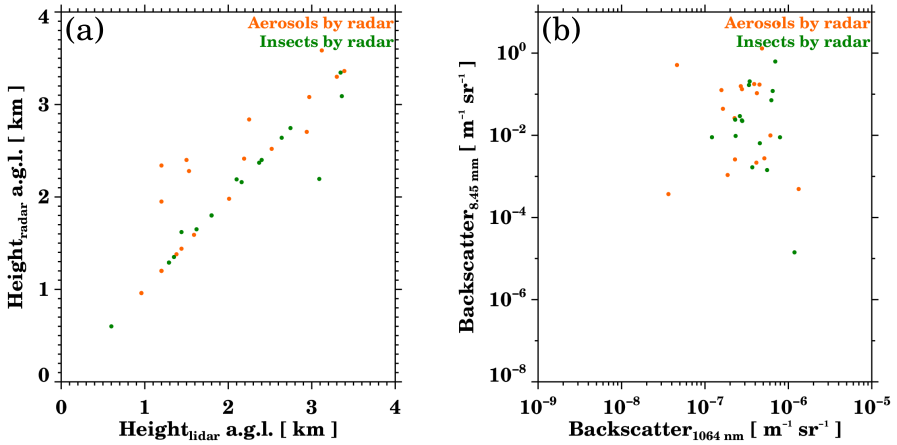

Figure 6.8: *Comparison of (a) the mean lidar and radar layer height and (b) the mean backscatter at 1064 nm and 8.45 mm for the observed lofted layers.*

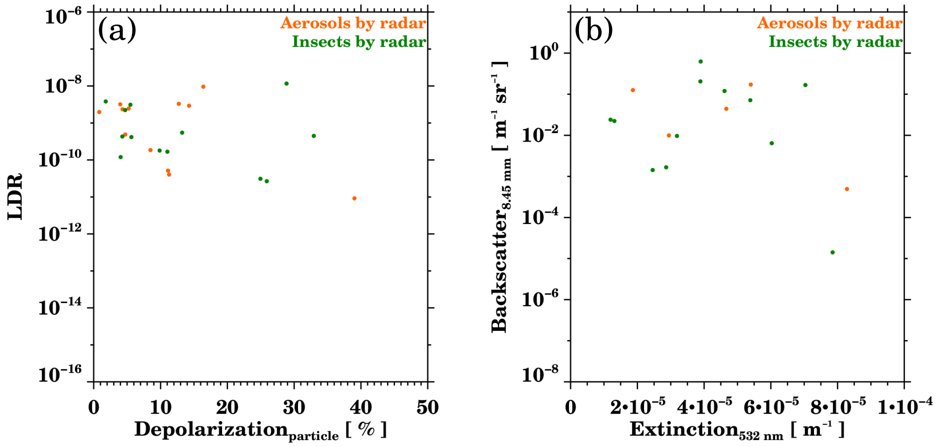

Figure 6.9: *Scatter plots of (a) lidar linear particle depolarization versus radar* LDR *and (b) lidar extinction at 532 nm against the radar backscatter.*

The scatter plots displayed a high degree of correlation only for the location of the layers, whereas the other parameters were uncorrelated. This indicates that the retrieval of the aerosol microphysical properties cannot be performed by using collectively these parameters at all the wavelengths (3 lidar plus 1 radar), as it is usually done in lidar retrievals. In the lidar observations, the measurements at the three wavelengths correspond to the same particles and are, therefore, correlated. Accordingly, the retrieval procedure can make use of the particles spectral dependency for the retrieval. Nevertheless, our findings show no correlation between the two instruments different parameters, which suggests that the signal measured by the lidar and the radar comes from different particles. Therefore, a joint retrieval by using the measurements at the four wavelengths is not possible.

6.2 Microphysical properties retrieval

The inversion of the radar and lidar data for the aerosol microphysical properties retrieval cannot be done jointly because the two instruments observe different parts of the size distribution. Therefore, it is necessary to invert the data for each instrument individually and merge the information to estimate the size distribution from fine to giant mode.

The procedure followed in order to obtain the aerosol effective radius is depicted in *Figure 6.10*. Note that this is the first attempt to observe aerosols in a systematic way with a cloud radar, hence we develop an inversion method to retrieve the aerosol microphysical properties. For the lidar data, the inversion code developed by Veselovskii et al. (2010) was used.

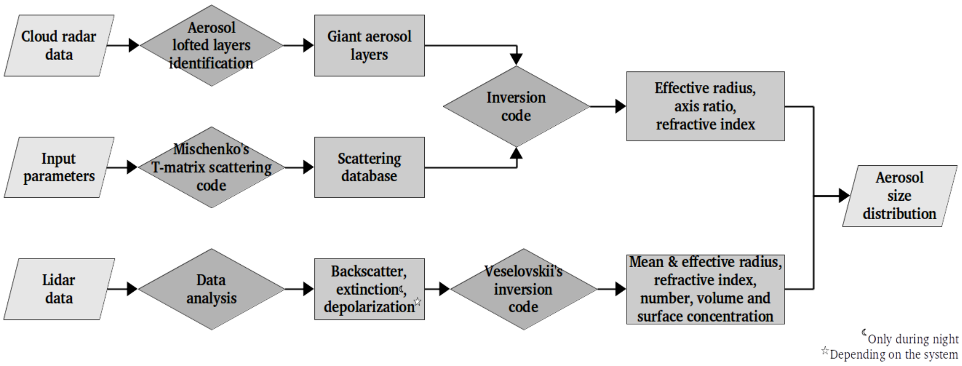

Figure 6.10: *Aerosol microphysical properties and size distribution inversion scheme.*

6.2.1 From radar

The retrieval based on the radar data consists of two parts: the creation of a scattering database and the inversion of the data.

6.2.1.1 Scattering database generation

For the creation of the scattering database, the T-matrix approach was used, since it is one of the most powerful and widely used tools for accurately computing light scattering by nonspherical particles, both single and distributed, based on the direct solving of Maxwell's equations (Mishchenko et al., 1996).

The T-matrix scattering code developed by Mishchenko et al. (1996) has been applied in our retrieval, which computes orientationally-averaged light-scattering characteristics for ensembles of non-spherical axially symmetric particles. The code, here, is solved for spheroids. The main parameter defining them is the axis ratio, which is the ratio between the horizontal and vertical axes. A schematic representation of spheroids with different axis ratio is shown in *Figure 6.11.* The axis ratio for prolate spheroids is lower than 1, while is over 1 for oblate spheroids. When the axis ratio is equal to 1, the particle is a sphere.

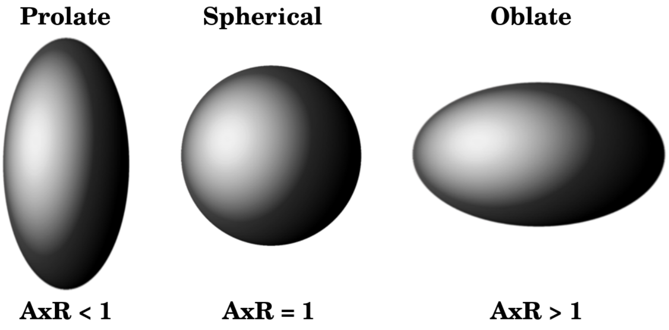

Figure 6.11: *Spheroids with different axis ratios. "AxR" stands for axis ratio.*

The scattering parameters are computed for a really large set of randomly oriented particles at the cloud radar wavelength, considering the combination of a large number of values of effective radius, axis ratio, refractive index and number concentration, resulting in over 3 millions of combinations.

The ranges considered for the listed parameters are reported in *Table 6.1*. The effective radius range is set in the aerosol coarse mode, from 1 μm up to 50 μm. The axis ratio varies between 0.1 and 10, the difference between the two spheroids axis up to a factor of ten. The refractive index is defined according to Adams et al. (1996), who found that volcanic particles at 35.5 *GHz* have a real refractive index of 2.45 ± 0.12 and an imaginary refractive index of 0.43 ± 0.11. Since these values correspond to volcanic particles only, the range is slightly extended: from 2.20 to 2.70 for the real part and from 0.2 to 0.65 for the imaginary part. The number concentration was set to the range 10^{-3} - 10 cm^{-3} according to Lasher-Trapp and Stachnik (2007), who studied the variability of giant and ultragiant aerosols over the eastern Great Lakes region during a campaign with aircraft data. Finally, the scattering angle is set for backscatter and random particle orientation is selected.

Table 6.1: *Input parameters to create the aerosol scattering database at the cloud radar wavelength (8.45 mm). In the axis ratio, "h" and "v" stand for horizontal and vertical axes respectively.*

Parameter	Range
Effective radius [μm]	[1, 50]
Axis ratio (h/v)	[0.1, 10]
Refractive index (real)	[2.20, 2.70]
Refractive index (imaginary)	[0.20, 0.65]
Number concentration [cm^{-3}]	[10^{-3}, 10]
Scattering angle	180°
Orientation	Random

From the Müller matrix, which is the output of Mishchenko's scattering code, we obtain the reflectivity and LDR (Vivekanandan et al., 1991):

$$Z = 10\log_{10}\left\{N\frac{\lambda^4}{1.84\pi}(F_{11}+F_{22})\right\} \tag{6.11}$$

where F_{ii} corresponds to the Müller matrix elements (equation 2.15) and N to the number concentration.

$$LDR = 10\log_{10}\left\{\frac{F_{11}-F_{22}}{F_{11}+F_{22}}\right\} \tag{6.12}$$

Examples of the calculation of reflectivity and LDR are given in *Figures*

6.12 and *6.13*.

Figure 6.12 reports the estimated theoretical reflectivity at 8.45 *mm* for spheroidal particles depending on their size and number concentration. The reflectivity is increasing together with the particle radius and the number concentration, and expectedly the highest increase is associated the particle size (see Equation 6.8). As explained in *Chapter 3*, the radar sensitivity threshold is -55 *dB* at 1 *km*, and therefore reflectivities above this value are highlighted using white horizontal lines. This means that the corresponding particles effective radius and number of particles can be detected by the MIRA36 cloud radar. A particle of 1 μm radius, for example, cannot be measured if its number concentration is below 10 cm^{-3}. A 2 μm radius particle, instead, will be detected if the number concentration is higher than 0.2 cm^{-3}. And finally, all particles with a radius of 5 μm or bigger will be detected if their number concentration is as low as 10^{-3} cm^{-3}.

Figure 6.13 shows the LDR calculated values for a particle of 1 μm radius depending on its axis ratio. An axis ratio of 0.1 means that the horizontal dimension is a tenth of the vertical dimension, while an axis ratio of 10 indicates that the horizontal dimension is ten times bigger than the vertical dimension. The highest LDR value is over -10 *dB*, and corresponds to an axis ratio of 0.2. The lowest values are between -35 and -30 *dB* and correspond to almost spherical particles (axis ratio close to 1). In the event of increase or decrease of the axis ratio, the LDR increases rapidly. It is about -34 *dB* for a particle with an axis ratio of 1.1, -22 *dB* for an axis ratio of 1.5, and -17 *dB* for an axis ratio of 2.

Furthermore, the calculations can be used to understand how the reflectivity and LDR are affected by the complex refractive index. It is an important test since the value selected was the only one found at the radar wavelength and it corresponds to volcanic aerosols, which represent a minority of the cases. The reflectivity and LDR dependence on the complex refractive index is represented in *Fig. 6.14*. The calculations demonstrate that the reflectivity does not depend either on the real (*Fig. 6.14a*) or on the imaginary part (*Fig. 6.14b*) of the selected refractive index (2.20 to 2.70 for the real part and 0.20 to 0.65 for the imaginary part). They also show that the LDR dependency on the selected complex refractive index is very low. For the real part (*Fig. 6.14c*), only a change of 1 *dB* for particles

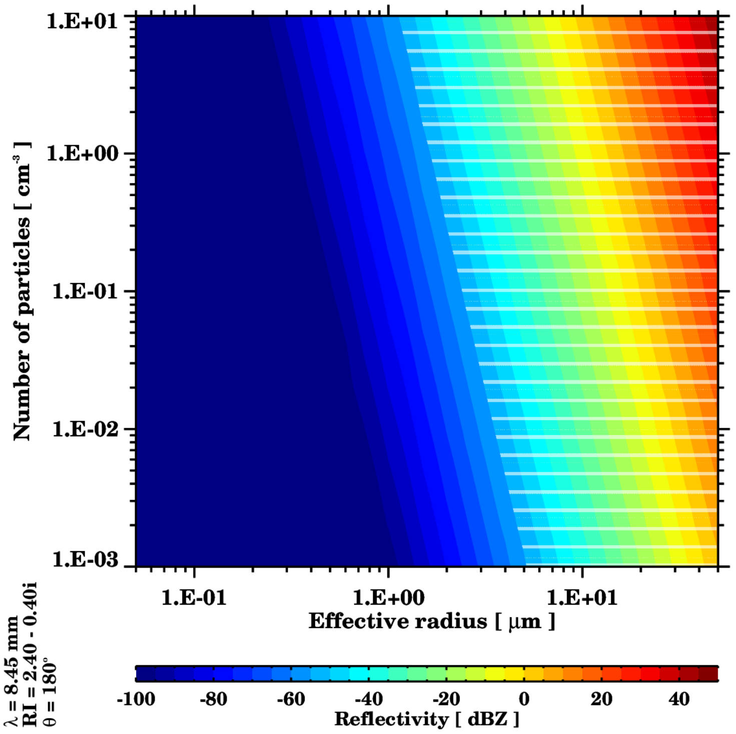

Figure 6.12: *Reflectivity calculations from the output of Mishchenko's T-matrix scattering code depending on the particle effective radius and the number of particles. These values correspond to a wavelength of 8.45 mm, to a complex refractive index of 2.40 - 0.40i, and to a scattering angle of 180°. The white horizontal lines highlight reflectivities over -55 dB, the radar sensitivity threshold at 1 km.*

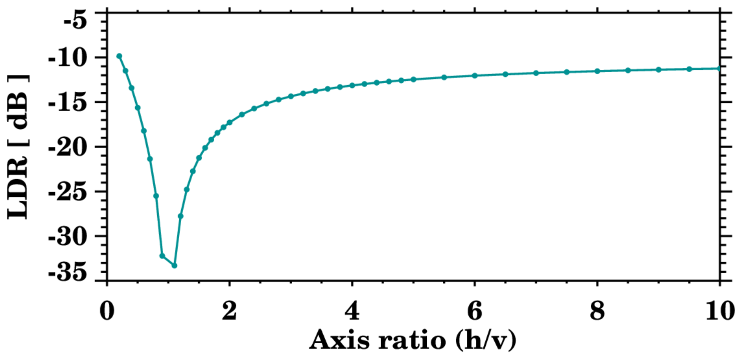

Figure 6.13: *LDR calculations from the output of Mishchenko's T-matrix scattering code depending on the particle effective radius and the number of particles. These values correspond to a particle of radius 1 μm, to a wavelength of 8.45 mm, to a complex refractive index of 2.40 - 0.40i, and to a scattering angle of 180°.*

over 1 μm radius and for refractive indices between 2.8 and 3 is detected. For the imaginary part (*Fig. 6.14d*), a change of 2 dB is detected for particles of of radius around 1 μm and for values of imaginary refractive index over 0.80. In conclusion, these small changes occur outside of the selected complex refractive index ranges, therefore we can say that the effect of this variable on LDR is negligible.

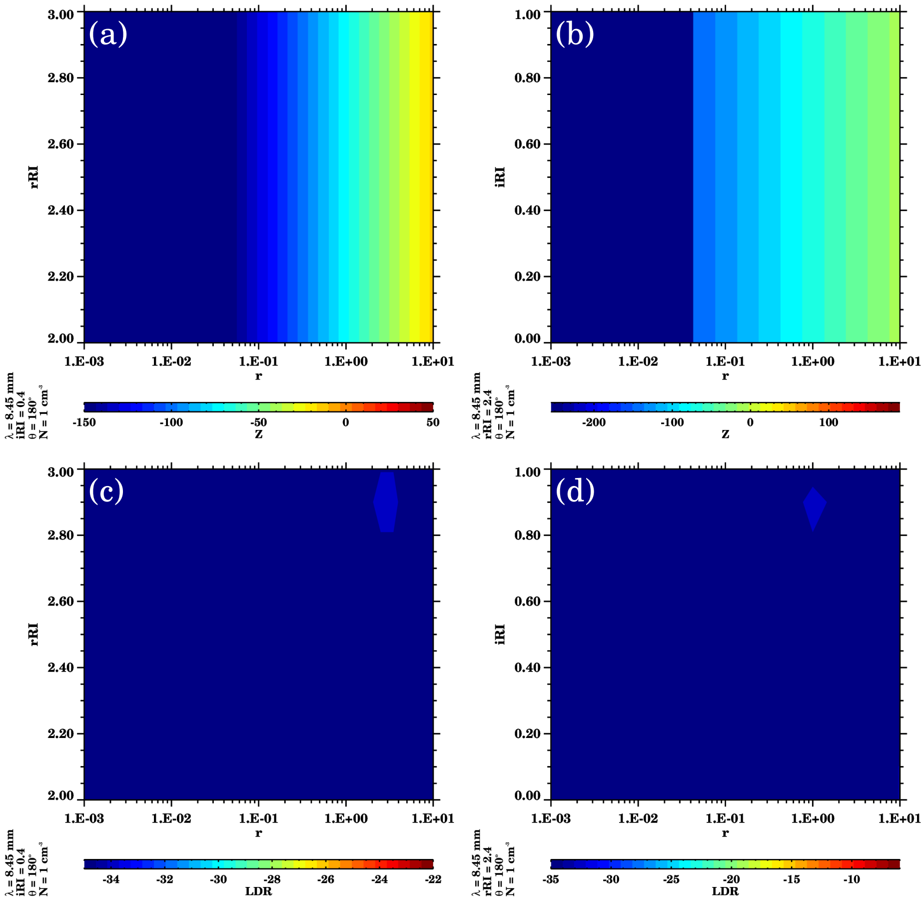

Figure 6.14: *Reflectivity and LDR dependency on the effective radius and the two components of the complex refractive index. (a) Reflectivity dependence on radius and real part of the refractive index. (b) Reflectivity dependence on radius and imaginary part of the refractive index. (c) LDR dependence on radius and real part of the refractive index. (d) LDR dependence on radius and imaginary part of the refractive index. These values correspond to a wavelength of 8.45 mm, to a complex refractive index of 2.40 - 0.40i, to a scattering angle of 180°, and to a number concentration of 1* cm^{-3}.

Summarizing, the scattering database comprises of all the reflectivity and LDR values corresponding to all the possible combinations of effective radius, axis ratio, refractive index and number concentration within the ranges in *Table 6.1*.

6.2.1.2 Inversion algorithm

The microphysical properties are retrieved following the creation of the scattering database. A schematic of the developed methodology can be found in *Fig. 6.15*. The microphysical properties retrieval of an aerosol layer makes use of the observed reflectivity and LDR. Briefly, each pixel is treated individually and, then, the mean properties are calculated considering the associated pixel values.

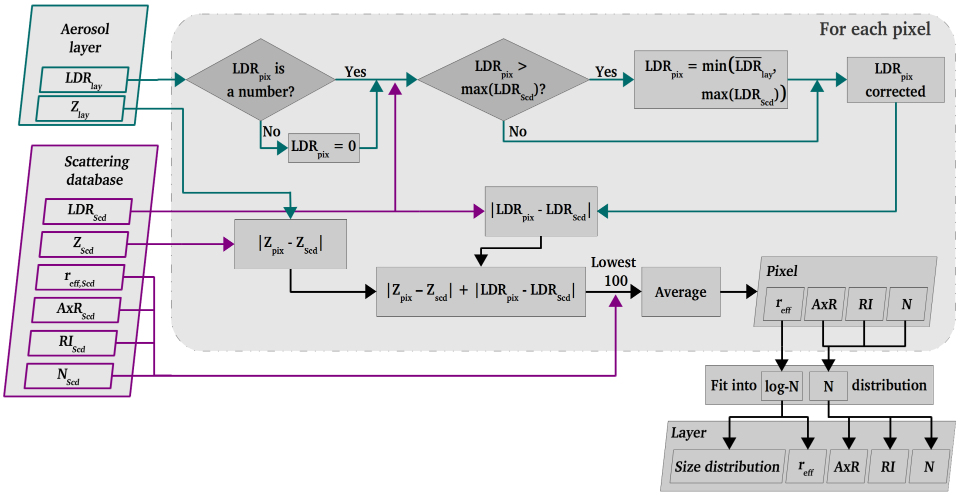

Figure 6.15: *Flowchart of the radar inversion methodology. The symbol "r_{eff}" corresponds to effective radius, "AxR" to axis ratio, "RI" to refractive index, and "N" to number concentration. The subscripts "Lay", "Scd" and "pix" correspond to layer, scattering database and pixel respectively.*

In the first step, it is checked if the pixel LDR value is a number, indicating that the LDR is above the sensitivity threshold. If not, the pixel LDR value is set to 0.

In the second step, the pixel LDR value is reset in case it is higher than the maximum LDR value estimated in the scattering database (~ -10 *dB*). Without this correction, in many cases it would not be possible to find a solution in the following step, providing a less accurate result. The pixel

LDR value, initially, was corrected with the maximum LDR value estimated in the scattering database. However, considering the reflectivity and LDR layer discrepancies, we found stable solutions when resetting the pixel LDR value to the layer mean LDR, if this value is lower than the maximum estimated values from the scattering database. In any other case, we correct with the maximum value in the scattering database. On account of this selection, *Table 6.2* reports the reflectivity and LDR discrepancies depending on the value to which the high LDR values were set, depicting that the discrepancies are always lower when the selected criterion is invoked.

Table 6.2: *Reflectivity and LDR discrepancy for Case 12, depending on the correction applied to LDR values higher than the maximum scattering database LDR value. In parenthesis, the discrepancy values expressed in dB.*

Variable	Range of application	Discrepancies when high LDR set to: min($\overline{LDR}_{lay}$, max(LDR_{Scd}))	max(LDR_{Scd})
Z	All points	$3.557\ 10^{-5}$ (-44.5)	$3.872\ 10^{-5}$ (-44.1)
	LDR > LDR_{max}	$3.417\ 10^{-5}$ (-44.7)	$9.935\ 10^{-5}$ (-40.0)
LDR	All points	$4.606\ 10^{-5}$ (-43.4)	$5.785\ 10^{-5}$ (-42.4)
	LDR > LDR_{max}	$5.296\ 10^{-5}$ (-42.8)	$2.966\ 10^{-4}$ (-35.3)

After the pixel LDR correction, where needed, the absolute differences between the reflectivity pixel value and the database reflectivity values and between the LDR pixel value and the database LDR values are computed and added. Then, the particle properties corresponding to the lowest hundred values (or less, if the absolute difference is not below 1 *dB*) are averaged to obtain the mean pixel effective radius, axis ratio, complex refractive index and number concentration.

Upon retrieving the mean pixel effective radii, we fit them to a mono-modal log-normal distribution to obtain the layer aerosol size distribution and its effective radius. Then, the pixel axis ratios, complex refractive indices and number concentrations are fit to a normal distribution, which provides a mean layer value and a standard deviation for each parameter.

In the following, the performance of the described method in terms of discrepancy for reflectivity and LDR is shown for Case 12 in *Table 6.3* and in *Figures 6.16* and *6.17*.

Table 6.3 includes the reflectivity and LDR discrepancy (difference between the measured and retrieved values) for different scenarios. Considering all the layer points, the difference is below 5 10^{-5} for both reflectivity and LDR. The lowest discrepancies correspond to spherical or almost spherical particles (LDR = 0), when the LDR is equal to 0. This can be explained by the null or very low LDR differences. The highest discrepancies correspond to the pixels in which the LDR values were not corrected ($0 <$ LDR $\leq$ LDR$_{max}$), which is associated with larger pixel LDR variability. Considering all the pixels with LDR equal to zero and the not corrected (LDR $\leq$ LDR$_{max}$), the discrepancies are very close to those considering the whole layer, which is also the case for the pixels in which the LDR was corrected for being too high (LDR $>$ LDR$_{max}$).

Table 6.3: *Reflectivity and LDR discrepancy for Case 12 (19 June 2013). In parenthesis, the discrepancy values expressed in dB.*

Range of application	Discrepancies	
	Z	LDR
All points	3.557 10^{-5} (-44.5)	4.606 10^{-5} (-43.4)
LDR = 0	3.966 10^{-6} (-54.0)	0.0 (–)
$0 <$ LDR $\leq$ LDR$_{max}$	9.709 10^{-5} (-40.1)	1.344 10^{-4} (-38.7)
LDR $\leq$ LDR$_{max}$	3.564 10^{-5} (-44.5)	4.571 10^{-5} (-43.4)
LDR $>$ LDR$_{max}$	3.417 10^{-5} (-44.7)	5.296 10^{-5} (-42.8)

In *Figure 6.16* the calculated reflectivity (blue line) reproduces well the measured radar reflectivity (purple line), suggesting a robust performance of the methodology. The yellow line corresponds to the pixels for which LDR is equal to 0. The proportion of pixels for which this condition is met is increasing with lower reflectivity values due to the instrument sensitivity. The turquoise line corresponds to the pixels where the LDR was not corrected, since the measured value was below the threshold of the maximum scattering database LDR value. This line presents an inversed behaviour in respect to the previous category. The last two categories together are presented in green, and follow closely the original values. The observed discrepancy (between blue and green lines) can be easily attributed to the LDR pixel values that were corrected for high values (red line).

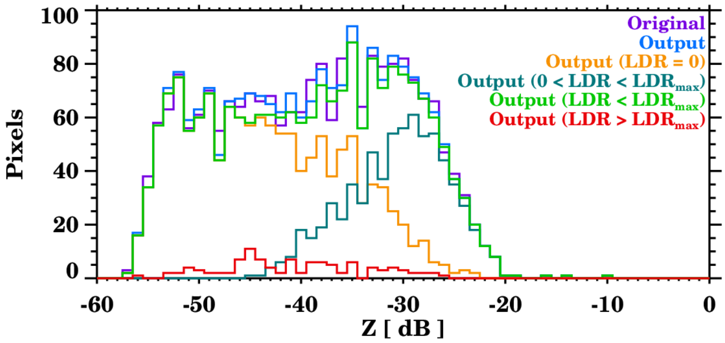

Figure 6.16: *Reflectivity performance for Case 12 (19 June 2013). "Original" corresponds to the cloud radar measurements, and "Output" to the retrieval. In parenthesis, different subsets of pixels are presented according to their* LDR.

The agreement, once more, is satisfactory regarding the performance of LDR (*Fig. 6.17*). The values measured by the radar are depicted with the purple line, spanning from -30 to 0 *dB*. The LDR values equal to 0 are not presented in this plot, and the LDR values over the scattering database maximum were, in this case, assigned to the mean LDR of the layer (~ -13 *dB*). The corrected LDR is presented in dark blue. The retrieval including all the points (light blue) is very close to the used input (corrected). The output for LDR points without correction (green line) along with the corrected pixels (red line) are almost the same as the input used.

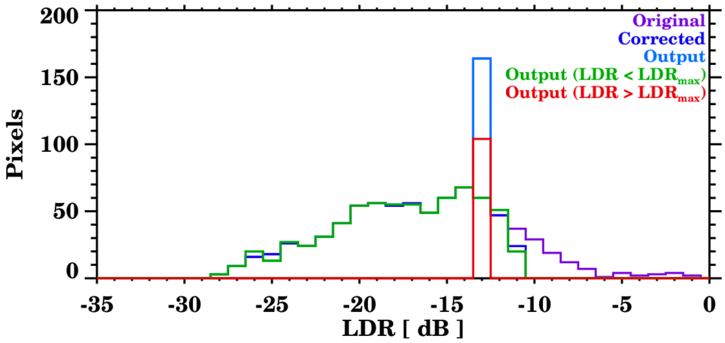

Figure 6.17: LDR *performance for Case 12 (19 June 2013). "Original" corresponds to the cloud radar measurements, and "Output" to the retrieval. In parenthesis, different subsets of pixels are presented according to their* LDR.

The described method was applied to all the cloud radar aerosol lofted layers observations. The size ranges and refractive indices considered to generate the scattering database (*Tab. 6.1*) do not correspond to insects, and therefore the results are associated to aerosols only.

The performance of the method in terms of discrepancy is presented in *Table 6.4* for reflectivity and LDR. The discrepancy averaged for all the cases is of 5.30 10^{-5} for the reflectivity and of 1.21 10^{-4} for the LDR. The discrepancy is 1 order of magnitude higher for the LDR, which can be attributed to the corrections to the pixels that had measured values over the maximum value in the scattering database. The worst performance has discrepancies 2 orders of magnitude higher for both parameters (5.43 10^{-3} and 1.12 10^{-2} respectively), but the values are acceptable. The best performance for the reflectivity has a discrepancy of 2.65 10^{-7}, and for the LDR of 1.08 10^{-7}.

Table 6.4: *Reflectivity and LDR performance for all the aerosol cases. In parenthesis, the discrepancy values expressed in dB.*

Performance	Z	LDR
Best	2.65 10^{-7} (-65.8)	1.08 10^{-7} (-69.7)
Mean	5.30 10^{-5} (-42.8)	1.21 10^{-4} (-39.1)
Worst	5.43 10^{-3} (-22.7)	1.12 10^{-2} (-19.5)

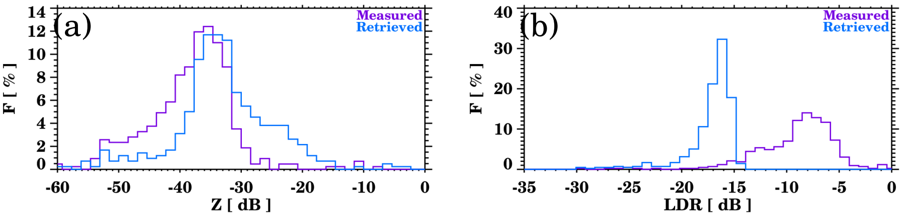

Figure 6.18: *Frequency distributions of the original and retrieved (a) reflectivity and (b) LDR.*

Figure 6.18 shows the frequency distributions of the mean reflectivity and LDR for all the aerosol layers as measured by the radar (purple line) and as retrieved by our method (blue line). The reflectivity plot (*Fig. 6.18a*) shows a fair agreement between the two distributions. The most frequent distributions (between -40 and -30 *dB*) coincide for the measured and retrieved reflectivity. The created inversion method, though, generally overestimates reflectivities over -30 *dB* and underestimates them below -40 *dB*. The reason for these discrepancies is probably due to the LDR pixels corrections done. In the LDR plot (*Fig. 6.18b*), the effect of the correction of pixel values over the maximum LDR value in the scattering database is obvious: the frequency distribution is shifted towards lower LDR values for the retrieval.

The frequency distributions of the retrieved effective radius, size parameter, number concentration, axis ratio and refractive index are shown in *Figures 6.19*, *6.20* and *6.21*.

The effective radius (*Fig. 6.19a*) ranges between 1.5 and 6 μm and has a bimodal distribution. The first maximum is slightly below 3 μm and the second slightly above 4 μm. The corresponding size parameter (*Fig. 6.19b*) is between 10^{-3} and 2 10^{-2}, and agrees with the Rayleigh regime assumption embedded in the retrieval method.

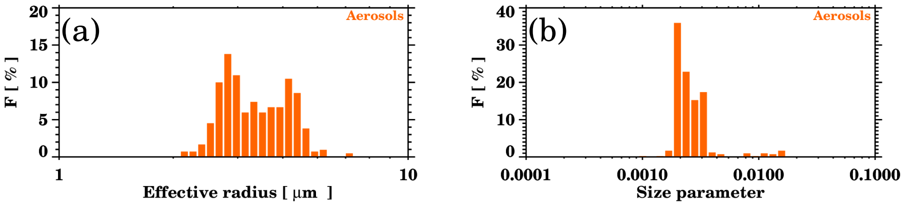

Figure 6.19: *Frequency distributions of the retrieved (a) effective radius, (b) size parameter.*

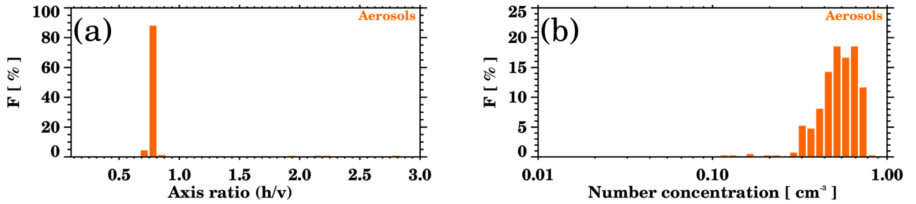

Figure 6.20: *Frequency distributions of the (a) axis ratio (horizontal / vertical axis) and (b) number concentration.*

The axis ratio (horizontal/vertical axis) frequency distribution (*Fig. 6.20a*) indicates that more than 90% of the particles are prolate, with axis ratios between 0.7 and 0.8. A small portion of the aerosols are oblate, with axis ratios around 2, and almost none are spherical. These findings are consistent with our hypothesis of giant particles. They comprise mainly of dust, pollen, and volcanic; hence irregular shaped aerosol types. The number concentration (*Fig. 6.20b*) is found to be between 0.10 and 1 cm^{-3}, with maximum values in the region 0.4 - 0.7 cm^{-3}.

The real part of the refractive index (*Fig. 6.21a*) oscillates between 2.43 and 2.47, while its imaginary part (*Fig. 6.21b*) fluctuates around 0.4, suggesting that the observed particles have a lower single scattering albedo than the volcanic particles studied by Adams et al. (1996).

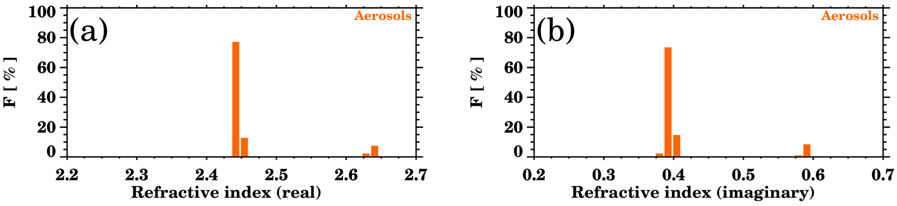

Figure 6.21: *Frequency distributions of the retrieved (a) real and (b) imaginary part of the refractive index.*

Finally, the aerosol geometric radius is calculated by using equation 1.5 from *Chapter 1*. *Fig. 6.22* shows the frequency distribution of this parameter. The aerosols radius extends between 1 and 10 μm, and the particles are most likely to have radii in the range 1 - 2 μm. Typically, the frequency decreases with aerosol size. This suggests that the smaller aerosols reach the observational site more frequently compared to bigger ones, as one would expect according to their respective settling velocities.

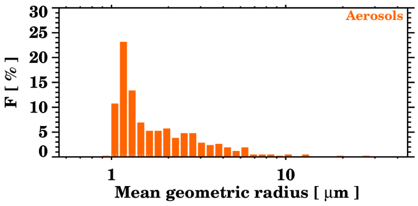

Figure 6.22: *Frequency distribution of the retrieved mean geometric radius.*

6.2.2 From lidar

The retrieval of microphysical properties for the aerosol layers observed with lidar is done using the algorithm introduced by Veselovskii et al. (2004). The model uses as input the profiles of multi-wavelength aerosol extensive optical properties and delivers the aerosol size distribution, the complex refractive index and number, surface and volume concentrations.

The algorithm retrieval consists in the comparison between a precalculated optical dataset and the optical data from the lidar. The solutions are found by minimizing the discrepancy between these two. This is based on the dependence of the complex refractive index on the intensive optical properties: the backscatter determines the scattering (real part, m_r) and the extinction the absorption (imaginary part, m_i).

To perform a retrieval, first, it is necessary to constrain the range of the solutions. The constraints used for this study can be found in *Table 6.5*.

Table 6.5: *Input parameters for the retrieval of the lidar microphysical properties.*

Parameter	Range
Minimum radius [μm]	[0.05, 0.2]
Maximum radius [μm]	[0.55, 10]
Refractive index (real)	[1.35, 1.68]
Refractive index (imaginary)	[0.0005, 0.05]
Scattering angle	180°
Particle shape	Spheres & spheroids
Distribution	Bimodal

The input variables used in this study correspond to the three aerosol backscatter coefficients (at 355, 532 and 1064 *nm*) and the two aerosol extinction coefficients (at 355 and 532 *nm*) obtained from the Raman lidar measurements. The mean layer properties are calculated and further processed by the model. The retrieved microphysical properties correspond to the average of all the solutions that differ less than 1% from the input parameters.

The inversion code was applied to all the lidar measurements in which the three backscatter coefficients and the two extinction coefficients were available for the aerosol lofted layer. From the 25 night-time lidar cases, the inversion of the microphysical properties could be performed for 11 cases. As previously, they are classified according to the cloud radar observed target: 5 correspond to aerosols and 6 to insects observations.

Figure 6.23 reports the number, surface and volume distribution for each individual case (a, c and e) and the mean distribution with respect to all the cases depending on the observed radar target (b, d and f).

In *Figure 6.23a*, the number distribution for each case shows that most of the particles fall in the size range 0.06 - 1 μm. The number concentration reaches up to 670 $\mu m\ cm^{-3}$, but for most cases is lower than 150 $\mu m\ cm^{-3}$. In *Figure 6.23c*, the surface distributions reveals the existence of a minor lobe in the region 1-10 μm. This indicates that even if in low number concentration, some coarse particles are detected by the lidar. The surface concentration is, in general, lower than 50 $\mu m^2\ cm^{-3}$, but in some cases reaches up to 100 $\mu m^2\ cm^{-3}$. The volume concentration in *Figure 6.23e* yields a remarkable feature: not all the distributions are bimodal. Some distributions have three modes, and its corresponding radii ranges are: from 0.1 to 0.3 μm, between 0.3 and 1 μm and from 1 to 6 μm. No differences in the distributions of all the individual cases could be observed depending on the cloud radar target. In the averaged distributions, though, there are some discrepancies.

Figure 6.23b shows the number distribution for all the lidar aerosol cases averaged depending on the cloud radar detected target. In this case, in fact, the distributions are slightly different: the aerosol radii when insects were observed by the cloud radar (between 0.06 and 0.13 μm) is lower than when also aerosols were observed (between 0.09 and 0.14 μm). The number concentration in both cases, though, is similar. *Figure 6.23d* presents the surface distribution in the same way. For the cloud radar insects observations, two modes are observed, the second from 0.3 to 1 μm, while for radar aerosols observations there is one main mode between 0.10 and 1 μm. The surface concentration is slightly higher for the aerosol cases. *Figure 6.23f* reports the volume distribution, which has three modes both for cloud radar aerosols and insects. In this case, the distributions are relatively closer than before, and also the volume concentration is quite similar.

In conclusion, in the studied cases it was possible to observe particles with lidar with radii between 0.1 and 6 μm, with mean radii below 1 μm. Some differences in the number, surface and volume distributions were detected according to the cloud radar observed target, but they do not seem to be significant given the high standard deviation.

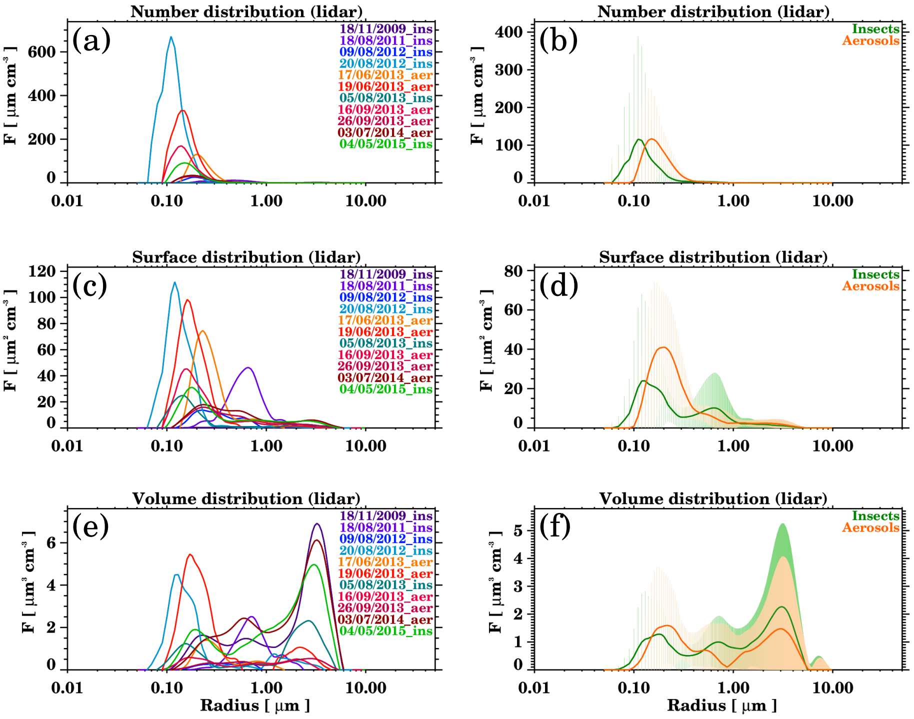

Figure 6.23: *Number, surface and volume distribution for all the night-time lidar cases, using Veselevskii's algorithm. In the left panels (a, c and e), the distributions are plotted for each of the cases, and the legend indicates the date and the target detected by the cloud radar ("aer" stands for aerosols and "ins" for insects. In the right panels (b, d and f), the distributions correspond to averaging all the individual distributions depending on the target observed by the cloud radar. The vertical lines correspond to the standard deviation.*

6.2.3 Combination

By combining the aerosol size distribution information from the lidar and the radar, it is possible to merge and subsequently enhance the range of the aerosol size distribution. The aerosols detected by the radar have radii between 1 and 10 μm, whereas the particles observed by the lidar are mainly between 0.1 and 1 μm, sometimes detecting particles up to 6 μm.

Cases 12 and 18 are used to illustrate the advantages of coupling lidar and radar data. The microphysical properties for Case 2 could not be retrieved from the lidar measurements, owing to background contamination during day-time conditions.

Case 12: 19/06/2013

Smoke particles were observed on 19 June 2013. The panels in *Figure 6.24* show the number, surface and volume distribution respectively, combining the lidar and radar observations.

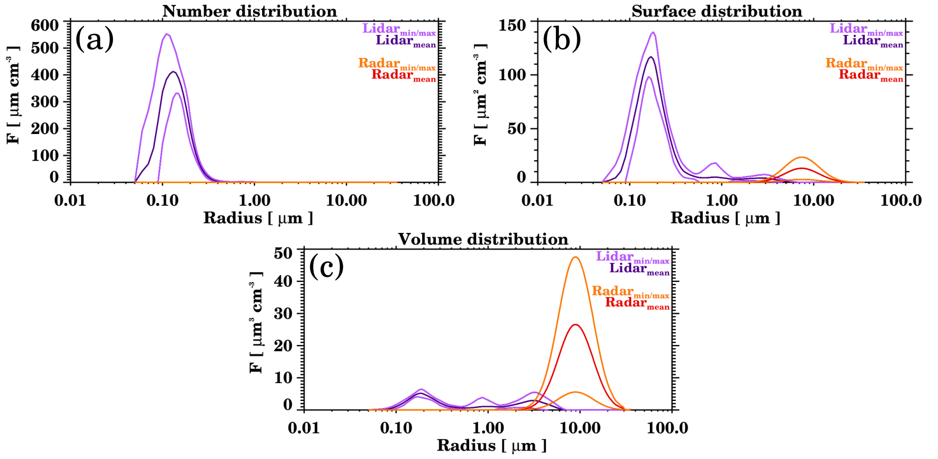

Figure 6.24: *Case 12: (a) number, (b) surface and (c) volume size distribution for the layer observed on 19 June 2013 from 19:27 to 19:57* UT.

The number distribution (*Fig. 6.24a*) shows that the number of particles below 0.4 μm is predominant. The number concentration of particles with radii over 1 μm is as low as not to be visible in the graph. In the surface distribution graph (*Fig. 6.24b*), particles below 0.4 μm still predominate, however coarser particles are manifested in 3 secondary maxima. The first and second secondary maxima are seen by the lidar (~ 1 μm and ~ 3 μm) and the third by the radar (~ 7 μm). The volume distribution (*Fig. 6.24c*) shows an inverted behaviour if compared with the surface distribution. The lidar and radar curves overlap for aerosols between 2 and 6 μm radius approximately. This indicates that the lidar detected a small fraction of the coarser particles seen by radar, with maximum centered at ~ 9 μm.

This case is an example of how to get an enlarged aerosol size distribution by combining Raman lidar and cloud radar information. The Raman lidar can be used to retrieve the size distribution for aerosols in the Aitken and in the accumulation mode, as well as for a small part of the coarse mode. The cloud radar can be used to retrieve the size distribution for coarse mode aerosols.

Table 6.6: *Case 12: aerosol microphysical properties retrieved from the radar and lidar measurements for the smoke case on 19 June 2013. In the axis ratio, "h" and "v" stand for horizontal and vertical axis respectively.*

Parameter	Radar	Lidar
Effective radius [μm]	5.20 ± 2.55	0.97 ± 0.22
Mean radius [μm]	3.32 ± 0.11	0.22 ± 0.034
Number concentration [cm^{-3}]	0.77 ± 0.61	58 ± 25
Refractive index (real)	2.45 ± 0.02	1.40 ± 0.09
Refractive index (imaginary)	0.41 ± 0.02	0.006 ± 0.1
Spheroid fraction [%]	–	0
Axis ratio (h/v)	0.77 ± 0.04	–

The mean microphysical properties retrieved from the radar and lidar measurements for this case can be found in *Table 6.6*. As already discussed, the effective and mean radius are larger for the aerosols detected by the radar and the number concentration is much higher for the lidar detected particles. The complex refractive index is very different for both instruments. The different input values for the two inversion methods bias the retrieved mean values, since this parameter depends both on the particle type and the wavelength. The spheroid fraction for the lidar particles is equal to 0, while the axis ratio for the radar shows that the particles were prolate. This information is not directly comparable, but it indicates that the lidar observed spherical particles and the radar aspherical ones.

Case 18: 03/07/2014

Pure dust particles, as classified by the lidar, were observed on 3 July 2014. Number, surface and volume distributions are shown in *Figure 6.25*.

The number distribution (*Fig. 6.25a*) shows that the number of particles below 1 μm is predominant, and no contribution from larger particles is observed. The surface distribution (*Fig. 6.25b*) for aerosols detected by the lidar has two modes: a main mode from 0.07 to 2 μm radius, and a smaller one from 2 to 8 μm. The surface distribution for the aerosols, as measured by the radar, spans from 1 to 12 μm approximately. Therefore, there is an overlap between the aerosol radii measured by the two instruments. In the volume distribution (*Fig. 6.25c*) this overlap between the coarse aerosols observed by lidar and by radar is even more evident. As in the previous case, the combined information is able to provide an enlarged aerosol size distribution.

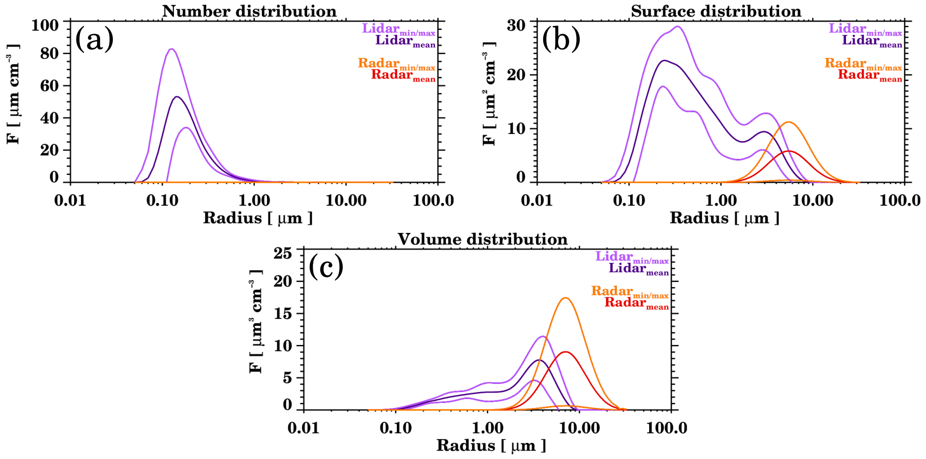

Figure 6.25: *Case 18: (a) number, (b) surface and (c) volume size distribution for the layer observed with the lidar between 2.0 and 2.5 km a.g.l. on 3 July 2014 from 21:09 and 21:39 (lidar) and between 22:57 and 23:27* UT *(radar).*

The mean microphysical properties retrieved from the radar and lidar measurements for this case are given in *Table 6.7*. The effective and mean radius is larger for the aerosols detected by the radar and the number concentration is one order of magnitude higher for the lidar. The spheroid fraction as retrieved by lidar indicates spherical particles; whereas radar retrieved axis ratio suggests the existence of non-spherical particles.

Table 6.7: *Case 18: aerosol microphysical properties retrieved from the radar and lidar measurements for the dust case on 3 July 2014. In the axis ratio, "h" and "v" stand for horizontal and vertical axis respectively.*

Parameter	Radar	Lidar
Effective radius [μm]	3.33 ± 0.65	0.97 ± 0.22
Mean radius [μm]	0.66 ± 0.13	0.22 ± 0.034
Number concentration [cm^{-3}]	0.71 ± 0.66	58 ± 25
Refractive index (real)	2.45 ± 0.02	1.40 ± 0.09
Refractive index (imaginary)	0.40 ± 0.02	0.006 ± 0.1
Spheroid fraction [%]	–	0
Axis ratio (h/v)	0.79 ± 0.04	–

In conclusion, the combination of the aerosol microphysical properties retrieved individually from the lidar and from the radar measurements provides an enlarged aerosol size distribution: approximately from 60 nm to 15 μm.

7

Giant aerosol effects

The ultimate goal of observing giant aerosols is to study their effects in order to get a better understanding of the processes that they are involved in and their importance for meteorology and climate. To this purpose, observations of ancillary ground-based instruments are compared for giant aerosol observations by the cloud radar and *control measurements* (days in which giant aerosols were not observed). The considered ancillary observations that have been considered are the Aerosol Optical Depth (AOD), the Ångström exponent, the Cloud Optical Depth (COD), the Ice Water Content (IWC), the Liquid Water Path (LWP) and the precipitation.

The selection of the giant aerosols and the not giant aerosols (control) observations is based on the study of Koren et al. (2012), who characterized the aerosol induced intensification of rain from the tropics to the mid-latitudes by using rain rates from the Tropical Rainfall Measuring Mission (TRMM) and meteorological information from the Global Data Assimilation System (GDAS). The findings of this study were that the increases in aerosol abundance are associated with the local intensification of rain rates detected by the TRMM.

The diurnal cycle is an important factor in determining convective activity, clouds and rain. For this reason, it needs to be taken into account to study the effects on clouds and precipitation. Therefore, a time period of the day needs to be selected and used for all the cases (giant and not giant aerosol observations). The time interval used is from 13:00 to 14:00 local time, selected on the basis of Koren et al. (2012), who set the time for his study at 13:30 local time.

The giant observations are screened using the following criterion. Measurements are selected if they were performed less than 4 hours distant from the predefined time interval. From the initial 446 cases of giant aerosol observations, 174 days passed this specific filter.

The selection of control cases (not giant aerosol observations) is based on the size distribution retrievals from AERONET. Therefore, days with effective radius of the coarse mode lower than 2.5 μm - definition of giant aerosols - are flagged as control cases. The AERONET size distribution retrievals were available for 212 of the 2107 considered days (March 2009 - June 2015). The screening filter was invoked for 173 cases.

The meteorological situation is assessed by sorting the data into cases with different pressure vertical velocities (ω) of the upper atmosphere (500 - 350 hPa). Negative pressure vertical velocities indicate a net upward air motion, related with more developed clouds and higher rain rates. Positive ω indicates subsidence and therefore less developed clouds. This screening criterion was used by Koren et al. (2012), who separated the data in three groups according to ω at 400 hPa: $\omega < -0.04$ $Pa\ s^{-1}$, -0.04 $Pa\ s^{-1} < \omega < 0.04$ $Pa\ s^{-1}$, and $\omega < 0.04$ $Pa\ s^{-1}$. In this study, the pressure vertical velocities used are the ones from the ECMWF model. The frequency distribution of the pressure vertical velocities from March 2009 to June 2015 in our site is shown in *Figure 7.1*. We found much lower ω values than in Koren's study: no values are below -0.04 $Pa\ s^{-1}$ or above 0.04 $Pa\ s^{-1}$. This difference can be attributed to the latitudinal differences between studies. According to the observed values, here, three stability levels have been defined:

- Stability 1: $\omega \leq -0.001$ $Pa\ s^{-1}$
- Stability 2: -0.01 < $\omega \leq -0.001$ $Pa\ s^{-1}$
- Stability 3: $\omega > 0.001$ $Pa\ s^{-1}$

The pressure vertical velocity was available for 150 of the 174 giant aerosol observation cases and for 159 of the 173 initial not giant aerosol observation cases. Therefore, our dataset consists of 150 days of giant aerosol observations and 159 days of not giant aerosol observations. *Table 7.1* reports the initial number of cases, the study cases (for which ω

is available), and the cases corresponding to each atmospheric stability category.

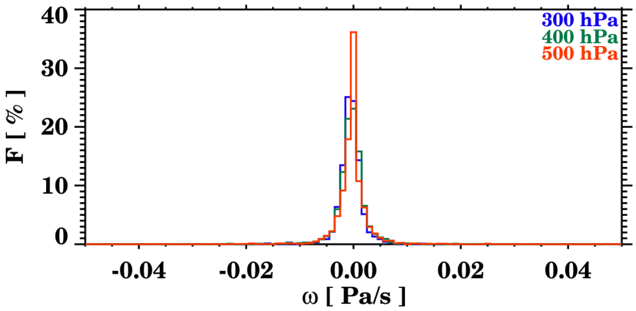

Figure 7.1: *Frequency distribution of the pressure vertical velocities at CIAO from March 2009 to June 2015 at three pressure levels: 300, 400 and 500 hPa.*

Table 7.1: *Number of giant and not giant cases for the initial conditions (giant cases within the time interval defined and not giant cases with a coarse mode effective radius < 2.5 μm) and with available pressure vertical velocity (ω) data. The stability types defined are: 1 ($\omega \leq -0.001$ $Pa\ s^{-1}$), 2 (-0.01 < $\omega \leq -0.001$ $Pa\ s^{-1}$) and 3 ($\omega > 0.001$ $Pa\ s^{-1}$).*

Parameter	Stability condition	Giant	Not giant
Initial cases	None	174	173
Stability (ω)	All	150	159
	1	33	47
	2	88	70
	3	29	42

7.1 Aerosol Optical Depth and Ångström exponent

The sun photometer measures the AOD and the Ångström exponent at different wavelengths. The AOD is a measure of radiation extinction due to both absorption and scattering of aerosols. The Ångström exponent, in this case referred to the AOD columnar measurements, indicates the AOD dependence on the wavelength, and is inversely related to the average size of the aerosol particles. It is calculated as:

$$å_{AOD} = -\frac{log\frac{\tau_{\lambda_1}}{\tau_{\lambda_2}}}{log\frac{\lambda_1}{\lambda_2}} \tag{7.1}$$

where τ is the optical depth and λ_1 and λ_2 correspond to the two different wavelengths. The AOD and the Ångström exponent are standard products of AERONET.

The annual evolution of AOD and Ångström exponent is presented in *Fig. 7.2* together with the normalized frequency distribution of giant aerosol cases. AERONET observations are columnar and cover a broad range of the aerosol size spectrum. In *Figure 7.2a*, the AOD curves and the distribution of the giant aerosol observations yield a good agreement: the highest AOD values are observed during the months in which more giant aerosol cases occur. The enhanced AOD values during spring and summer agree with the annual cycle of dust outbreaks (Mona et al., 2009, 2014) suggesting the prevalence of coarse mode aerosols over Potenza. The AOD evolution that should be closer to the giant aerosol observations is the one corresponding to the bigger wavelength, at 1020 *nm*. *Fig. 7.2b* shows the evolution of the aerosols size through the year: smaller during winter and bigger during summer.

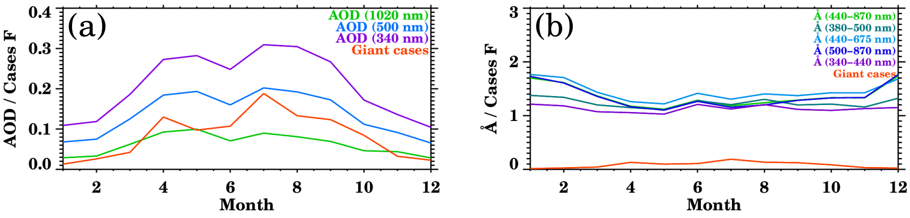

Figure 7.2: *Frequency distribution of giant aerosols cases (orange line) as observed with the cloud radar together with two AERONET measured variables: (a) AOD at 340, 500 and 1020 nm and (b) Ångström exponent for different pairs of wavelengths.*

Next, the frequency distribution of AOD for cases of giant and not giant aerosol observations for two wavelengths is given in *Figure 7.3*. The same graphs are plotted also for the Ångström exponent, as shown in *Figure 7.4*. No major differences are observed for none of the variables at the different plotted wavelengths.

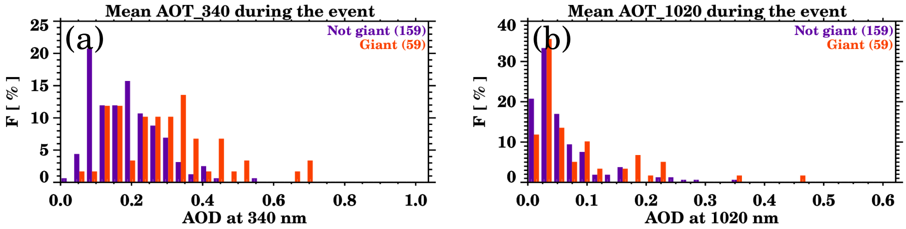

Figure 7.3: *Frequency distributions of* AOD *at (a) 340 and (b) 1020 nm for giant and not giant events. The numbers in parenthesis indicate the number of cases available for each category.*

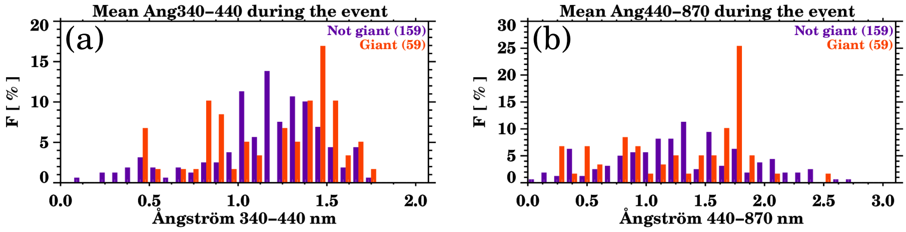

Figure 7.4: *Frequency distributions of the Ångström exponent for the pairs of wavelength: 340-440 nm and 440-870 nm. The numbers in parenthesis indicate the number of cases available for each category.*

7.2 Cloud Optical Depth

The COD is a measure of radiation extinction due to absorption or scattering by clouds. In principle, the bigger the aerosols, the lower the initial concentration of cloud droplets and the shortest the lifetime of clouds. Hence, higher COD values are expected after giant aerosols are observed.

The COD values used in this section correspond to the AERONET retrievals in cloud mode, that were introduced in *Section 3.3.1.3*.

Figure 7.5 reports the frequency distribution of COD for giant and not giant aerosols 1 *hour* and 6 *hours* after the observations. The spurious character of the distributions and the data paucity (33 not giant and 30 giant aerosol observations) do not allow to extract any safe remarks.

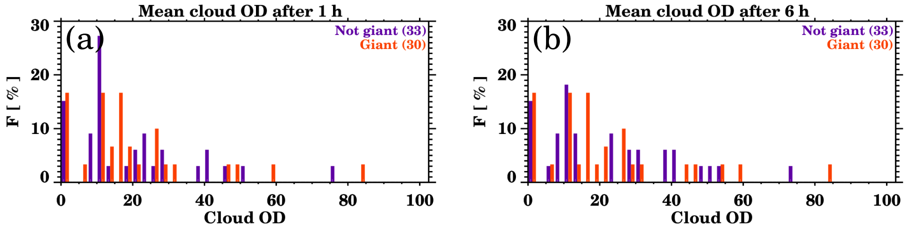

Figure 7.5: *Frequency distributions of* COD *during the following 1 (a) and 6 hours (b) after the giant or not giant event.*

Figure 7.6 shows the same data classified according to the atmospheric stability. In this case, after 1 *hour* (*Fig. 7.6a*) the mean values of COD for giant aerosol observations are slightly higher in the stability conditions 1 and 3, and lower in the stability condition 2. The stability condition 1 corresponds to the most unstable case, indicating that the presence of giant aerosols promote the presence of higher COD values. The same effect is observed for stability condition 3 (the most stable), while an inversed behaviour is detected for condition 2 (intermediate stability). The reason for this behaviour is unknown, and these results should be treated with care, since the number of cases is small, as shown in *Table 7.2*. The same situation is observed after 6 *h* (*Fig. 7.6b*), suggesting the time passed from the observations does not affect this variable.

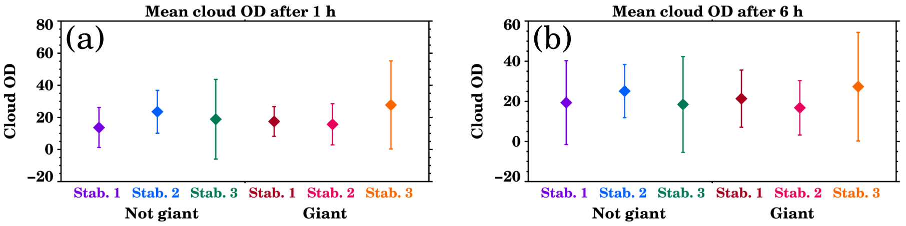

Figure 7.6: *Mean* COD *values during the following 1 hour (a) and 6 hours (b) after the event for cases of not giant and giant aerosol observations and according to the atmospheric stability. The error bars correspond to the standard deviation. "Stab." stands for atmospheric stability condition, where "1" has the lower stability and "3" the highest.*

Table 7.2: *Number of giant and not giant cases for the initial cases and with available* COD *data. The stability types defined are: 1 ($\omega \leq -0.001$ Pa s^{-1}), 2 (-0.01 < $\omega \leq -0.001$ Pa s^{-1}) and 3 ($\omega > 0.001$ Pa s^{-1}).*

Parameter	Stability condition	Giant	Not giant
Cases	All	150	159
COD	All	30	33
	1	7	8
	2	13	16
	3	10	9

7.3 Integrated Water Vapour and Liquid Water Path

The Integrated Water Vapour (IWV) is the total amount of water vapour present in a vertical atmospheric column, and is usually measured in *km* m^{-2} or *cm*.

The Liquid Water Content (LWC) is the measure of the mass of the water in a cloud in a specified amount of dry air, and it is typically measured per volume of air (g/m^3) or mass of air (*g/kg*) (Bohren and Albrecht, 1998). Clouds that have low densities, such as cirrus clouds, contain very little water, thus resulting in relatively low liquid water content values of around 0.03 g/m^3. Clouds that have high densities, like cumulonimbus clouds, have much higher liquid water content values that are around 1-3 g/m^3, as more liquid is present in the same amount of space (Thompson, 2007). The Liquid Water Path (LWP) is the total amount of LWC in a vertical atmospheric column, and is usually measured in $g\ m^{-2}$ or *mm*.

The MWR retrievals of IWV and LWP are used in this study. These variables are available for 92 giant aerosol observation cases and 144 not giant aerosol cases. More information about the corresponding stability conditions is reported in *Table 7.3*.

The frequency distribution of IWV and the mean values 1 *hour* after the giant or not giant aerosol events is presented in *Figure 7.7*. A different IWV distribution (*Fig. 7.7a*) is observed: below 1.5 *cm*, the frequency for cases of not giant aerosol observations is higher. The situation is the opposite over

Table 7.3: *Number of giant and not giant cases for the initial cases and with available IWV and LWP data. The stability types defined are: 1 ($\omega \leq -0.001$ Pa s^{-1}), 2 (-0.01 < $\omega \leq -0.001$ Pa s^{-1}) and 3 ($\omega > 0.001$ Pa s^{-1}).*

Parameter	Stability condition	Giant	Not giant
Cases	All	150	159
IWV / LWP	All	92	144
	1	23	49
	2	45	59
	3	24	33

that value: the frequency for cases of giant aerosol observations is higher. The differences cannot be linked to the giant aerosols presence but to the seasonality of this parameter. To demonstrate the latter, in *Figure 7.8* the annual evolution of IWV is plotted. The IWV is lower during the winter months and higher during summer. Therefore, the differences in the IWV frequency distribution can be explained by the higher frequency of giant cases during summer. This fact should be considered in the analysis of the LWP. The compared mean IWV (*Fig. 7.7b*) showed no significant differences between giant and not giant aerosol observations, nor between the different stability conditions.

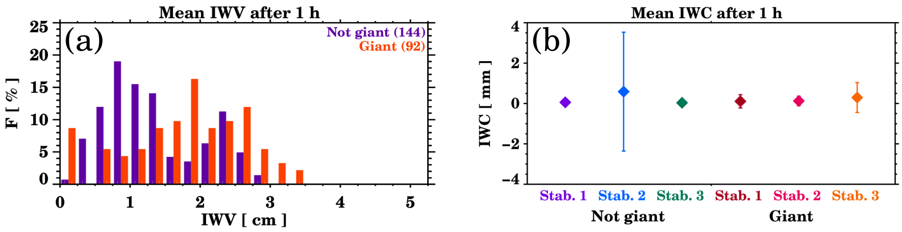

Figure 7.7: *(a) Frequency distribution of the IWV values during the following 1 hour after the event for not giant and giant aerosol observations according to the atmospheric stability. (b) Mean IWV values for the same time interval. The error bars correspond to the standard deviation. "Stab." stands for atmospheric stability condition, where "1" has the lower stability and "3" the highest.*

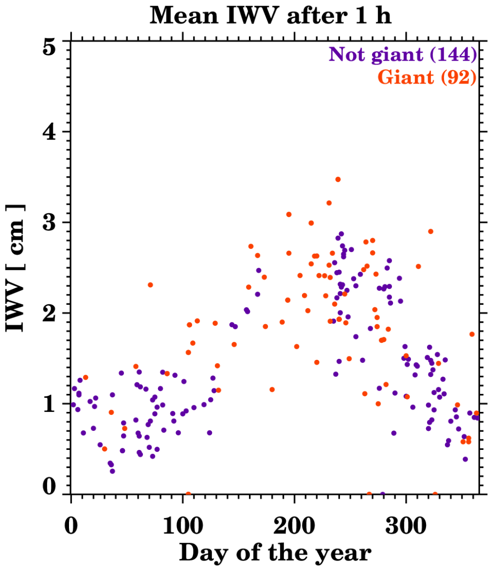

Figure 7.8: *Annual evolution of the IWV values during the following 1 hour after the event for not giant and giant aerosol observations according to the atmospheric stability.*

The frequency distribution of LWP 2 and 6 *hours* after giant or not giant aerosol observations is presented in *Figure 7.9*. The different time intervals, here, facilitate to identify whether the CCN efficiency of the giant aerosol observations is higher. The distribution after 2 *hours* (*Fig. 7.9a*) is very similar for both cases. However, the behaviour of LWP after 6 *hours* (*Fig. 7.9b*) is altered: LWP values over 0.15 *mm* are more frequent when giant aerosols have been previously observed. As for IWV, here, we assess the seasonality of LWP. In *Figure 7.10*, no correlation was found. Thus, we believe that the higher values of LWP 6 *hours* after the observation of giant aerosols are due to higher CCN efficiency.

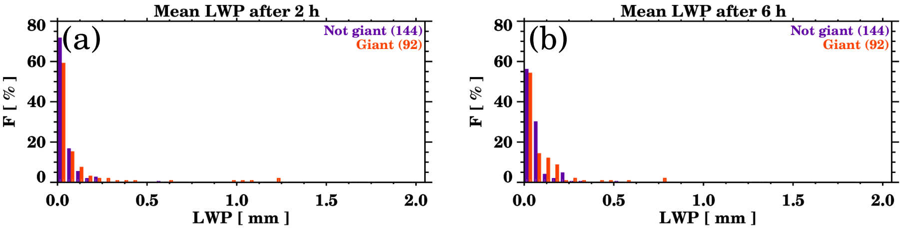

Figure 7.9: *Frequency distribution of the LWP values during the following 2 (a) and 6 hours (b) after the event for not giant and giant aerosol observations.*

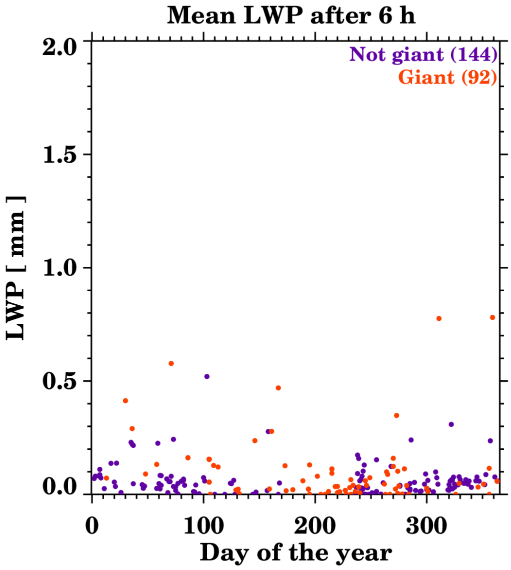

Figure 7.10: *Distribution of the* LWP *values along the year during the following 6 hours after the event for not giant and giant observations.*

Figure 7.11 presents the differences between the LWP means after not giant and giant aerosol observations according the the stability conditions. Once more, the are no significant discrepancies between the two categories or depending on the stability conditions.

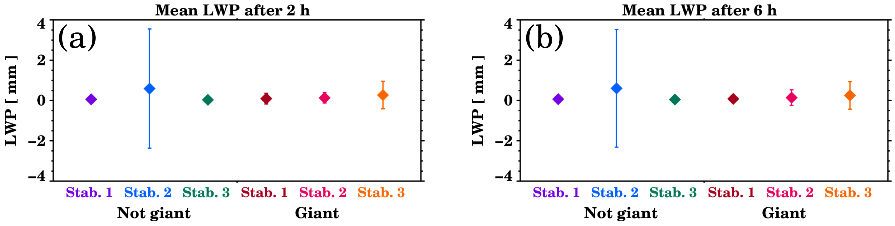

Figure 7.11: *Mean* LWP *values during the following 2 (a) and 6 hours (b) after the event for not giant and giant aerosol observations according to the atmospheric stability. The error bars correspond to the standard deviation. "Stab." stands for atmospheric stability condition, where "1" has the lower stability and "3" the highest.*

Finally, a comparison between the IWV and the LWP 1 *hour* after for not giant and giant aerosol observations is performed screening the data by the stability conditions, as shown in *Figure 7.12*. In this scatter plot, the first thing to note is that there is no dependency between the IWV and their related LWP for LWP values lower than 0.2 *mm*. Over this threshold, higher IWV values correspond to also higher LWP values. In fact, almost all the LWP values over 0.2 *mm* correspond to giant cases. This indicates that in presence of giant aerosols, the formation of water droplets is more efficient given the same amount of IWV in the atmosphere.

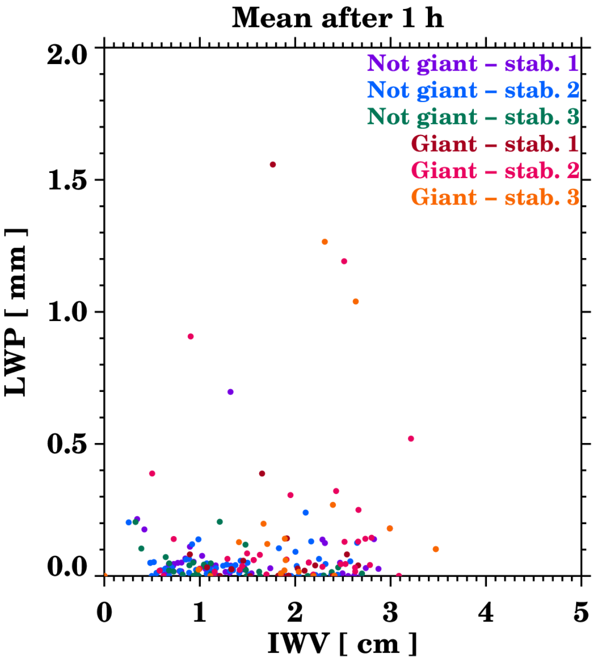

Figure 7.12: *IWV versus LWP values during the following 1 hour after the event for not giant and giant cases according to the atmospheric stability. In the legend, "stab." stands for atmospheric stability condition, where "1" has the lower stability and "3" the highest.*

7.4 Precipitation

Giant aerosols can act as GCCN and IN, affecting the precipitation formation and the temperature at which ice nucleation initiates. Hence, the giant aerosol observations are compared with precipitation measurements and compared to control cases to investigate if, in fact, they have an effect on precipitation.

The precipitation measurements are performed by the Regional Civil Protection, which we refer to as regional. This implies that case occurrence is considered not as a local event but as horizontally distributed over a certain mesoscale spatial domain. The region is divided into three different hydrological groups, as presented previously in *Figure 3.5* (*Chapter 3*).

In *Fig. 7.13*, the frequency distribution of accumulated rain in the three hydrological basins during the 24 *hours* following the event (giant or not giant aerosol observations) is shown. The cases in which the accumulated rain was equal to 0 *mm* are not plotted in the histogram, and are noted in parenthesis in the legend. The percentage of cases in which it did not rain after the event is slightly lower after the observation of giant aerosols for all the basins (4.7, 2.2 and 1.0% for A, B and C respectively). This indicates that after the observation of giant aerosols, it is most likely to experience slight increases in precipitation. The most frequent rain amount within 24 *hours* is lower than 5 *mm*, and most values concentrate below 25 *mm*. The maximum accumulated rain was for Group C, which corresponds to the region at the south of the CIAO observatory.

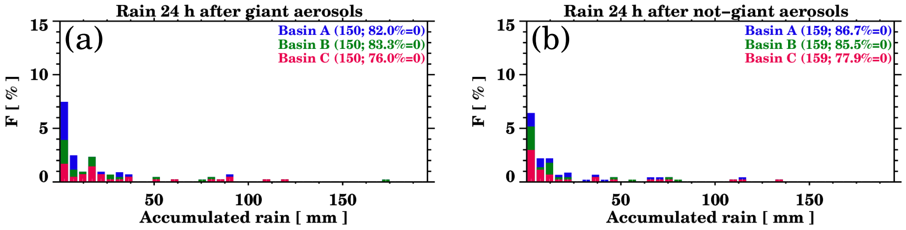

Figure 7.13: *Total accumulated rain in the three hydrological groups in presence of (a) giant and (b) not giant aerosol in the 24 hours following the events. In parenthesis, the number of cases considered in the statistics for each basin together with the percentage of events without precipitation are noted.*

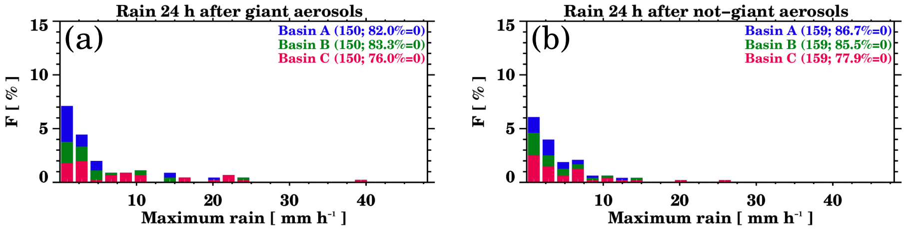

Figure 7.14: *Maximum rain rate in the three hydrological groups in presence of (a) giant and (b) not giant aerosol in the 24 hours following the events. In parenthesis, the number of cases considered in the statistics for each basin together with the percentage of events without precipitation are noted.*

Figure 7.14 presents the maximum rain rate frequency distribution in the three hydrological groups during the 24 *hours* following the giant or not giant aerosol observations. The cases in which the maximum rain rate was equal to 0 *mm* h^{-1} are not plotted in the histogram, and are noted in parenthesis in the legend. There are no major differences below 10 *mm* h^{-1}. The frequencies over this value, though, are higher after the giant aerosol observations, suggesting that these particles contribute to invigorate clouds.

The meteorological situation plays an important role in the precipitation formation, and thus in the total amount of precipitation and maximum rain rate. For this reason, the precipitation data was classified depending on the atmospheric stability condition. *Table 7.4* reports the number of cases corresponding to each stability type for giant and not giant events.

Table 7.4: *Number of giant and not giant aerosol observations for the initial cases and with available rain gauges measurements. The stability types defined are: 1 ($\omega \leq -0.001$ Pa s^{-1}), 2 (-0.01 < $\omega \leq -0.001$ Pa s^{-1}) and 3 ($\omega > 0.001$ Pa s^{-1}).*

Parameter	Stability condition	Giant	Not giant
Cases	All	150	159
Precipitation	All	150	159
	1	30	45
	2	87	67
	3	29	39

Figure 7.15 presents the mean precipitation accumulation during the 12 and 24 *hours* after giant and not giant aerosol observations. The mean accumulated rain during the 12 *hours* following the event (*Fig. 7.15a*) is bigger after giant aerosol observations for all the stability conditions. The biggest difference is 18.8 *mm* and refers to Condition 1. The difference for the stability Condition 2 is 3.4 *mm*, and 9.1 *mm* for the Condition 3. The stability Condition 1 is related to the highest atmospheric instability, which fosters the cloud formation. Hence, precipitation formation is enhanced after the presence of giant aerosols. For the other stability conditions, there is also a precipitation enhancement, but not as pronounced as for Condition 1. During the next 24 *hours* after the events (*Fig. 7.15b*), the same effect is observed in stability Condition 1: the mean accumulated rain is 7.4 *mm* higher after giant aerosols observations. For the stability Condition 2, the precipitation accumulation after

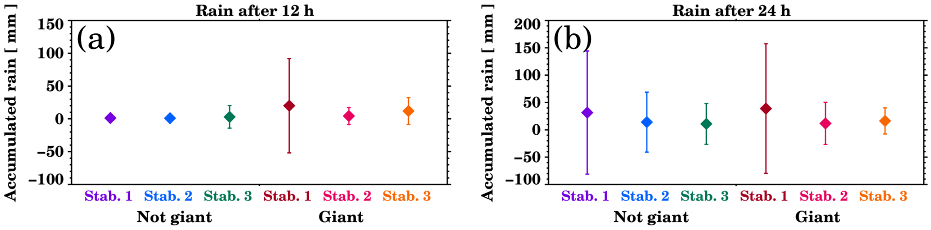

Figure 7.15: *Mean precipitation accumulation during the (a) 12 and (b) 24 hours after giant and not giant aerosol observations according to the atmospheric stability conditions. "Stab." stands for atmospheric stability condition, where "1" has the lower stability and "3" the highest.*

giant aerosol observations is lower; the difference is -2.4 *mm* in this case. Furthermore, as after 12 *hours*, there is an increase of precipitation for the stability Condition 3 after giant aerosol observations; the difference, here, is 5.4 *mm*. The increase of accumulated rain is proportionally much higher during the 12 *hours* following the event than during the 24 *hours*. For the stability Condition 1, for example, the relative increase of rain accumulation due to giant aerosols is of 1457% after 12 *hours*, while it is 23% after 24 *hours*. There are two possible explanations for this effect. The first could be the daily convection evolution. Since the time selected for the study is between 13:00 and 14:00 local time, the next 12 *hours* comprise of convective cloud development, and therefore the afternoon and evening showers. The 24 *hours* after the event include the same time period plus the night and morning of the next day, in which the clouds are less invigorated by the convection processes. The second possibility could be related to the time needed for the precipitation formation: it is more likely that clouds form and precipitate within 12 *h* from the event rather than within 24 *h*.

The maximum rain rate during the 12 *h* and 24 *h* after the event for the different stability conditions is shown in *Figure 7.16*. An increase of the mean maximum rain rate is observed after giant aerosols observations for all the stability conditions, both during the 12 and 24 *h* after the events. During the following 12 *h* (*Fig. 7.16a*), the presence of giant aerosols produces an increase of 2.0, 1.1 and 3.4 $mm\ h^{-1}$ for the stability conditions 1, 2 and 3 respectively. During the following 24 *h* (*Fig. 7.16b*), the increases are relatively smaller: 0.9, 0.6 and 3.2 $mm\ h^{-1}$ for the three stability conditions respectively. As for the accumulated rain, the relatively smaller increases after 24 *h* can be linked to the selected time intervals or to the precipitation timing.

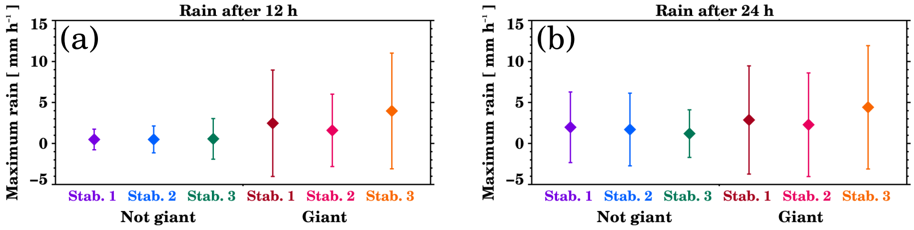

Figure 7.16: *Maximum rain rate observed during the (a) 12 and (b) 24 hours after giant and not giant aerosol observations according to the atmospheric stability conditions. “Stab.” stands for atmospheric stability condition, where “1” has the lower stability and “3” the highest.*

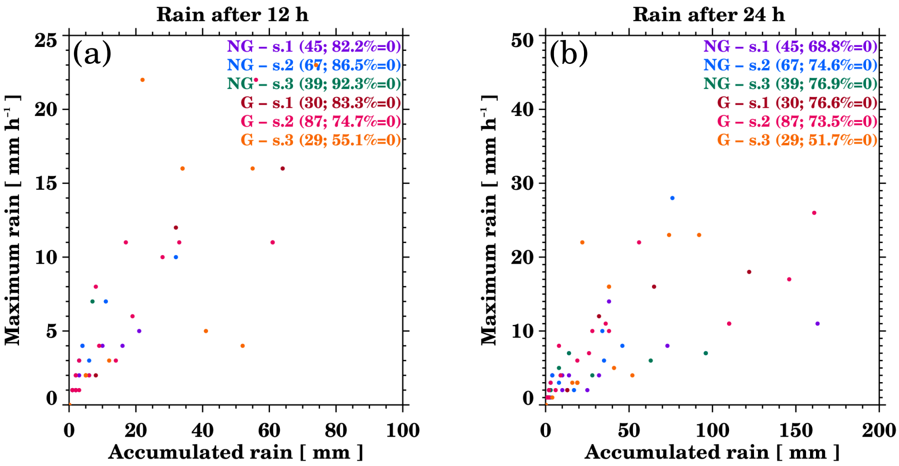

Figure 7.17: *Total accumulated rain in all the basins versus maximum rain rate for giant and not giant aerosol observations (a) 12 and (b) 24 hours after the observations. In the legend, “NG” stands for not giant, “G” for giant, and “s” for stability condition. In parenthesis, the number of cases considered in the statistics with the percentage of events without precipitation are reported.*

The relation between the total amount of precipitation and the maximum rain rate is plotted in *Figure 7.17*. During the next 12 *h* after the event (*Fig. 7.17a*), the points with accumulated rain over 25 *mm* and rain rates over 6 $mm\ h^{-1}$ correspond, mainly, to giant aerosol cases. This illustrates the effect that giant aerosols have on extreme rain events. Surprisingly, the events with a higher relation between the maximum rain and accumulated rain correspond to giant aerosol cases in the highest atmospheric stability (Condition 3) and not to the highest instability case (Condition 1). During the next 24 *h* after the event (*Fig. 7.17b*), a similar effect is observed, corresponding the highest values of accumulated rain and maximum rain rate principally to the giant aerosol cases. In this case, the higher relation between the maximum rain rate and the accumulated rain corresponds to giant cases for the stability Condition 3, as observed after 12 *h*. In the comparison between the scatter plots for the two time intervals, the most remarkable feature is the different slope of the maximum rain rate and the accumulated rain: it is much higher after 12 *h* than after 24 *h*. A higher slope means that the rain rate corresponding to a precipitation event, given the same accumulation, is higher. Thus, the precipitation events after 12 *h* are more torrential than after 24 *h*. As previously discussed, this can be attributed either to the diurnal cycle or to the precipitation formation timing.

In conclusion, we found that giant aerosols contribute to an increase of the accumulated rain and to an increase of the maximum rain rate.

7.5 All variables

Table 7.5 summarises the stability conditions for which each variable is maximum after giant and not giant aerosol observations. After observations of giant aerosols, all the variables except the accumulated rain are maximum for Condition 3 (highest atmospheric stability). The accumulated rain is maximum for Condition 1, associated with the most unstable conditions. After observations of not giant aerosols, the COD, IWV and LWP are maximum for Condition 2 (intermediate atmospheric stability), and no preference was observed for the accumulated rain nor for the maximum rain rate. The behaviour of the different variables indicates that the atmospheric stability has a higher impact on them after giant aerosol observations. The exception after giant aerosol observations is the accumulated rain, which is maximum for Condition 1. This fact could be due to a faster CCN activation, where the updrafts are more likely to occur. The same behaviour could be expected for the maximum rain rate, but it is not the case. Therefore, a more detailed study which considers other parameters such as the precipitation formation time should be done to better understand these effects.

Table 7.5: *Stability conditions for which the different variables are maximum after giant and not giant observations. The stability types defined are: 1 ($\omega \leq -0.001$ Pa s^{-1}), 2 ($-0.01 < \omega \leq -0.001$ Pa s^{-1}) and 3 ($\omega > 0.001$ Pa s^{-1}). No data indicates almost identical values for all the stability conditions.*

Variable	Giant	Not giant
COD	3	2
IWV	3	2
LWP	3	2
Accumulated rain	1	–
Maximum rain rate	3	–

8

Conclusions

The topic of this thesis was the investigation of tropospheric aerosols by exploiting the synergy of two ground-based remote sensing instruments, multi-wavelength Raman lidar and Doppler cloud radar.

The thesis was focused, particularly, on the study of giant aerosol particles. Giant aerosols affect the cloud development and rain formation by acting as Cloud Condensation Nuclei (CCN) (Dagan et al., 2015) and Ice Nuclei (IN) (Möhler et al., 2006). Several studies have found that they have contradictory effects on precipitation: from the expedition of, specially, warm rain processes (i.e. Feingold et al., 1999) to their suppression (i.e. L'Ecuyer et al., 2009). Moreover, the main instruments used nowadays to measure aerosols –lidar and sun photometer– cannot retrieve aerosol microphysical properties for particles bigger than a few microns and, therefore, they do not account for giant and ultragiant aerosols. This lack of observations is translated into a scarce knowledge about the giant aerosols distribution and effects and into a large underestimation by aerosol transport models (Ginoux et al., 2011). In consequence, this study intends to fill the giant aerosols observational gap to get a deeper understanding of their characteristics and effects.

The research presented here was carried out using the CIAO infrastructure, the CNR-IMAA Atmospheric Observatory, which is located in southern Italy. The main instruments utilized were two advanced multi-wavelength Raman lidars and a millimeter wavelength cloud radar. The operating wavelengths of the two lidars (355, 532 and 1064 *nm*) are four orders of magnitude lower than the Ka-band cloud radar wavelength (8.45 *mm*). Accordingly, they provide complementary information about different parts of the aerosol size distribution.

During the preparation of this thesis, considerable work has been carried out to enlarge the size range in which aerosols can be characterized. This objective has been reached by achieving three main goals: (a) the development of an automatic aerosol classification algorithm based on cloud radar observations; (b) the analysis of lidar measurements simultaneous to cloud radar aerosol observations; and (c) the synergystic use of both instruments to obtain an enlarged aerosol size distribution. Moreover, the effects of giant aerosols on precipitation as well as on other atmospheric variables have been studied to assess their role in the atmosphere.

In this study, giant aerosols have been methodically observed and characterized by cloud radar measurements for the first time. A novel methodology for giant and ultragiant aerosols detection was developed with this purpose. In summary, it consists in separating the radar observations of non-hydrometeorological targets into aerosols and insects, for which the findings of several entomology studies regarding the insects behaviour in the atmosphere were used. The application of the methodology to approximately six years of measurements yielded to the identification of more than three hundred giant aerosol layers. The maximum number of layers observed occurred during summer, and a relative maximum is observed in spring. Together with a minimum during winter, the seasonal evolution of giant aerosols is in agreement with climatological studies of the site realized using lidar measurements (i.e. Mona et al., 2009). Thus, it is likely that particles of all sizes reach the site together in many cases, as for example during dust outbreaks. Lastly, considering the continuous cloud radar operation, the developed method could be very useful for monitoring continuously and in near real-time coarse aerosol particles such as dust, pollen and volcanic aerosols.

The analysis of lidar measurements simultaneous to the identification of giant aerosol layers presented in this thesis is important for various reasons. First, it provides information about fine aerosol particles. Second, the lidar information is unique to identify different types of particles. And third, lidars are effective aerosol monitoring instruments and they have been used to study airborne particles for several decades. For the six year-long explored dataset, 40 simultaneous lidar measurements were found, considering day- and night-time conditions. Among all the lidar aerosol observations, 22 corresponded to aerosol observations also by the cloud radar. For the rest, 18 cases, the cloud radar identified insects, according to the novel classification methodology. To see if the insects behaviour in the atmosphere, such as flying altitudes, depends on the aerosol load and characteristics, the aerosol optical properties obtained by the lidar were categorized according to the target observed by the cloud radar (aerosols or insects) and compared. No major differences in the aerosol properties were observed depending on the cloud radar aerosols or insects observations.

The synergistic use of the lidar and radar simultaneous measurements was not possible for the retrieval of the aerosol microphysical properties. The initial intention was to use the three lidar wavelengths and the radar measurements jointly in order to retrieve the aerosol properties. After calculating the scattering efficiencies at the four wavelengths and comparing the aerosol vertical profiles for several cases, it was found that, in fact, the lidar and radar are sensitive to different parts of the aerosol size distribution. Therefore, the two instruments observe different particles, and a joint retrieval of the aerosol properties is not feasible. Accordingly, the approach followed to enlarge the aerosol size distribution consisted of the size distribution and the microphysical properties retrieval for each instrument measurements separately and their subsequent combination. The retrieval of the aerosol properties as measured by the lidar was accomplished by using the code introduced by Veselovskii et al. (2010), which makes use of the backscatter and extinction measurements at different wavelengths to carry out the inversion. The retrieval of the aerosol properties as measured by the radar was more complex. Since this thesis is the first attempt to observe and characterize aerosols with cloud radar in a systematic way, inversion codes are non-existing. Hence, it was necessary to create a code for the retrieval of aerosol properties. The method developed consists of two main parts: the creation of a scattering database and the inversion of the data. The database was generated by using the T-matrix scattering code developed by Mishchenko and Travis (1998). It was used to compute the reflectivity and Linear Depolarization Ratio (LDR) values at the cloud radar wavelength for a broad ensemble of particle sizes, shapes, refractive indices and number concentrations.

Afterwards, the retrieval of the aerosol properties and size distribution was achieved by selecting the aerosol particles for which the computed reflectivity and LDR was closer to the measured values. Finally, the aerosol size distribution from the fine to the giant mode was obtained by combining the obtained information of the instruments inversion procedures. The results from this synergy show that the giant particles are a small portion of the total aerosol load but, nevertheless, they are very relevant in terms of surface and volume.

Finally, the effects of giant aerosols on the local meteorology were studied by correlating the observations of giant particles with different atmospheric variables and comparing them to *control observations* (giant particles not observed). The approach followed in this investigation is based on the selection of a day time interval and the screening of the data according to the atmospheric stability, which was estimated by the pressure vertical velocity in the upper atmosphere. Giant aerosol influence on the Aerosol Optical Depth (AOD) and Ångström exponent at different wavelengths, as measured by AERONET, was not observed. Considering that its measurements are columnar, this suggests that giant aerosols constitute a small portion of the columnar aerosol load. On the contrary, it was found that giant aerosols have an effect on the Cloud Optical Depth (COD), also retrieved by AERONET. Higher values of COD were observed after giant aerosol observations, specially in the most unstable atmospheric conditions. This indicates an invigorating effect of clouds owing to giant aerosols presence. Regarding the Liquid Water Path (LWP), we observed higher LWP values when giant aerosols were detected few hours before. This could indicate a higher CCN efficiency of the giant aerosol particles. Last, the effects of giant aerosols on precipitation at a regional scale were explored. Giant aerosols were found to enhance the accumulated precipitation as well as the maximum rain rate. These enhancements were remarkably higher when the atmospheric stability was low. Our findings are in accordance with the studies of Eagan et al. (1974) and Feingold et al. (1999) for the enhancement of warm rain processes and with Koren et al. (2010, 2012, 2014) regarding the rain rate increase.

During the investigation carried out for this thesis, several limitations were identified that can introduce uncertainties and biases in the obtained results. First, the identification of aerosol layers by the cloud radar is limited to the layers that are lofted in respect to the insects flying regions, since the radar reflectivity is proportional to the target diameter to the sixth power and insects are some orders of magnitude bigger than aerosols. In light of this, the definition of lofted layers (i.e. how distant should they be from the insect flying areas) is critical, and it could probably be overcome by estimating the Planetary Boundary Layer (PBL) height from the lidar or ceilometer observations. Second, several thresholds are set in our methodology for cloud radar aerosol observations (i.e. height difference in respect to the temperature inversion height during night). These thresholds should probably change depending on the seasonal fluctuations of insects. Third, the application of this methodology requires ancillary data, which should be available to monitor in near real-time the presence of giant aerosols. Fourth, the number of simultaneous lidar and cloud radar aerosol measurements is limited due to the lidar measurements schedule. Fifth, the T-matrix scattering calculations yielded lower LDR values than the measured by the radar in many cases, implying a crucial limitation for the inversion method. Here, the important limiting factor is the inadequate modelling of the non-spherical aerosol properties: the spheroid approximation currently used in most of the remote sensing applications is unable to reproduce the backscattering characteristics of dust and this can lead to a bias in the retrievals (Binietoglou, 2014).

In spite of all the limitations, the observation and retrieval methodologies developed in this thesis are a very important achievement for the study of giant aerosols and can be used as a basis for innovative research in many different directions. The giant aerosol detection methodology in cloud radar measurements could be applied in near real-time in order to monitor continuously the presence of giant aerosols in the atmosphere. Moreover, these observations could be assimilated into aerosol transport models in order to overcome their typical underestimation of the biggest aerosol fraction. Moreover, the combination of lidar and radar observations for the retrieval of an enlarged aerosol size distribution could be applied and studied in different sites, contributing to better understand the giant aerosols. Finally, the research on the giant aerosol effects on the local meteorology presented promising results for the study of the effects of these particles and could be done for different conditions and applied in different locations.

The performed study also highlighted several paths of research that could be followed to improve the current giant aerosols remote sensing capabilities. The validation of the results with independent measurements is essential, and further research should be done in this way. Aerosols in-situ observations, such as air-borne, could be used to validate the methodology for giant aerosol detection in cloud radar data as well as the retrieval of aerosol microphysical properties and size distribution from lidar and radar measurements. Besides, the radar inversion method could be improved by the generation of a more complex scattering database, which should include different particle orientations and more complex and irregular particle shapes. The effects of giant aerosols on the local meteorology could be explored for a much wider series of conditions. For example, the data could be screened, apart than by the atmospheric stability, by other parameters such as the AOD and the LWP. Moreover, the effects of giant aerosols on precipitation could be investigated more thoroughly, for example realising the study for different times of the day (i.e. morning and afternoon), calculating the time precipitation needs to be formed or considering the precipitation only in the stations within the giant aerosols atmospheric circulation modelled path.

Summing up, the main novelties of this thesis are: (a) the use of cloud radar for the first time to study aerosols in a methodical way and for a long time interval, for which a whole new methodology has been developed; (b) the creation of a novel inversion procedure to retrieve aerosol microphysical properties with a cloud radar; and (c) the enhancement of the size range in which aerosol microphysical properties can be characterized.

In conclusion, the research carried out in this thesis produced important results that allow a better understanding of the role and importance of giant and ultragiant aerosols in meteorology and climate.

Acknowledgements

First of all, I would like to express my deep gratitude to Dr. Aldo Amodeo and Dr. Fabio Madonna, my research supervisors, for their patient guidance, enthusiastic encouragement and useful ideas and critiques of this research work.

I would also like to thank Dr. Gelsomina Pappalardo, Dr. Matthias Bauer-Pfundstein and Prof. Herman Russchenberg for their guidance and advice along the last three years. I also need to acknowledge all the members of the Initial Training for atmospheric Remote Sensing (ITARS) network, which influenced considerably in the improvement of this work. Specially, I would like to thank Dr. Christine Chiu, as her careful reading of the thesis and her useful suggestions contributed substantially to the final result, as well as all the ITARS fellows for all the shared experiences along the past three years.

I am also very grateful of each one of the persons of the CNR-IMAA Atmospheric Observatory (CIAO) group. I would like to thank Aldo G., Lucia, Giuseppe and Simone for their companionship and good humour, Iannis and Miky for their friendship and discussions, Francesco for all the coffees and particularly Marco and Nikos for our good times at the office.

The financial support by the European Community throught the Aerosols, Clouds and Trace gases Research InfraStructure network (ACTRIS) Research Infrastructure Action under the 7th Framework Programme under ACTRIS Grant Agreement n° 262254 and ITARS Grant Agreement n° 289923 and by the national project "Programma Operativo Nazionale (PON) Regione Basilicata 2000/2006" are gratefully acknowledged.

Finally, I would like to thank I. Veselovskii for the availability of his aerosol microphysical properties inversion code, M.I. Mishchenko for the availability of the T-matrix scattering code, and FLEXible PARTicle dispersion model (FLEXPART), Moderate Resolution Imaging Spectroradiometer (MODIS) and the Civil Protection of Basilicata Region for the availability of their data.

Bibliography

Adams, R., Perger, F., Rose, W., and Kostinski, A. (1996). Measurements of the complex dielectric constant of volcanic ash from 4 to 19 GHz. *J. Geophys. Res.*, 101:8175–8185.

Albrecht, B. A. (1989). Aerosols, cloud microphysics, and fractional cloudiness. *Science*, 245(4923):1227–1230.

Amiridis, V., Giannakaki, E., Balis, D., Gerasopoulos, E., Pytharoulis, I., Zanis, P., Kazadzis, S., Melas, D., and Zerefos, C. (2010). Smoke injection heights from agricultural burning in Eastern Europe as seen by CALIPSO. *Atmospheric Chemistry and Physics*, 10(23):11567–11576.

Amodeo, A. (2010). Uncertainties evaluation for aerosol optical properties. In *2nd GALION Workshop - EARLINET-ASOS Symposium*, Geneva, Switzerland.

Ansmann, A. and Müller, D. (2005). *Lidar: Range-Resolved Optical Remote Sensing of the Atmosphere*, chapter Lidar and Atmospheric Aerosol particles. Springer.

Ansmann, A., Riebesell, M., and Weitkamp, C. (1990). Measurement of atmospheric aerosol extinction profiles with a Raman lidar. *Optics letters*, 15(13):746–748.

Ansmann, A., Seifert, P., Tesche, M., and Wandinger, U. (2012). Profiling of fine and coarse particle mass: case studies of Saharan dust and Eyjafjallajökull/Grimsvötn volcanic plumes. *Atmospheric Chemistry and Physics*, 12(20):9399–9415.

Ansmann, A., Wandinger, U., Riebesell, M., Weitkamp, C., and Michaelis, W. (1992). Independent measurement of extinction and backscatter profiles in cirrus clouds by using a combined Raman elastic-backscatter lidar. *Applied Optics*, 31(33):7113–7131.

Ayris, P. and Delmelle, P. (2012). The immediate environmental effects of tephra emission. *Bulletin of Volcanology*, 74(9):1905–1936.

Bass, M., DeCusatis, C., Enoch, J., Lakshminarayanan, V., Li, G., Mac-Donald, C., Mahajan, V., and Stryland, E. V. (2009). *Handbook of Optics, Third Edition Volume I: Geometrical and Physical Optics, Polarized Light, Components and Instrument*. McGraw-Hill Professional, New York, 3rd edition edition.

Bauer-Pfundstein, M. (2009). *Ka Band Cloud Radar MIRA 36, Theory of Data Processing*. METEK Meteorologische Messtechnik GmbH.

Bauer-Pfundstein, M. and Görsdorf, U. (2007). Target separation and classification using cloud radar Doppler-spectra. In *Proceedings 33rd Intern. Conf. on Radar Meteorology, Cairns*.

Binietoglou, I. (2014). *Synergies of ground based remote sensing techniques for aerosol mass profiling*. PhD thesis, University of Basilicata.

Binietoglou, I., Basart, S., Alados-Arboledas, L., Amiridis, V., Argyrouli, A., Baars, H., Baldasano, J., Balis, D., Belegante, L., Bravo-Aranda, J., et al. (2015). A methodology for investigating dust model performance using synergistic EARLINET/AERONET dust concentration retrievals. *Atmospheric Measurement Techniques Discussions*, 8(4):3605–3666.

Bohren, C. F. and Albrecht, B. A. (1998). *Atmospheric Thermodynamics*. Oxford University Press, 1st edition.

Burton, S., Ferrare, R., Hostetler, C., Hair, J., Rogers, R., Obland, M., Butler, C., Cook, A., Harper, D., and Froyd, K. (2012). Aerosol classification using airborne High Spectral Resolution Lidar measurements–methodology and examples. *Atmospheric Measurement Techniques*, 5(1):73–98.

Burton, S., Ferrare, R., Vaughan, M., Omar, A., Rogers, R., Hostetler, C., and Hair, J. (2013). Aerosol classification from airborne HSRL and comparisons with the CALIPSO vertical feature mask. *Atmospheric Measurement Techniques*, 6(5):1397–1412.

Chapman, J., Drake, V., and Reynolds, D. (2011). Recent insights from radar studies of insect flight. *Annu. Rev. Entomol.*, 56:337–356.

Chapman, J., Reynolds, D., and Smith, A. (2004). Vertical-looking radar: a new tool for monitoring high-altitude insect migration. *BioScience*, 53:503–5011.

Chiu, J. C., Huang, C., Marshak, A., Slutsker, I., Giles, D. M., Holben, B. N., Knyazikhin, Y., and Wiscombe, W. J. (2010). Cloud optical depth retrievals from the Aerosol Robotic Network (AERONET) cloud mode observations. *J. Geophys.Res.*, 115(D14202).

Clothiaux, E., Ackerman, T., Mace, G., Moran, K., Marchand, R., Miller, M., and Martner, B. (2000). Objective determination of cloud heights and radar reflectivities using a combination of active remote sensors at the ARM CART sites. *J. Appl. Meteor.*, 39:645–665.

Dagan, G., Koren, I., and Altaratz, O. (2015). It is all about timing: evaluation of aerosol effects on warm rain processes. *Geophysical Research Letters*.

D'Almeida, G., Koepke, P., and Shettle, E. (1991). *Atmospheric Aerosol: Global Climatology and Radiative Characteristics*. A. Deepak.

DeMott, P. J., Sassen, K., Poellot, M. R., Baumgardner, D., Rogers, D. C., Brooks, S. D., Prenni, A. J., and Kreidenweis, S. M. (2003). African dust aerosols as atmospheric ice nuclei. *Geophysical Research Letters*, 30(14):n/a–n/a.

Di Girolamo, P., Ambrico, P. F., Amodeo, A., Boselli, A., Pappalardo, G., and Spinelli, N. (1999). Aerosol observations by lidar in the nocturnal boundary layer. *Applied optics*, 38(21):4585–4595.

Drake, V. (1984). The vertical distribution of macroinsects migrating in the nocturnal boundary layer: a radar study. *Bound.Layer Meteorol.*, 28:353–374.

Drake, V. and Farrow, R. (1988). The influence of atmospheric structure and motions on insect migration. *Annu. Rev. Entomol.*, 33:183–210.

Dubovik, O., Sinyuk, A., Lapyonok, T., Holben, B. N., Mishchenko, M., Yang, P., Eck, T. F., Volten, H., Munoz, O., Veihelmann, B., et al. (2006). Application of spheroid models to account for aerosol particle nonsphericity in remote sensing of desert dust. *Journal of Geophysical Research: Atmospheres (1984–2012)*, 111(D11).

Eagan, R., Hobbs, P., and Radke, L. (1974). Measurements of CCN and cloud droplet size distribution in the vicinity of forest fires. *J. Appl. Meteor.*, 13:553–537.

Feingold, G., Cotton, W., Kreidenweis, S., and Davis, J. (1999). The Impact of Giant Cloud Condensation on Drizzle Formation in Stratocumulus: Implications for Cloud Radiative Properties. *J. Atmos. Sci.*, 56:4100–4117.

Freudenthaler, V., Esselborn, M., Wiegner, M., Heese, B., Tesche, M., Ansmann, A., Müller, D., Althausen, D., Wirth, M., F., A., G., E., P., K., C., T., J., G., Garhammer, M., and Seefeldner, M. (2009). Depolarization ratio profiling at several wavelengths in pure Saharan dust during SAMUM 2006. *Tellus B*, 61:165–179.

Gallisai, R., Peters, F., Basart, S., and Baldasano, J. (2012). Mediterranean basin-wide correlations between Saharan dust deposition and ocean chlorophyll concentration. *Biogeosciences Discussions*, 9(7):8611–8639.

Gatehouse, A. (1997). Behavior and ecological genetics of wind-born migration by insects. *Annu. Rev. Entomol.*, 42:475–502.

Giglio, L., Descloitres, J., Justice, C. O., and Kaufman, Y. J. (2003). An enhanced contextual fire detection algorithm for MODIS. *Remote sensing of environment*, 87(2):273–282.

Ginoux, P., Prospero, J., Gill, T., and Hsu, N. (2011). Natural and anthropogenic dust: From sources to radiative forcing derived from satellite data and GFDL climate model. *Proceedings of the Fall Meeting, American Geophysical Union*.

Goudie, A. and Middleton, N. (2006). *Desert dust in the global system*. Springer.

Grainger, R. (2015). Some Useful Formulae for Aerosol Size Distributions and Optical Properties. Available at "http://eodg.atm.ox.ac.uk/user/grainger/research/aerosols.pdf". Consulted on 02/09/2015.

Groß, S., Esselborn, M., Weinzierl, B., Wirth, M., Fix, A., and Petzold, A. (2013). Aerosol classification by airborne high spectral resolution lidar observations. *Atmos. Chem. Phys.*, 13:2487 – 2505.

Groß, S., Freudenthaler, V., Schepanski, K., Toledano, C., Schäfler, A., Ansmann, A., and Weinzierl, B. (2015). Optical properties of long-range transported Saharan dust over Barbados as measured by dual-wavelength depolarization Raman lidar measurements. *Atmospheric Chemistry and Physics*, 15(19):11067.

Guerzoni, S. and Chester, R. (1996). *The impact of desert dust across the Mediterranean*, volume 11. Springer Science & Business Media.

Heese, B. and Wiegner, M. (2008). Vertical aerosol profiles from Raman polarization lidar observations during the dry season AMMA field campaign. *Journal of Geophysical Research: Atmospheres (1984–2012)*, 113(D23).

Henyey, L. and Greenstein, J. (1941). Diffuse radiation in the galaxy. *Astrophysical Journal*, 93:70–83.

Hinds, W., editor (1999). *Aerosol Technology: Properties, Behavior, and Measurement of Airborne Particles*. Wiley, 2nd edition.

Hobbs, P. (1993). Aerosol-Cloud-Climate Interactions. *Academic Press*.

Houghton, H. (1938). Problems connected with the condensation and precipitation processes in the atmosphere. *Bull. Am. Meteorol. Soc.*, 19:152–159.

Hudson, J. G. and Yum, S. S. (2001). Maritime-continental drizzle contrasts in small cumuli. *Journal of the atmospheric sciences*, 58(8):915–926.

IPCC (2013). Summary for Policymakers. In: Climate Change 2013: The Physical Science Basis. Contribution of Working Group I to the Fifth Assessment Report of the Intergovernmental Panel on Climate Change. Technical report, Intergovernmental Panel on Climate Change, Cambridge University Press, Cambridge, United Kingdom and New York, NY, USA. Stocker, T.F., D. Qin, G.K. Plattner, M. Tignor, S.K. Allen, J. Boschung, A. Nauels, Y. Xia, V. Bex and P.M. Midgley (eds).

Jacobson, M. Z. (2002). *Atmospheric pollution: history, science and regulation*. Cambridge.

Johnson, D. B. (1982). The role of giant and ultragiant aerosol particles in warm rain initiation. *Journal of the Atmospheric Sciences*, 39(2):448–460.

Kandler, K., Benker, N., Bundke, U., Cuevas, E., Ebert, M., Knippertz, P., Rodríguez, S., Schütz, L., and Weinbruch, S. (2007). Chemical composition and complex refractive index of Saharan Mineral Dust at Izaña, Tenerife (Spain) derived by electron microscopy. *Atmospheric Environment*, 41(37):8058–8074.

Kaufman, Y. J. (1993). Aerosol optical thickness and atmospheric path radiance. *J. Geophys. Res*, 98(D2):2677–2692.

Khain, A. P., Ovchinnikov, M., Pinsky, M., Pokrovsky, A., and Krugliak, H. (2000). Notes on the state-of-the-art numerical modeling of cloud microphysics. *Atmos. Res.*, 55:159–224.

Khandwalla, A., Majurec, N., Sekelsky, S., Williams, C., and Gage, K. (2002). Characterization of radar boundary layer data collected during the 2001 multi-frequency radar IOP. *Proceedings of the 12th ARM Science Team Meeting*.

Klett, J. (1981). Stable analytical inversion solution for processing lidar returns. *Applied Optics*, 20(2):211–220.

Klett, J. D. (1985). Lidar inversion with variable backscatter/extinction ratios. *Applied Optics*, 24(11):1638–1643.

Koren, I., Altaratz, O., Remer, L. A., Feingold, G., Martins, J. V., and Heiblum, R. H. (2012). Aerosol-induced intensification of rain from the tropics to the mid-latitudes. *Nature Geoscience*, 5(2):118–122.

Koren, I., Dagan, G., and Altaratz, O. (2014). From aerosol-limited to invigoration of warm convective clouds. *science*, 344(6188):1143–1146.

Koren, I., Feingold, G., and Remer, L. (2010). The invigoration of deep convective clouds over the Atlantic: aerosol effect, meteorology or retrieval artifact? *Atmospheric Chemistry and Physics*, 10(18):8855–8872.

Lasher-Trapp, S. and Stachnik, J. P. (2007). Giant and ultragiant aerosol particle variability over the eastern Great Lakes region. *Journal of applied meteorology and climatology*, 46(5):651–659.

L'Ecuyer, T. S., Berg, W., Haynes, J., Lebsock, M., and Takemura, T. (2009). Global observations of aerosol impacts on precipitation occurrence in warm maritime clouds. *Journal of Geophysical Research: Atmospheres (1984–2012)*, 114(D9).

Lovett, R. (2010). African dust keeps Amazon blooming. *Nature*.

Luke, E., Kollias, P., and K.L., J. (2007). A technique for the automatic detection of insect clutter in cloud radar returns. *J. Atmos. Ocean. Techn.*, 25:1498–1513.

Madonna, F., Amodeo, A., Boselli, A., Cornacchia, C., Cuomo, V., D'Amico, G., Giunta, A., Mona, L., and Pappalardo, G. (2011). CIAO: the CNR-IMAA advanced observatory for atmospheric research. *Atmos. Meas. Tech.*, 4:1191–1208.

Madonna, F., Amodeo, A., D'Amico, G., Mona, L., and Pappalardo, G. (2010). Observation of non-spherical ultragiant aerosol using a microwave radar. *Geophys. Res. Lett.*, 37.

Madonna, F., Amodeo, A., D'Amico, G., and Pappalardo, G. (2013). A study on the use of radar and lidar for characterizing ultragiant aerosol. *Geophys. Res.*, 118.

Maring, H., Savoie, D. L., Izaguirre, M. A., Custals, L., and Reid, J. S. (2003). Mineral dust aerosol size distribution change during atmospheric transport. *Journal of Geophysical Research: Atmospheres*, 108(D19):n/a–n/a. 8592.

Marticorena, B. (2007). Modelling mineral dust sources; present knowledge and limitations. *Geophysical Research Abstracts*, 9.

Marzano, F., Barbieri, S., Vulpiani, G., and Rose, W. (2006a). Volcanic cloud retrieval by ground-based microwave weather radar. *IEEE Trans. Geosci. Rem. Sens.*, 44(11):3235–3246.

Marzano, F., Vulpiani, G., and Rose, W. (2006b). Microphysical Characterization of Microwave Radar Reflectivity Due to Volcanic Ash Clouds. *IEEE Trans. Geosci. and Rem. Sens.*, 44:313–327.

Mishchenko, M., Travis, L., Kahn, R., and West, R. (1997). Modeling phase functions for dustlike tropospheric aerosols using a mixture of randomly oriented polydisperse spheroids. *J. Geophys. Res.*, 102:16831–16847.

Mishchenko, M. I. (1993). Light scattering by size–shape distributions of randomly oriented axially symmetric particles of a size comparable to a wavelength. *Applied optics*, 32(24):4652–4666.

Mishchenko, M. I. (2000). Calculation of the amplitude matrix for a nonspherical particle in a fixed orientation. *Applied Optics*, 39(6):1026–1031.

Mishchenko, M. I. and Travis, L. D. (1998). Capabilities and limitations of a current FORTRAN implementation of the T-matrix method for randomly oriented, rotationally symmetric scatterers. *Journal of Quantitative Spectroscopy and Radiative Transfer*, 60(3):309–324.

Mishchenko, M. I., Travis, L. D., and Mackowski, D. W. (1996). T-matrix computations of light scattering by nonspherical particles: A review. *Journal of Quantitative Spectroscopy and Radiative Transfer*, 55(5):535–575. Light Scattering by Non-Spherical Particles.

Möhler, O., Field, P. R., Connolly, P., Benz, S., Saathoff, H., Schnaiter, M., Wagner, R., Cotton, R., Krämer, M., Mangold, A., and Heymsfield, A. J. (2006). Efficiency of the deposition mode ice nucleation on mineral dust particles. *Atmospheric Chemistry and Physics*, 6(10):3007–3021.

Møller, A. (2013). Long-term trends in wind speed, insect abundance and ecology of an insectivorous bird. *Ecosphere*, 4(1).

Mona, L., Amodeo, A., Pandolfi, M., and Pappalardo, G. (2006). Saharan dust intrusions in the Mediterranean area: Three years of Raman lidar measurements. *Journal of Geophysical Research: Atmospheres (1984–2012)*, 111(D16).

Mona, L., Papagiannopoulos, N., Basart, S., Baldasano, J., Binietoglou, I., Cornacchia, C., and Pappalardo, G. (2014). EARLINET dust observations vs. BSC-DREAM8b modeled profiles: 12-year-long systematic comparison at Potenza, Italy. *Atmospheric Chemistry and Physics*, 14(16):8781–8793.

Mona, L., Pappalardo, G., Amodeo, A., d'Amico, G., Madonna, F., Boselli, A., Giunta, A., Russo, F., and Cuomo, V. (2009). One year of CNR-IMAA multi-wavelength Raman lidar measurements in coincidence with CALIPSO overpasses: Level 1 products comparison. *Atmospheric Chemistry and Physics*, 9(18):7213–7228.

Müller, D., Ansmann, A., Mattis, I., Tesche, M., Wandinger, U., Althausen, D., and Pisani, G. (2007). Aerosol-type-dependent lidar ratio observed with Raman lidar. *J. Geophys. Res*, 112.

Müller, D., Ansmann, A., Mattis, I., Tesche, M., Wandinger, U., Althausen, D., and Pisani, G. (2007). Aerosol-type-dependent lidar ratios observed with Raman lidar. *Journal of Geophysical Research: Atmospheres (1984–2012)*, 112(D16).

O'Dowd, C. and Leeuw, G. (2007). Marine aerosol production: a review of the current knowledge. *Philosophical Transactions of the Royal Society A: Mathematical, Physical and Engineering Sciences*, 365(1856):1753–1774.

Pappalardo, G., Amodeo, A., Mona, L., Pandolfi, M., Pergola, N., and Cuomo, V. (2004). Raman lidar observations of aerosol emitted during the 2002 Etna eruption. *Geophys. Res. Lett.*, 31.

Pappalardo, G., Mona, L., D'Amico, G., Wandinger, U., Adam, M., Amodeo, A., Ansmann, A., Apituley, A., Alados Arboledas, L., Balis, D., Boselli, A., Bravo-Aranda, J. A., Chaikovsky, A., Comeron, A., Cuesta, J., De Tomasi, F., Freudenthaler, V., Gausa, M., Giannakaki, E., Giehl, H., Giunta, A., Grigorov, I., Groß, S., Haeffelin, M., Hiebsch, A., Iarlori, M., Lange, D., Linné, H., Madonna, F., Mattis, I., Mamouri, R.-E., McAuliffe, M. A. P., Mitev, V., Molero, F., Navas-Guzman, F., Nicolae, D., Papayannis, A., Perrone, M. R., Pietras, C., Pietruczuk, A., Pisani, G., Preißler, J., Pujadas, M., Rizi, V., Ruth, A. A., Schmidt, J., Schnell, F., Seifert, P., Serikov, I., Sicard, M., Simeonov, V., Spinelli, N., Stebel, K., Tesche, M., Trickl, T., Wang, X., Wagner, F., Wiegner, M., and Wilson, K. M. (2013). Four-dimensional distribution of the 2010 Eyjafjallajökull volcanic cloud over Europe observed by EARLINET. *Atmospheric Chemistry and Physics*, 13(8):4429–4450.

Pappalardo, G., Wandinger, U., Mona, L., Hiebsch, A., Mattis, I., Amodeo, A., Ansmann, A., Seifert, P., Linne, H., Apituley, A., et al. (2010). EARLINET correlative measurements for CALIPSO: First intercomparison results. *Journal of Geophysical Research: Atmospheres (1984–2012)*, 115(D4).

Platt, C. (1973). Lidar and radioinetric observations of cirrus clouds. *Journal of the atmospheric sciences*, 30(6):1191–1204.

Pöschl, U. (2005). Atmospheric Aerosols: Composition, Transformation, Climate and Health Effects. *Angewandte Chemie International Edition*, 44(46):7520–7540.

Prospero, J. (1999). Long-term measurements of the transport of african mineral dust to the southeastern United States: Implications for regional air quality. *Geophysical Research*, 104(D13):917–927.

Prospero, J., Ginoux, P., Torres, O., Nicholson, S., and Gill, T. (2002). Environmental characterization of global sources of atmospheric soil dust identified with the Nimbus 7 Total Ozone Mapping Spectrometer (TOMS) absorbing aerosol product. *Reviews of Geophysics*, 40(1):1002.

Prospero, J. M. (1997). *Saharan dust transport over the north atlantic ocean and mediterranean: An overview*, chapter 133-151. Springer.

Reid, D., Wardhaugh, K., and Roffey, J. (1979). Radar studies of insect flight at Benalla, Victoria, in February 1974. *CSIRO Aust. Div. Entomol. Tech. Pap.*, 16:21.

Reynolds, A., Reynolds, D., and Riley, J. (2009). Does a 'turbophoretic' effect account for layer concentrations of insects migrating in the stable night-time atmosphere? *J. R. Soc. interface*, 6:87–95.

Reynolds, D., Chapman, J., Edwards, A., Smith, A., Wood, C., Barlow, J., and Woiwod, I. (2005). Radar studies of the vertical distribution of insects migrating over southern Britain: the influence of temperature inversions on nocturnal layer concentrations. *Bull. Entomol. Res.*, 95:259–274.

Reynolds, D., Smith, A., and Chapman, J. (2008). A radar study of emigratory flight and layer formation at dawn over southern Britain. *Bull. Entomol. Res.*, 98:35–52.

Roelofs, G.-J. and Jongen, S. (2004). A model study of the influence of aerosol size and chemical properties on precipitation formation in warm clouds. *Journal of Geophysical Research: Atmospheres (1984–2012)*, 109(D22).

Roesli, H., Kerkmann, J., Rosenfeld, D., and König, M. (2004). Introduction to RGB image composites. "http://oiswww.eumetsat.org/WEBOPS/msg_interpretation/msg_channels.php". consulted on 05/03/2015.

Rosenfeld, D. (2014). Climate effects of aerosol-cloud interactions. *Science*, 1247490(379):343.

Saha, S., Moorthi, S., Pan, H.-L., Wu, X., Wang, J., Nadiga, S., Tripp, P., Kistler, R., Woollen, J., Behringer, D., et al. (2010). The NCEP climate forecast system reanalysis. *Bulletin of the American Meteorological Society*, 91(8):1015–1057.

Schütz, L., Jaenicke, R., and Pietrek, H. (1981). Saharan dust transport over the North Atlantic Ocean. *Geological Society of America Special Papers*, 186:87–100.

Seibert, P. and Frank, A. (2004). Source-receptor matrix calculation with a Lagrangian particle dispersion model in backward mode. *Atmospheric Chemistry and Physics*, 4(1):51–63.

Seinfeld, J. and Pandis, S. (2006). *Atmospheric chemistry and physics: from air pollution to climate change*. John Wiley & Sons, Hoboken, N.J.

Stohl, A., Forster, C., Frank, A., Seibert, P., and Wotawa, G. (2005). Technical note: The Lagrangian particle dispersion model FLEXPART version 6.2. *Atmos. Chem. and Phys.*

Thompson, A. (2007). *Simulating the Adiabatic Ascent of Atmospheric Air Parcels using the Cloud Chamber*. PhD thesis, Department of Meteorology, Penn State.

Twomey, S. (1974). Pollution and the planetary albedo. *Atmospheric Environment (1967)*, 8(12):1251–1256.

Van de Hulst, H. (1957). *Light scattering by small particles*. Courier Dover Publications.

Van de Hulst, H. (1981). *Light scattering by small particles*. Dover Publications.

Veselovskii, I., Dubovik, O., Kolgotin, A., Lapyonok, T., Di Girolamo, P., Summa, D., Whiteman, D., Mishchenko, M., and Tanre, M. (2010). Application of randomly oriented spheroids for retrieval of dust particle parameters from multiwavelength lidar measurements. *J. Geophys. Res.*, 115.

Veselovskii, I., Kolgotin, A., Griaznov, V., Müller, D., Franke, K., and Whiteman, D. N. (2004). Inversion of multiwavelength Raman lidar data for retrieval of bimodal aerosol size distribution. *Applied optics*, 43(5):1180–1195.

Vivekanandan, J., Adams, W., and Bringi, V. (1991). Rigorous approach to polarimetric radar modeling of hydrometeor orientation distributions. *Journal of Applied Meteorology*, 30(8):1053–1063.

Wandinger, U. (2005). *Lidar: Range-Resolved Optical Remote Sensing of the Atmosphere*, chapter Introduction to lidar. Springer.

Ware, R. H. and Solheim, F. S. (2000). Microwave profiling of atmospheric temperature, humidity, and cloud liquid water. In *Second International Asia-Pacific Symposium on Remote Sensing of the Atmosphere, Environment, and Space*, pages 292–302. International Society for Optics and Photonics.

Weitkamp, C. (2006). *Lidar: range-resolved optical remote sensing of the atmosphere*, volume 102. Springer.

Wilson, T. M., Stewart, C., Sword-Daniels, V., Leonard, G. S., Johnston, D. M., Cole, J. W., Wardman, J., Wilson, G., and Barnard, S. T. (2012). Volcanic ash impacts on critical infrastructure. *Physics and Chemistry of the Earth, Parts A/B/C*, 45:5–23.

Wood, C., Chapman, J., Reynolds, D., Barlow, J., Smith, A., and Woiwod, I. (2006). The influence of the atmospheric boundary layer on nocturnal layers of moths migrating over southern Britain. *Int. J. Biometeorol.*, 50:193–204.

Wood, C., O'Connor, E., Hurley, R., Reynolds, D., and Illingworth, A. (2009a). Cloud-radar observations of insects in the UK convective boundary layer. *Meteorol. Appl.*, 16:491–500.

Wood, C., Reynolds, D., Wells, P., Barlow, J., Woiwod, I., and J.W., C. (2009b). Flight periodicity and the vertical distribution of high-altitude moth migration over southern Britain. *Bull. Entomol. Res.*, 99:525–535.

List of Acronyms

ABL	Atmospheric Boundary Layer
ACTRIS	Aerosols, Clouds and Trace gases Research InfraStructure network
AERONET	AErosol RObotic NETwork
AOD	Aerosol Optical Depth
BT	Brightness Temperature
CALIOP	Cloud-Aerosol Lidar with Orthogonal Polarization
CALIPSO	Cloud-Aerosol Lidar and Infrared Pathfinder Satellite Observations
CBL	Convective Boundary Layer
CCN	Cloud Condensation Nuclei
CFS	Climate Forecast System
CIAO	CNR-IMAA Atmospheric Observatory
CNR-IMAA	Consiglio Nazionale delle Ricerche - Istituto di Metodologie per l'Analisi Ambientale
COD	Cloud Optical Depth
EARLINET	European Aerosol Research LIdar NETwork
ECMWF	European Center for Medium-range Weather Forecasts
ESA	European Space Agency
EUMETSAT	European Organisation for the Exploitation of Meteorological Satellites

FFT	Fast Fourier Transform
FLEXPART	FLEXible PARTicle dispersion model
FOV	Field Of View
GCCN	Giant Cloud Condensation Nuclei
GDAS	Global Data Assimilation System
HRV	High Resolution Visible
IN	Ice Nuclei
IPWV	Integrated Precipitable Water Vapour
ITARS	Initial Training for atmospheric Remote Sensing
IWC	Ice Water Content
IWV	Integrated Water Vapour
LDR	Linear Depolarization Ratio
LNA	Low Noise Amplifier
LWC	Liquid Water Content
LWP	Liquid Water Path
MBL	Marine Boundary Layer
MIRA36	MIRA36 pulsed Doppler Ka-band cloud radar
MISR	Multi-angle Imaging Spectroradiometer
MODIS	Moderate Resolution Imaging Spectroradiometer
MSG	METEOSAT Second Generation
MUSA	MUltiwavelength System for Aerosol
MWR	MicroWave Radiometer
NASA	National Aeronautics and Space Administration
NCEP	National Center for Environmental Prediction
PBC	Polarizing Beamsplitter Cube
PBL	Planetary Boundary Layer
PEARL	Potenza EArlinet Raman Lidar
PON	Programma Operativo Nazionale
PRF	Pulse Repetition Frequency
PSD	Particle Size Distribution
RCS	Range Corrected Signal
RGB	Red-Green-Blue
RMS	Peak Width
SEVIRI	Spinning Enhanced Visible and Infrared Imager

SNR	Signal-to-Noise Ratio
TRMM	Tropical Rainfall Measuring Mission
UT	Universal Time
VEL	Doppler velocity
Z	Reflectivity

List of Figures

List of Tables